FEDERAL UNIVERSITY OF MINAS GERAIS (UFMG)
SCHOOL OF ENGINEERING
DEPARTMENT OF STRUCTURAL ENGINEERING
GRADUATE PROGRAM IN STRUCTURAL ENGINEERING (PROPEES)

Hugo Mouro Leão

A CRITICAL STUDY ON PHASE-FIELD MODELLING OF FRACTURE

Belo Horizonte, Brazil
19th May, 2021

Hugo Mouro Leão

A CRITICAL STUDY ON PHASE-FIELD MODELLING OF FRACTURE

Final Version

Master's thesis submitted to the Graduate Program in Structural Engineering (PROPEES) of the School of Engineering at the FEDERAL UNIVERSITY OF MINAS GERAIS (UFMG), in partial fulfillment of the requirements for the master degree in Structural Engineering

Supervisor: Prof. Dr. Roque Luiz da Silva Pitangueira

Co-Supervisor: Prof. Dr. Lapo Gori

Belo Horizonte, Brazil
19th May, 2021

Leão, Hugo Mouro.
L437c A critical study on phase-field modelling of fracture [recurso eletrônico] / Hugo Mouro Leão. - 2021.
1 recurso online (113 f. : il., color.) : pdf.

Orientador: Roque Luiz da Silva Pitangueira.
Coorientador: Lapo Gori.

Dissertação (mestrado) - Universidade Federal de Minas Gerais, Escola de Engenharia.

Apêndices: f. 87-113.

Bibliografia: f. 80-86.
Exigências do sistema: Adobe Acrobat Reader.

1. Engenharia de estruturas - Teses. 2. Fratura - Teses. 3. Método dos elementos finitos. I. Pitangueira, Roque Luiz da Silva. II. Gori, Lapo. III. Universidade Federal de Minas Gerais. Escola de Engenharia. IV. Título.

CDU: 624(043)

Ficha catalográfica elaborada pela bibliotecária Roseli Alves de Oliveira CRB/6 2121
Biblioteca Prof. Mário Werneck, Escola de Engenharia da UFMG

UNIVERSIDADE FEDERAL DE MINAS GERAIS

PROGRAMA DE PÓS-GRADUAÇÃO EM ENGENHARIA DE ESTRUTURAS

ATA DA DEFESA DE DISSERTAÇÃO DE MESTRADO EM ENGENHARIA DE ESTRUTURAS Nº: 383 DO ALUNO HUGO MOURO LEÃO

Às **14:00** horas do dia **19** do mês de **maio** de **2021**, reuniu-se, totalmente por videoconferência para atender aos novos protocolos de distanciamento social adotados pelo Governo Federal e pela Prefeitura de Belo Horizonte, que integram medidas para combater o avanço da pandemia de Covid-19, provocada pelo novo coronavírus, a Comissão Examinadora indicada pelo Colegiado do Programa em 22 de abril de 2021, para julgar a defesa da Dissertação de Mestrado intitulada **"A Critical Study on Phase-Field Modelling of Fracture"**, cuja aprovação é um dos requisitos para a obtenção do Grau de MESTRE EM ENGENHARIA DE ESTRUTURAS na área de Estruturas.

Abrindo a sessão, o Presidente da Comissão, **Prof. Dr. Roque Luiz da Silva Pitangueira**, após dar a conhecer aos presentes o teor das Normas Regulamentares passou a palavra ao candidato para apresentação de seu trabalho. Seguiu-se a arguição pelos examinadores, com a respectiva defesa do candidato. Logo após, a Comissão se reuniu, sem a presença do candidato e do público, para julgamento e expedição do resultado final. Foram atribuídas as seguintes indicações:

Prof. Dr. Roque Luiz da Silva Pitangueira - DEES - UFMG (Orientador)
Prof. Dr. Lapo Gori - DEES - UFMG (Coorientador)
Prof. Dr. Samuel Silva Penna - DEES - UFMG
Prof. Dr. Adair Roberto Aguiar - USP

Pelas indicações acima, o candidato foi considerado APROVADO, conforme pareceres em anexo.

O resultado final foi comunicado publicamente ao candidato pelo Presidente da Comissão. Nada mais havendo a tratar, o Presidente encerrou a reunião e lavrou a presente ATA, que será assinada por todos os membros participantes da Comissão Examinadora.

Belo Horizonte, 19 de maio de 2021.

Observações:

1. A aprovação do candidato na defesa da Dissertação de Mestrado não significa que o mesmo tenha cumprido todos os requisitos necessários para obtenção do Grau de Mestre em Engenharia de Estruturas;
2. Este documento não terá validade sem a assinatura do Coordenador do Programa de Pós-Graduação.

Documento assinado eletronicamente por **Roque Luiz da Silva Pitangueira**, **Professor do Magistério Superior**, em 19/05/2021, às 17:20, conforme horário oficial de Brasília, com fundamento no art. 5º do Decreto nº 10.543, de 13 de novembro de 2020.

Documento assinado eletronicamente por **Lapo Gori**, **Professor do Magistério Superior**, em 19/05/2021, às 17:21, conforme horário oficial de Brasília, com fundamento no art. 5º do Decreto nº 10.543, de 13 de novembro de 2020.

Documento assinado eletronicamente por **Adair Roberto Aguiar**, **Usuário Externo**, em 19/05/2021, às 17:21, conforme horário oficial de Brasília, com fundamento no art. 5º do Decreto nº 10.543, de 13 de novembro de 2020.

Documento assinado eletronicamente por **Samuel Silva Penna**, **Professor do Magistério Superior**, em 19/05/2021, às 17:22, conforme horário oficial de Brasília, com fundamento no art. 5º do Decreto nº 10.543, de 13 de novembro de 2020.

A autenticidade deste documento pode ser conferida no site https://sei.ufmg.br/sei/controlador_externo.php?acao=documento_conferir&id_orgao_acesso_externo=0, informando o código verificador **0703107** e o código CRC **24951D49**.

Referência: Processo nº 23072.222374/2021-79 SEI nº 0703107

Agradecimentos

Agradeço primeiramente à Deus, pela saúde durante o período deste mestrado, e por ter iluminado a minha inteligência para a conclusão deste trabalho.

Ao meu pai, Jésus à minha mãe, Eliane, pelo apoio.

À minha namorada, Tainara Viana, pela companhia.

Ao professor orientador Roque Pitangueira, pelo convite para participar do grupo de pesquisa.

Ao co-orientador Lapo Gori, que prontamente aceitou a nos ajudar neste trabalho.

À CAPES, pelo auxílio financeiro.

Resumo

Nos modelos de degradação elástica, a trinca é considerada de maneira distribuída, e a energia liberada devido ao seu crescimento é controlada pela energia de fratura e outros parâmetros do material, como os limites de resistência. Tal abordagem não é capaz de representar a geometria da região onde ocorre a trinca. Além disso, apresenta algumas limitações bem conhecidas, como forte dependência da malha, início prematuro da fratura e fratura perfeitamente frágil instantânea. O grupo de pesquisa onde surgiu esse trabalho possui uma vasta e diversificada experiência na formulação e implementação de modelos de representação de fissuras. Vários estudos deste grupo de pesquisa referem-se a tentativas de mitigar as limitações mencionadas. Atualmente, modelos de campo de fase têm sido usados como uma abordagem alternativa para lidar com fraturas. Esses modelos consideram uma trinca difusiva e suave pertencente a uma determinada região de volume no qual uma função que descreve a densidade de trincas é prescrita. Esses modelos podem detectar a nucleação de trincas e, como sua principal vantagem, conseguem descrever uma trinca discreta sem se preocupar com a geometria da trinca em si. Desta forma, o modelo de campo de fase consiste em incorporar uma equação adicional no modelo para controlar uma variável de campo contínuo que representa uma transição suave entre o material intacto e o completamente danificado. Este trabalho é uma consequência natural dos estudos anteriores do grupo de pesquisa sendo, neste grupo, um estudo pioneiro sobre modelos de campo de fase visando compreender as principais características, vantagens e desvantagens destes modelos. Todas as implementações computacionais foram feitas no programa *INSANE* (INteractive Structural ANalysis Environment), um programa gratuito desenvolvido pelo próprio grupo de pesquisa.

Palavras-chave: Modelos de fratura baseado em campo de fase; Modelo de degradação elástica; Método dos Elementos Finitos baseado em modelos de campo de fase.

Abstract

While the Griffith approach is based on a discrete description of a crack, in the so-called elastic degrading models, cracks are considered in a continuous way, and the energy released due to crack growth is controlled by the fracture energy and other material parameters, like the strength limits. Such an approach is not capable to represent the geometry of the region where the crack takes place. Also, it presents some well known limitations such as strong mesh-dependency, premature fracture initiation and instantaneous perfectly-brittle fracture. The research group where the present work takes place has a large and diverse experience concerning the formulation and implementation of models for cracking representation. A number of studies of the research group focused on the mitigation of the aforementioned limitations. Nowadays, Phase-field models have been used as an alternative approach to deal with fracture. These models consider a diffusive and smooth crack that belongs to a certain volume region where a function that describes the crack density is prescribed. Such models can detect cracks nucleation and, as their main advantage, can describe a sharp crack without worrying about the sharp crack itself. In this way, the phase-field model consists in incorporating an additional equation in the model to controls a continuous field variable that represents a smooth transition between the completely broken and unbroken material. This work is a natural consequence of the previous studies of the research group. It is a pioneer study of the group concerning phase-field models that aims to understand the main characteristics, advantages and drawbacks of phase-field models. All the computational implementations were done in the software *INSANE* (INteractive Structural ANalysis Environment), an open source software developed by the own research group.

Key-words: Phase field models of Fracture; Elastic degrading models; Finite Element Method based Phase-field models.

Table of contents

Resumo vii

Abstract viii

Table of contents xii

List of tables xiii

List of figures xviii

List of symbols xix

List of abbreviations and acronyms xxii

1 Introduction 1

1.1 Major Objective . . . 2
1.2 Specific Objectives . . . 3
1.3 Outline . . . 3

2 Theoretical foundation 4

2.1 The variational approach to Griffith's theory . . . 4
2.2 Introduction of a diffuse crack . . . 7
2.2.1 A brief introduction to phase-field modelling . . . 7
2.2.2 Strong form of PFM . . . 8
2.2.3 Energetic Degradation Function . . . 11
2.2.4 Generic crack surface density function . . . 12
2.2.5 The strain energy density . . . 13
2.3 Equations of PFM in weak form . . . 14
2.4 FEM Discretization . . . 15
2.5 Phase-field constitutive models . . . 16
2.5.1 Isotropic constitutive model . . . 17
2.5.2 Lancioni and Royer-Carfagni (2009) constitutive model . . . 18
2.5.3 Amor et al. (2009) constitutive model . . . 18

2.5.4 Miehe et al. (2010b) constitutive model . . . 19
2.5.5 Plane case . . . 20
2.6 Solvers . . . 20

3 Implementation **22**
3.1 A brief introduction to *INSANE* . . . 22
3.2 Modifications in *INSANE* structure . . . 23
3.2.1 Phase-field functions . . . 24
3.2.2 Material . . . 25
3.2.3 Constitutive model . . . 25
3.2.4 Analysis model . . . 27
3.2.5 Degeneration . . . 29
3.2.6 Problem driver . . . 29
3.2.7 Assembler . . . 29
3.2.8 Step . . . 31

4 Implementation validation **34**
4.1 Monolithic versus staggered solver . . . 34
4.2 Comparisson between numerical and analytical solution . . . 35
4.2.1 Homogeneous solution . . . 35
4.2.2 Localized solution . . . 37
4.3 Validation of implemented constitutive models . . . 38
4.3.1 Isotropic constitutive model . . . 38
4.3.2 Lancioni and Royer-Carfagni (2009) constitutive model . . . 39
4.3.3 Amor et al. (2009) constitutive model . . . 40
4.3.4 Miehe et al. (2010b) constitutive model . . . 40

5 Comparison between constitutive models **43**
5.1 Shear test . . . 43
5.2 Traction test . . . 46

6 Material law and structural behaviour **48**
6.1 Material behaviour . . . 48
6.1.1 Carreira and Chu (1985, 1986) material . . . 49
6.2 Structural behaviour . . . 50
6.3 Influence of length scale (l_0) in degraded band . . . 53

7 Size effect **54**
7.1 Brazilian splitting test . . . 54
7.2 Bending Test . . . 58

8 Ability to detect crack nucleation **61**
8.1 3 point bending . . . 61
8.2 4 point bending test . . . 61
8.3 Two failure modes of a beam . . . 64

9 Miscellaneous examples **66**
9.1 Three point bending . . . 66
9.2 Four point bending . . . 68
9.3 Antisymmetric sample with two holes . . . 69
9.4 Asymmetrically notched beam . . . 71
9.5 Mixed model failure test . . . 72
9.6 Semi circular bending test . . . 74

10 Conclusions and future research topics **77**

Appendices **87**

A Demonstration of theoretical foundation equations **88**
A.1 Eq. (2.6) . . . 88
A.2 Eq. (2.7) . . . 89
A.3 Eq. (2.11) . . . 90
A.4 Eq. (2.14) . . . 91
A.5 Eq. (2.21) . . . 92
A.6 Eq. (2.24) . . . 94
A.7 Eq. (2.38) . . . 95

B Numerical solution **97**
B.1 Homogeneous solution . . . 98
B.2 Localised solution . . . 99

C Demonstration of FEM equations **102**

D Constitutive and stress tensors **104**
D.1 Eq. (2.57): Lancioni and Royer-Carfagni (2009) . . . 104
D.2 Eq. (2.58c) and Eq. (2.58d): Amor et al. (2009) . . . 105
D.3 Eq. (2.63): Miehe et al. (2010b) . . . 106
D.3.1 The fourth order $\hat{\mathbf{P}}^{\pm}$ tensor . . . 106
D.3.2 The constitutive and stress tensor . . . 107

E Strain energy density particularized for 2-D case **109**
E.1 Eq. (2.64): Isotropic model . . . 109
E.2 Eq. (2.65): Lancioni and Royer-Carfagni (2009) . . . 109

E.3 Eq. (2.66): Amor et al. (2009) 110
E.4 Eq. (2.67): Miehe et al. (2010b) 111

F Demonstration of implementation equations **112**
F.1 Eq. (3.3): Dual internal variable operator in monolithic solver 112
F.2 Eq. (3.10): Constitutive tensor for plane stress in Voigt notation 113

List of tables

2.1 Energetic degradation functions 12
2.2 Geometric crack functions and its corresponding phase-field distribution (Wu et al., 2020). 13
2.3 Active and inactive strain energy density 20

3.1 Implemented crack geometric functions 24

6.1 Parameters of phase-field materials. 49

8.1 Considered values for each test. 64

List of figures

2.1 A solid body with a crack. 4
2.2 Sharp and diffusive crack modeling (Adapted from Miehe et al. (2010b)). (a) Sharp crack at $x = 0$ and (b) diffusive crack at $x = 0$ modeled with the length scale l_0. 7
2.3 A solid body with a phase-field crack. 9
2.4 (a) Energetic degradation function ($g(\phi)$), and (b) Derivative of energetic degradation function ($g'(\phi)$). 12
2.5 Phase-field distribution in function of α 13
2.6 Iterative procedure for staggered solver (Adapted from Zang et al. (2018)). 21

3.1 *INSANE* core organization (Penna, 2011) 22
3.2 Classes representation in UML diagram. 23
3.3 Package with crack geometric functions and energetic degradation functions. 24
3.4 Package with phase-field material. 25
3.5 Diagram with phase-field constitutive models. 26
3.6 Diagram with phase-field analysis model. 27
3.7 Diagram with `PhaseFieldPrescribedDegeneration` 29
3.8 Diagram with `PhaseFieldPhysicallyNonLinear` 30
3.9 Diagram with `PhaseFieldFemAssembler` 30
3.10 Diagram with `PhaseFieldStandardNewtonRaphsonStaggeredSolver` . . . 31
3.11 Global activity diagram 32
3.12 Iterative procedure activities diagram of the phase-field and displacement convergence. 33

4.1 Shear test. (a) Problem setting, (b) Q4 mesh. 34
4.2 Comparison between monolithic and staggered solver for shear test of Fig. 4.1 35
4.3 Material test setting. Thickness of 1 mm. 36
4.4 Comparison between monolithic and staggered solver for shear test of Fig. 4.1 36
4.5 Shear test. Thickness of 1 mm. (a) Problem setting, (b) Modelling, take advantage of symmetry. 37
4.6 Phase-field value along the axis of the bar, for various displacement values of the bar end. 37

4.7 Phase-field profile for shear test. 38
4.8 French Panthéon Fracture. (a) Problem setting, (b) T3 mesh. 39
4.9 Load-displacement curve for french Panthéon fracture test. 39
4.10 Phase-field evolution in french Panthéon fracture test. (a) $\Delta = 0.070$ mm, (b) $\Delta = 0.085$ mm, (c) $\Delta = 0.090$ mm. 40
4.11 Asymmetric traction test. (a) Problem setting (Wu et al., 2020), (b) T3 mesh. 41
4.12 Results of asymmetric traction test. (a) Phase-field profile for $\Delta = 0.35$ mm, (b) Load-displacement curve of the top edge. 41
4.13 Miehe three bending test. Thickness of 1 mm (a) Problem setting (Miehe et al., 2010b), (b) T3 mesh. 42
4.14 Results of Miehe et al. (2010b) bending test. (a) Phase-field profile in 1000th step, (b) Load-displacement curve of the horizontal displacement of the controlled node; (c) Load-displacement curve of the vertical displacement of the loading application node. 42

5.1 Phase-field profile for shear test. The mesh is depicted in Fig. 4.1.b and the constitutive models used are: (a) Lancioni and Royer-Carfagni (2009), (b) Amor et al. (2009), (c) Miehe et al. (2010b). 43
5.2 Refined mesh used in shear test. $h = 0.1$ mm in the unrefined region and $h = 0.002$ mm in the refined region. 44
5.3 Phase-field profile for shear test. The mesh is depicted in Fig. 5.2 and the constitutive models used are: (a) Lancioni and Royer-Carfagni (2009), (b) Amor et al. (2009), (c) Miehe et al. (2010b). 44
5.4 Phase-field profile for shear test and Lancioni and Royer-Carfagni (2009) constitutive model. (a) T3 mesh ($h = 0.1$ mm in the unrefined region and $h = 0.002$ mm in the refined region), (b) Phase-field evolution 45
5.5 Load-displacement curves for shear test. (a) Q4 mesh, (b) Mesh of Fig. 5.2, (c) Mesh of Fig. 5.4. 45
5.6 Traction test. (a) Problem setting, (b) T3 mesh ($h = 0.05$ mm in the unrefined region and $h = 0.001$ mm in the refined region). 46
5.7 Load-displacement curves of the top edge for tension test. 46
5.8 Phase-field profile for tension test. (a) Isotropic constitutive model, (b) Lancioni and Royer-Carfagni (2009) constitutive model, (c) Amor et al. (2009) constitutive model, (d) Miehe et al. (2010b) constitutive model. . . 47

6.1 Stress-strain curves for materials presented in Table 6.1 49
6.2 L-panel. Thickness of 100 mm. (a) Problem setting (Penna, 2011), (b) Mesh for smeared crack model (c) Mesh for phase-field model. 50

6.3 Load-displacement curve of L-Panel. (a) Vertical displacement of the reentrant corner node; (b) Vertical displacement of the lower node of the load application line. 51
6.4 Normalized load-displacement curve of L-Panel. (a) Vertical displacement of the reentrant corner node; (b) Vertical displacement of the lower node of the load application line. 52
6.5 Phase-field profile in 1000th step. (a) $l_0 = 8$ mm, (b) $l_0 = 10$ mm, (c) $l_0 = 20$ mm, (d) $l_0 = 30$ mm. 53

7.1 Diametrical compression setting. (a) Full setting (Zhou et al., 2018), (b) Triangular (T3) mesh with mean nodal distance of 0.5 mm across the domain. 54
7.2 Phase-field profile for various analysis step. (a) Step 100, (b) Step 400, (c) Step 700, (d) Step 1000. 55
7.3 Diametrical compression setting, taking advantage of symmetry. (a) Problem setting. Parameter c is the initial crack size, (b) T3 mesh ($h = 0.5$ mm). 56
7.4 Load factor-displacement curve of the rightmost node, for various initial crack size. 56
7.5 Relation between the nominal resistance with the effective diameter in diametrical compression. 57
7.6 Descending branches of the normalized load factor-displacement curve of the rightmost node, for various initial crack sizes. 57
7.7 Size effect in 3-point bending. $P = 1$ N, the reference value. (a) Problem setting (Penna, 2011), (b) Modelling, taking advantage of symmetry. 58
7.8 Load-displacement curves for the loading application node. 59
7.9 Relation between the nominal resistance with the effective height in 3 point bending test. 59
7.10 Descending branches of the normalized load-displacement curves for the vertical displacement where the load is applied. 60

8.1 Phase-field evolution for 3 point bending test without initial crack. (a) $\Delta = 0.20$ mm, (b) $\Delta = 0.25$ mm, (c)$\Delta = 0.50$ mm. 62
8.2 Four point bending without initial crack. Thickness of 120 mm. 62
8.3 Phase-field evolution for 4 point bending test without initial crack. (a) $\Delta = 0.15$ mm, (b) $\Delta = 0.20$ mm, (c)$\Delta = 0.50$ mm. 63
8.4 Two failure modes of a beam without initial crack. Thickness of 120 mm. . 64
8.5 Phase-field evolution for Test 1. (a) $\Delta = 0.50$ mm, (b) $\Delta = 0.75$ mm, (c)$\Delta = 1.50$ mm. 65
8.6 Phase-field evolution for Test 2. (a) $\Delta = 0.50$ mm, (b) $\Delta = 0.60$ mm, (c)$\Delta = 1.0$ mm. 65

9.1 Three point bending test. Thickness of 150 mm. (a) Problem setting (Khalilpour et al., 2019), (b) T3 mesh. 67
9.2 Load-displacement curve for three point bending test. (a) Horizontal displacement of the controlled node; (b) Vertical displacement of the load application point. 67
9.3 Phase-field profile for three point bending test. 68
9.4 Four point bending test. Thickness of 120 mm. (a) Problem setting (Khalilpour et al., 2019), (b) T3 mesh. 68
9.5 Load-displacement curve for four point bending test. (a) Horizontal displacement of the controlled node; (b) Vertical displacement of the load application load. 69
9.6 Phase-field profile for four point bending test. 69
9.7 Antisymmetric sample with two holes. (a) Problem setting (Egger et al., 2019), (b) T3 mesh. $h = 0.1$ mm in the refined region and $h = 0.5$ mm in the unrefined. 70
9.8 Load-displacement curve of top edge for antisymmetric sample with two holes. 70
9.9 Phase-field profile for $\Delta = 0.022$ mm. (a) With protection around the hole, (b) Without protection around the hole. 71
9.10 Asymmetric notched beam. The hole has 1 mm of radius and the beam has 0.5 mm of thickness. (a) Problem setting (Miehe et al., 2010b), (b) T3 mesh. 71
9.11 Load-displacement curve for the asymmetrically notched beam. (a) Horizontal displacement of the controlled node; (b) Vertical displacement of the load application node. 72
9.12 Phase-field profile for asymmetrically notched beam in 120th step. 72
9.13 Mixed model failure test. Thickness of 50 mm. (a) Problem setting (Wu et al., 2020), (b) T3 mesh with the red support, (c) T3 mesh without the red support. 73
9.14 Load-displacement curve for mixed model failure test. (a) Displacement of the controlled degree of freedom; (b) Vertical displacement of the load application point. 74
9.15 Phase-field profile for mixed model failure test. (a) Without red support (400th step), (b) With red support(250th step). 74
9.16 Semi circular bending test. The mesh has size of 0.5 mm in the refined region and 10 mm elsewhere. (a) Problem setting for mode I of failure (Aliha et al., 2017), (b) Problem setting for mode II of failure (Aliha et al., 2017), (c) T3 mesh for mode I of failure, (d) T3 mesh for mode II of failure. 75

9.17 Load-displacement curve for the semi circular bending test. (a) Displacement of the controlled degree of freedom; (b) Vertical displacement of the load application point. 76
9.18 Phase-field profile for semi circular bending test in 400th step. (a) Mode I of failure, (b) Mode II of failure. 76

List of symbols

E_0	initial elasticity modulus
ν	Poison coefficient
ϕ	phase-field
ϕ'	derivative of ϕ with respect to x
l_0	length scale parameter
G_c	critical energy release rate
t	time
ϵ	perturbation
∇	nabla operator
$\mathcal{G}$	variation of strain energy functional with respect to the crack surface
γ	crack surface density function
$\dot{\gamma}$	crack surface density rate
λ_0	first Lamé constant
μ_0	second Lamé constant
ψ_0^+	active strain energy density
ψ_0^-	inactive strain energy density
H	Heaviside function
Γ	crack surface
$\dot{\Gamma}$	crack surface rate
Ω	body domain
$\partial\Omega$	body boundary
$\partial\Omega_u$	body boundary with prescribed displacements
$\partial\Omega_t$	body boundary with prescribed forces
$\mathcal{B}$	damage part of the body
$\partial\mathcal{B}$	damaged surface of the body
Y	crack driving force
$\bar{Y}$	effective crack driving force
g	energetic degradation function
α	geometrical crack function
ψ_0	elastic strain energy density

ψ	strain energy
P_{ext}	external load potential
E_t	energy functional
Ψ_c	crack surface energy
Ψ_s	strain energy
δP_{ext}	first variation of external load potential
δE_t	first variation of energy functional
$\delta \Psi_c$	first variation of crack surface energy
$\delta \Psi_s$	first variation of strain energy
$\delta \Gamma$	first variation of crack surface
$\dot{P_{ext}}$	external load potential rate
$\dot{E_t}$	energy rate functional
$\dot{\Psi}_c$	crack surface energy rate
$\dot{\Psi}_s$	strain energy rate
$\dot{\Gamma}$	crack surface rate
$\bar{b}$	body forces vector
$\bar{u}$	displacements vector
$\bar{t}$	surface forces vector
$\bar{n}$	surface normal vector
$\delta \bar{u}$	first variation displacements vector
$\dot{\bar{b}}$	body forces rate vector
$\dot{\bar{u}}$	displacements rate vector
$\dot{\bar{t}}$	surface forces rate vector
$\underline{I}$	second order identity tensor
$\underline{\sigma}$	stress tensor
$\underline{\varepsilon}$	strain tensor
$\underline{\varepsilon}_{ac}^{D}$	deviatoric part of the strain tensor
$\underline{\varepsilon}_D$	deviatoric stress tensor
$\underline{\varepsilon}_V$	volumetric stress tensor
$\underline{\varepsilon}^-$	inactive strain tensor
$\underline{\varepsilon}^+$	active strain tensor
$\dot{\underline{\varepsilon}}$	strain rate tensor
$\hat{\mathbf{E}}_0$	linear elastic isotropic constitutive tensor
$\hat{\mathbf{C}}$	non linear constitutive tensor
$\hat{\mathbf{I}}$	fourth order identity tensor
$\hat{\mathbf{P}}^+$	positive $\hat{\mathbf{P}}$ tensor (used in Miehe et al. (2010b) constitutive model)
$\hat{\mathbf{P}}^-$	negative $\hat{\mathbf{P}}$ tensor (used in Miehe et al. (2010b) constitutive model)
$[\mathbf{C}]_{\text{mon}}$	constitutive tangent stiffness matrix, for monolithic solver
$\bar{\sigma}_{\text{mon}}$	dual internal variable operator, for monolithic solver

$[\mathbf{C}]^{u}_{\text{stg}}$	displacement constitutive tangent stiffness matrix, for staggered solver
$[\mathbf{C}]^{\phi}_{\text{stg}}$	phase-field constitutive tangent stiffness matrix, for staggered solver
$\bar{u}_{\text{mon}}$	displacements and phase fields, for monolithic solver
$[\mathbf{N}]_{\text{mon}}$	state variable operator, for monolithic solver
$\bar{d}_{\text{mon}}$	nodal values, for monolithic solver
$\otimes$	outer product

List of abbreviations and acronyms

PFM	Phase-Field Modelling
FEM	Finite Element Method

Chapter 1

Introduction

Fracture is an important failure mechanism for engineering materials and it has been extensively studied to prevent catastrophic collapse of engineering structures (Wu, 2017).

One of the first approaches to the modelling of fracture is the Griffith criterion, that is based on a pre-existing crack that propagates when the energy release rate matches the fracture toughness (Broek, 1984). This method, however, presents a number of limitations, like the need for a pre-existing crack and the impossibility to describe curvilinear crack paths (Miehe et al., 2010b).

While the Griffith approach is based on a discrete description of a crack, in the so-called elastic degrading models, e.g. classic smeared crack models (Borst and Gutiérrez, 1999, de Borst, 2002) and damage models (Mazars, 1984, Simo and Ju, 1987, Lemaitre and Chaboche, 1990), cracks are considered in a continuous way, and the energy released due to crack growth is controlled by the fracture energy and other material parameters, like the strength limits. Even so extensively used, such an approach is not capable to represent the geometry of the region where the crack takes place. Another well known limitation of elastic degrading models is that numerical analyses where localisation occurs are characterised by a number of pathological behaviours, such as strong mesh-dependency, premature fracture initiation and instantaneous perfectly-brittle fracture. These pathological effects are due to the fact that, when strain-softening material models are adopted, at a certain load level the continuum boundary value problem may become ill-posed (loss of ellipticity of the equilibrium equations, corresponding to a singular strain rate). The ill-posedness of the problem corresponds to an infinite set of solutions (discontinuous bifurcation), from which the numerical method selects the one corresponding to the smallest energy dissipation. This approximated solution strongly depends on the mesh; at mesh refinement it tends to a failure with zero energy dissipation, and then to a non-physical behaviour (Borst, de et al., 1993, Peerlings et al., 2002).

The research group where the present work takes place has a large and diverse experience concerning the formulation and implementation of models for cracking representation, as it can be seen by a number of papers on the topic (da Silva et al., 2017,

Malekan et al., 2018, Wolenski et al., 2020, Campos et al., 2020, Wolff et al., 2020, Fonseca et al., 2020)[1]. A number of studies of the research group focused on the mitigation of the aforementioned mesh dependency issue, by: (1) adopting different formulations for inelastic/damage regions (Monteiro, 2013, Oliveira et al., 2020); (2) changing the numerical method, e.g. Generalized Finite Element Method (Monteiro et al., 2020, Novelli et al., 2020), Boundary Element Method (Peixoto et al., 2018, Mendonça et al., 2020), Meshfree Methods (Gori, 2018, Gori et al., 2019*b*) and Coupling Methods (Saliba et al., 2021); (3) modelling damage variable using a nonlocal approach (Peixoto et al., 2019); (4) representing the continuum medium with higher order theories, e.g. micropolar (Gori et al., 2017, 2019*a*), microstretch (Fuina, 2009) or micromorphic (Silva, 2019, Nogueira, 2021); (5) introducing heterogeneity modelling (Monteiro, 2021), and so on. Therefore, even with a large experience in modeling cracks, there is still room for another study. Thus, this work presents a new approach to deal with the fracture, the phase-field approach.

Nowadays, the so-called phase-field models have been used as an alternative approach to deal with fracture. Phase-field models (PFM) can detect cracks nucleation and, as their main advantage, can describe a sharp crack without worrying about the sharp crack itself. In this way, the phase-field model consists in incorporating an additional equation in the model to control a continuous field variable that represents a smooth transition between the completely broken and unbroken material. This variable is 1 for fully broken state and 0 for unbroken state. Another variable of phase-field models is the length scale parameter that relates the diffusive approximation of the sharp crack. When the length parameter tends to zero, the model tends to the Griffith theory, i.e. to a sharp crack. Insofar as the parameter becomes larger, the broken region also becomes larger. Then, such parameter introduces a smooth transition between the broken and unbroken states. This work is a natural consequence of the previous studies of the research group. It is a pioneer study of the group concerning phase-field models. Such a starting study aims to understand the main characteristics, advantages and drawbacks of phase-field models. All the computational implementations were done in the software INSANE (INteractive Structural ANalysis Environment), an open source software based on the Object-Oriented Programing paradigm and developed by the research group since 2002. To generate the mesh and as post-processor, the Gmsh[2] and Paraview[3] softwares were used.

1.1 Major Objective

Taking into account the above discussion, the major objective of this work is to study the theoretical basis of phase-field models of fracture and implement some finite element

[1]See also the web-page of the group, `http://insane.dees.ufmg.br`.
[2]Gmesh software can be download at `https://gmsh.info/`
[3]Paraview software can be download at `https://www.paraview.org/`

method based models, in order to understand the main characteristics, advantages and drawbacks of such approach.

1.2 Specific Objectives

To reach the major objective it will be done:

- To choose a Finite Element Model for phase-field approach;
- To implement the FEM model chosen at INSANE, by using its OOP project with minor modifications, in such way that introduces new java classes for a phase-field constitutive model and for a new version of Newton-Raphson method;
- To validate the implementation by comparing the obtained results with that one's already existing in literature;
- To compare some phase-field constitutive models;
- To analyse the material and structural behaviour of the model;
- To study the size effect with phase-field approach.

1.3 Outline

This work is organized in 10 chapters and 6 appendices. After this first chapter, Chapter 2 presents the theoretical foundation of PFM. Beginning by the variational approach to Griffith's theory that is adapted to introduce the phase-field diffuse crack, all discussion is made until reach at the FEM discretization and the phase-field tangent constitutive tensors. Chapter 3 presents the *INSANE* code modifications that is validated in Chapter 4. Comparisons among the implemented models are presented in Chapter 5. Chapter 6 presents a comparative study on the behaviour of the phase-field strategy at the material and structural levels. Chapter 7 presents a phase-field modelling of size effect on strength and structural brittleness. The phase-field models ability to detect crack nucleation is illustrated by some examples in Chapter 8. Miscellaneous simulations are presented in Chapter 9 in order to try reproducing some examples available in the literature. Finally, Chapter 10 closes the manuscript, summing up the main contributions of this work and discussing future developments. The Appendices A to F brings the demonstrations of equations used throughout this work.

Chapter 2

Theoretical foundation

In this chapter, the theoretical foundation of PFMs will be discussed, starting from the variational approach to Griffith's theory and then presenting the phase-field itself.

2.1 The variational approach to Griffith's theory

Griffith's problem is depicted in Fig. 2.1, where Ω is the problem domain with external boundary $\partial\Omega$ and a crack surface Γ. The external boundary can be splitted in two disjoint parts: $\partial\Omega_u$, representing the region where the displacement is prescribed, and $\partial\Omega_t$, where the loading is prescribed.

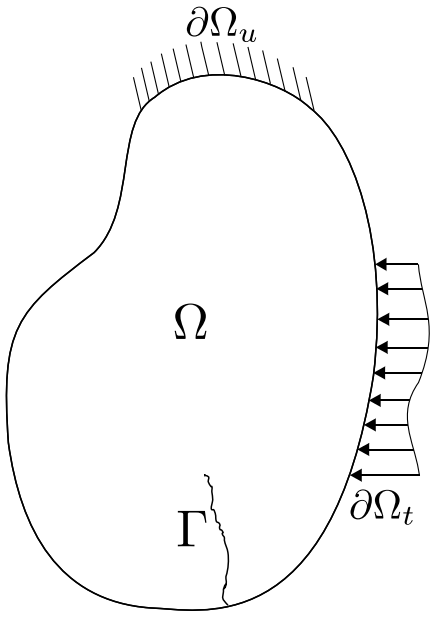

Figure 2.1: A solid body with a crack.

The variational form of the problem consists on the first order optimization of the

total energy functional, that is given by:

$$E_t(\bar{u}, \Gamma) = \Psi_s + \Psi_c - P_{ext} \tag{2.1}$$

with Ψ_s, Ψ_c, and P_{ext} being respectively the strain energy, the surface energy and the external load potential energy functionals, that are defined as:

$$\Psi_s = \int_\Omega \psi_0(\underline{\varepsilon}(\bar{u}))\ \mathrm{d}\mathcal{V} \tag{2.2a}$$

$$\Psi_c = \int_\Gamma G_c\ \mathrm{d}\mathcal{A} \tag{2.2b}$$

$$P_{ext} = \int_\Omega \bar{b} \cdot \bar{u}\ \mathrm{d}\mathcal{V} + \int_{\partial\Omega} \bar{t} \cdot \bar{u}\ \mathrm{d}\mathcal{A} \tag{2.2c}$$

where ψ_0 is the elastic strain energy density, $\underline{\varepsilon}$ is the strain tensor, G_c is the critical energy release rate and $\bar{b}$, $\bar{t}$ and $\bar{u}$ represent, respectively, the body forces, surface forces and displacements. For more details about those functionals see Bourdin et al. (2008).

For a sharp crack, as illustrated in Fig. 2.1, the functions that represent the energy depend on the crack surface and are defined as

$$\Psi_s(\bar{u}) = \int_{\Omega\setminus\Gamma} \psi(\underline{\varepsilon}(\bar{u}), \Gamma)\ \mathrm{d}\mathcal{V} \tag{2.3a}$$

$$\Psi_c(\Gamma) = \int_\Gamma G_c\ \mathrm{d}\mathcal{A} \tag{2.3b}$$

where ψ is the strain energy density.

The variational problem is based on the three following conditions:

1. **Irreversibility condition:** The crack only grows as time goes on, that is, once the crack had opened, it does not heal:

$$\dot{\Gamma}(t) \geq 0 \tag{2.4}$$

2. **Unilateral stationary condition:** It is assumed that the processes always consumes energy, so the pair $(\bar{u}(t), \Gamma(t))$ is a stationary point of the energy functional $(E_t(\bar{u}, \Gamma))$:

$$\delta E_t(\bar{u}, \Gamma) \geq 0 \tag{2.5}$$

3. **Energy conservation condition:** The energy functional E_t has to satisfy the energy balance when the crack grows in time (the proof of Eq. (2.6) can be found in Appendix A.1):

$$\dot{E}_t = \int_{\partial\Omega_u} (\underline{\sigma} \cdot \bar{n}) \cdot \dot{\bar{u}}\ \mathrm{d}\mathcal{A} - \int_\Omega \dot{\bar{b}} \cdot \bar{u}\ \mathrm{d}\mathcal{V} - \int_{\partial\Omega_t} \dot{\bar{t}} \cdot \bar{u}\ \mathrm{d}\mathcal{A} \tag{2.6}$$

Applying the unilateral stationary condition, given by Eq. (2.5), to Eq. (2.1), using

Eq. (2.2), results (as demonstrated on Appendix A.2) in

$$\delta E_t = \int_\Gamma (\underline{\sigma}\cdot\bar{n})\cdot\delta\bar{u}\ \mathrm{d}\mathcal{A} + \int_{\partial\Omega_t} (\underline{\sigma}\cdot\bar{n}-\bar{t})\cdot\delta\bar{u}\ \mathrm{d}\mathcal{A} - \int_{\Omega\backslash\Gamma} (\nabla\underline{\sigma}+\bar{b})\cdot\delta\bar{u}\ \mathrm{d}\mathcal{V} + \left(\frac{\partial\Psi_s}{\partial\Gamma} + G_c\right)\delta\Gamma \geq 0 \tag{2.7}$$

that, due to the arbitrariness of $\delta\bar{u}$, the following expressions must hold:

$$\nabla\underline{\sigma} + \bar{b} = \bar{0} \text{ in } \Omega\backslash\Gamma \tag{2.8a}$$

$$\underline{\sigma}\cdot\bar{n} - \bar{t} = \bar{0} \text{ on } \partial\Omega_t \tag{2.8b}$$

$$\underline{\sigma}\cdot\bar{n} = \bar{0} \text{ on } \Gamma \tag{2.8c}$$

It should be noted that Eq. (2.8a) is the already known pointwise equilibrium equation of a continuum body, Eq. (2.8b) is the natural condition, and Eq. (2.8c) is a stress-free condition for the crack surface. From Eq. (2.8), Eq. (2.7) can be recasted as:

$$\delta E_t = (-\mathcal{G} + G_c)\delta\Gamma \geq 0, \quad \text{where} \quad \mathcal{G} = -\frac{\partial\Psi_s}{\partial\Gamma} \tag{2.9}$$

Since the crack always grows, the therm $\delta\Gamma$ in Eq. (2.9) is positive. Because of that, to maintain the inequality valid, the following must hold:

$$-\mathcal{G} + G_c \geq 0 \Rightarrow \mathcal{G} - G_c \leq 0 \tag{2.10}$$

which corresponds to the Griffith's criterion, which states that the variable $\mathcal{G}$ will always be less then or equal to the fracture energy. In other words, it means that the variation of the strain energy with respect to the crack size will always be less then or equal to the fracture energy, a material parameter.

Finally, from Eq. (2.6), it can be shown that (Appendix A.3):

$$(\mathcal{G} - G_c)\dot{\Gamma} = 0 \tag{2.11}$$

that is, the crack starts growing when $\mathcal{G} = G_c$.

Then, Eqs. (2.4), (2.10) and (2.11) give, in optimization theory, the three conditions of Griffith's criterion, also known as Karush-Kuhn-Tucker conditions:

$$\frac{\partial\Gamma}{\partial t} = \dot{\Gamma} \geq 0 \quad \text{(The crack never heals)} \tag{2.12a}$$

$$\mathcal{G} - G_c \leq 0 \quad (G_c \text{ is a limit}) \tag{2.12b}$$

$$(\mathcal{G} - G_c)\dot{\Gamma} = 0 \quad \text{(The crack starts growing when } \mathcal{G} = G_c) \tag{2.12c}$$

2.2 Introduction of a diffuse crack

In this section, divided in four subsections the phase-field diffuse crack concept will be introduced. In the first subsection the ideas that are behind the phase-field modelling (PFM) will be introduced. In the second subsection, the Griffith theory will be adapted to arrive at the strong form of the phase-field equations. Then, some key functions for PFM, like the energetic degradation function and the generic crack surface density function, will be presented. Finally, the splitting of the strain energy density in active and inactive parts will be introduced, in an attempt to prevent crack propagation under compression.

2.2.1 A brief introduction to phase-field modelling

The general idea of PFM can be illustrated with the model depicted in Fig. 2.2, an infinite bar of cross-section Γ, under axial traction, with a crack at the position x = 0. This figure illustrates the function of the phase-field (ϕ) variable versus the axial position, comparing it with the sharp crack. When the parameter l_0 tends to zero, the model approximates

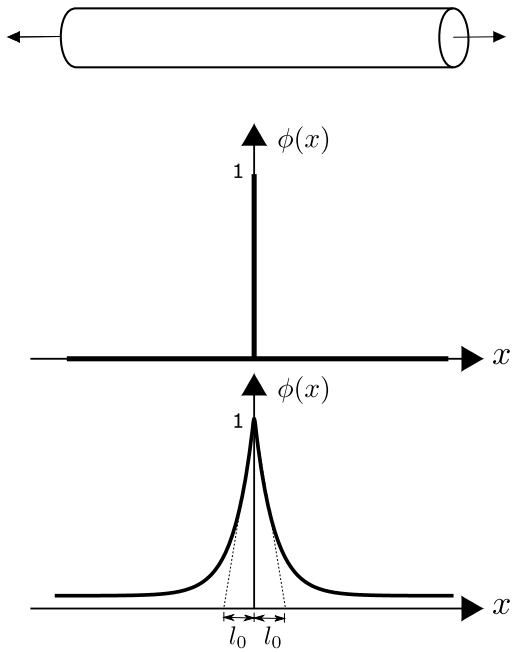

Figure 2.2: Sharp and diffusive crack modeling (Adapted from Miehe et al. (2010b)). (a) Sharp crack at $x = 0$ and (b) diffusive crack at $x = 0$ modeled with the length scale l_0.

to Griffith theory, with a sharp crack. Insofar as the parameter l_0 becomes larger, the broken region of the bar also becomes larger. Then, such parameter introduces a smooth transition between the broken and unbroken state.

From Miehe et al. (2010a), the following equations are given:

$$\phi(x) = e^{-|x|/l_0} \tag{2.13a}$$

$$I(\phi, \phi') = \frac{1}{2}\int_\Omega \phi^2 + l_0^2(\phi')^2 \, \mathrm{d}\mathcal{V} \tag{2.13b}$$

where Eq. (2.13a) gives the phase-field value as a function of the axial position x, in such a way that, in the center of the bar the section is fully broken and at $x \to \infty$ the section is fully unbroken. Eq. (2.13b) gives a functional whose minimization gives a differential equation which solution is given by Eq. (2.13a).

It can also be shown that solving Eq. (2.13b) for Eq. (2.13a), it give us (see Appendix A.4):

$$I(\phi, \phi') = \Gamma l_0 \tag{2.14}$$

So, it can say that, the crack surface area of the corresponding sharp crack can be given by:

$$\Gamma_l = \frac{1}{l_0} I(\phi, \phi') = \int_\Omega \gamma(\phi, \phi') \, \mathrm{d}\mathcal{V} \quad \text{with} \quad \gamma(\phi, \phi') = \frac{1}{2l_0}\phi^2 + \frac{l_0}{2}(\phi')^2 \tag{2.15}$$

where γ is called *crack surface density*.

Without loss of generality, for a 3D case, Eq. (2.15) can be given by:

$$\Gamma_l = \frac{1}{l_0} I(\phi, \nabla\phi) = \int_\Omega \gamma(\phi, \nabla\phi) \, \mathrm{d}\mathcal{V} \tag{2.16}$$

where:

$$\gamma(\phi, \nabla\phi) = \frac{1}{2l_0}\phi^2 + \frac{l_0}{2}|\nabla\phi|^2 \tag{2.17}$$

Within this approach that considers γ as a distribution of crack surfaces in a certain volume, the smeared form of crack surface functional, defined in Eq. (2.2b), becomes

$$\Psi_c = \int_\Omega G_c \gamma(\phi, \nabla\phi) \, \mathrm{d}\mathcal{A} \tag{2.18}$$

2.2.2 Strong form of PFM

The development of the strong form of PFM presented in this subsection is based on Wu et al. (2020) which should be consulted for more details. In that it is considered a domain Ω with a damaged part $\mathcal{B} \subset \Omega$ that corresponds to the crack smoothing region. The boundary of the solid and its damaged surface are, respectively, $\partial\Omega$ and $\partial\mathcal{B}$ (Fig. 2.3).

Considering the smooth crack representation, the surface (Eq. (2.2b)) and strain

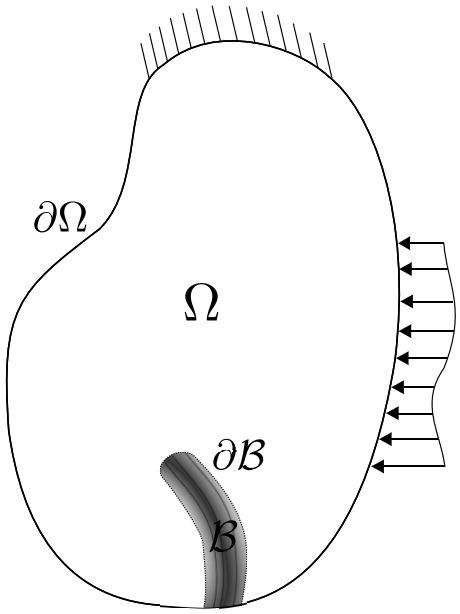

Figure 2.3: A solid body with a phase-field crack.

(Eq. (2.2a)) energies can be recast as

$$\Psi_c = \int_\Gamma G_c \, d\Gamma \approx \int_\mathcal{B} G_c \gamma(\phi, \nabla\phi) \, \mathrm{d}\mathcal{V} \tag{2.19a}$$

$$\Psi_s(\bar{u}, \phi) = \int_\Omega \psi(\underline{\varepsilon}(\bar{u}), \phi) \, \mathrm{d}\mathcal{V} \tag{2.19b}$$

and the total energy functional E_t becomes

$$E_t = \int_\Omega \psi(\underline{\varepsilon}(\bar{u}), \phi) \, \mathrm{d}\mathcal{V} + \int_\mathcal{B} G_c \gamma(\phi, \nabla\phi) \, \mathrm{d}\mathcal{V} - \int_\Omega \bar{b} \cdot \bar{u} \, \mathrm{d}\mathcal{V} - \int_{\partial\Omega} \bar{t} \cdot \bar{u} \, \mathrm{d}\mathcal{A} \tag{2.20}$$

According to the unilateral stationary condition (Eq. (2.5)), the displacement and the phase-field $(\bar{u}, \phi)$ are found by minimizing Eq. (2.20), whose first variation is (see Appendix A.5)

$$\begin{aligned} \delta E_t = &- \int_\Omega (\nabla \underline{\sigma} + \bar{b}) \cdot \delta\bar{u} \, \mathrm{d}\mathcal{V} + \int_{\partial\Omega_t} (\underline{\sigma} \cdot \bar{n} - \bar{t}) \cdot \delta\bar{u} \, \mathrm{d}\mathcal{A} + \\ &+ \int_\mathcal{B} \left[\frac{\partial\psi}{\partial\phi} + G_c \delta_\phi \gamma \right] \delta\phi \, \mathrm{d}\mathcal{V} + \int_{\partial\mathcal{B}} G_c \left(\frac{\partial\gamma}{\partial\nabla\phi} \cdot \bar{n} \right) \delta\phi \, \mathrm{d}\mathcal{A} \geq 0 \end{aligned} \tag{2.21}$$

where:

$$\delta_\phi \gamma = \left(\frac{\partial\gamma}{\partial\phi} - \nabla \cdot \frac{\partial\gamma}{\partial\nabla\phi} \right) \tag{2.22}$$

In analogy to what was discussed on Eq. (2.8), from Eq. (2.21) the following conditions

can be obtained:

$$\nabla \underline{\sigma} + \bar{b} = \bar{0} \text{ in } \Omega \tag{2.23a}$$

$$\underline{\sigma} \cdot \bar{n} - \bar{t} = \bar{0} \text{ on } \partial\Omega_t \tag{2.23b}$$

and defining $Y = -\dfrac{\partial \psi}{\partial \phi}$ (*crack driving force*), it can be shown that (Appendix A.6):

$$\begin{cases} Y - G_c \delta_\phi \gamma = 0, \text{ for } \dot{\phi} > 0 \\ Y - G_c \delta_\phi \gamma < 0, \text{ for } \dot{\phi} = 0 \end{cases} \tag{2.24}$$

$$\frac{\partial \gamma}{\partial \nabla \phi} \cdot \bar{n} = 0 \text{ in } \partial\mathcal{B} \tag{2.25}$$

Observe that the crack driving force is the energetic conjugate of the phase-field just like the stress is from the strains. It is also worth noticing that, Eq. (2.25) is a boundary condition since the γ doesn't varies on the boundary $\partial\mathcal{B}$.

Assuming that ψ depends on a degradation function[1] $g(\phi)$ as presented in Eq. (2.26b) and, using the chain rule, the *crack driving force* can be rewritten as in Eq. (2.26c). Eq. (2.26d) is obtained from Eq. (2.26c) after introduced the definition of the *effective crack driving force* $\bar{Y}$ (Eq. (2.26a)).

$$\bar{Y} = \frac{\partial \psi}{\partial g} \tag{2.26a}$$

$$\psi(\underline{\varepsilon}, \phi) = \psi(\underline{\varepsilon}, g(\phi)) \tag{2.26b}$$

$$Y = -\frac{\partial \psi}{\partial \phi} = -\frac{\partial \psi}{\partial g}\frac{\partial g}{\partial \phi} \tag{2.26c}$$

$$Y = -g'(\phi)\bar{Y} \tag{2.26d}$$

From all this developed theory it can be observed:

1. **Irreversibility condition**

   As it has already been discussed, the crack opening is irreversible. In terms of the functional Γ_l, discussed on Section 2.2.1, this results in:

   $$\dot{\Gamma}_l = \int_{\mathcal{B}} \dot{\gamma}(\phi, \nabla\phi) \, \mathrm{d}\mathcal{V} \geq 0 \tag{2.27}$$

   with:

   $$\dot{\gamma} = \frac{\partial \gamma}{\partial \phi}\dot{\phi} + \frac{\partial \gamma}{\partial \nabla \phi}\nabla\dot{\phi} \tag{2.28}$$

   After some manipulations, and applying the divergence theorem and the boundary

[1] The *energetic degradation function* $g(\phi)$ and its properties will be discussed in Section 2.2.3.

conditions, Eq. (2.27) becomes:

$$\dot{\Gamma}_l = \int_{\mathcal{B}} \dot{\phi}\delta_\phi\gamma \, \mathrm{d}\mathcal{V} \geq 0 \tag{2.29}$$

with $\delta_\phi\gamma$ defined in Eq. (2.22).

Since $\dot{\phi} \geq 0$, it is necessary that $\delta_\phi\gamma \geq 0$. These are the irreversibility conditions.

2. **Phase-field evolution equation**

Introducing $f(Y, \phi) = Y - G_c\delta_\phi\gamma$, the Karush-Kuhn-Tucker conditions become:

$$\dot{\phi} \geq 0, \quad f(Y, \phi) \leq 0, \quad \dot{\phi} f(Y, \phi) = 0 \tag{2.30}$$

with $G_c\delta_\phi\gamma$ being the limit in which the crack will grow. In analogy to a sharp crack, this therm is the critical energy release rate (G_c). The *crack driving force* (Y) can be compared to $\mathcal{G}$.

Considering $\dot{\phi} > 0$, from Eq. (2.24), and considering $\bar{Y}$ as defined on Eq. (2.26d), the following can be obtained:

$$-g'(\phi)\bar{Y} - G_c\delta_\phi\gamma = 0 \longrightarrow \delta_\phi\gamma = \frac{-g'(\phi)\bar{Y}}{G_c} \tag{2.31}$$

In other words, the density of cracks will be smaller the larger Gc. Then, a high value of G_c can be adopted as a strategy to prevent crack formation in certain regions.

2.2.3 Energetic Degradation Function

The energetic degradation function $g(\phi)$, that appears in Eq. (2.26), represents the degradation of the initially-elastic material and, according to Wu et al. (2020), it has to satisfy the following conditions:

- $g(0) = 1$: there is no degradation in the intact material;
- $g(1) = 0$: the energy is completely degraded in fully broken material;
- $g'(\phi) = \dfrac{dg}{d\phi} \leq 0$: the function $g(\phi)$ has to be monotonically decreasing;
- $g'(1) = 0$: there isn't a sudden variation at the interface where the material is fully broken.

Some of the functions already proposed in the literature are illustrated in Table 2.1 and its graphs are plotted on Fig. 2.4. It can be observed that the cubic and quartic functions have $g'(0) = 0$. These functions represent materials whose initial behaviour is linear elastic. On the other hand the quadratic function have $g'(0) < 0$, meaning that material degradation begins as soon as the loading starts.

Table 2.1: Energetic degradation functions

$g(\phi)$	authors
$(1-\phi)^2$	Bourdin et al. (2000)
$3(1-\phi)^2 - 2(1-\phi)^3$	Karma et al. (2001)
$4(1-\phi)^3 - 3(1-\phi)^4$	Kuhn et al. (2015)

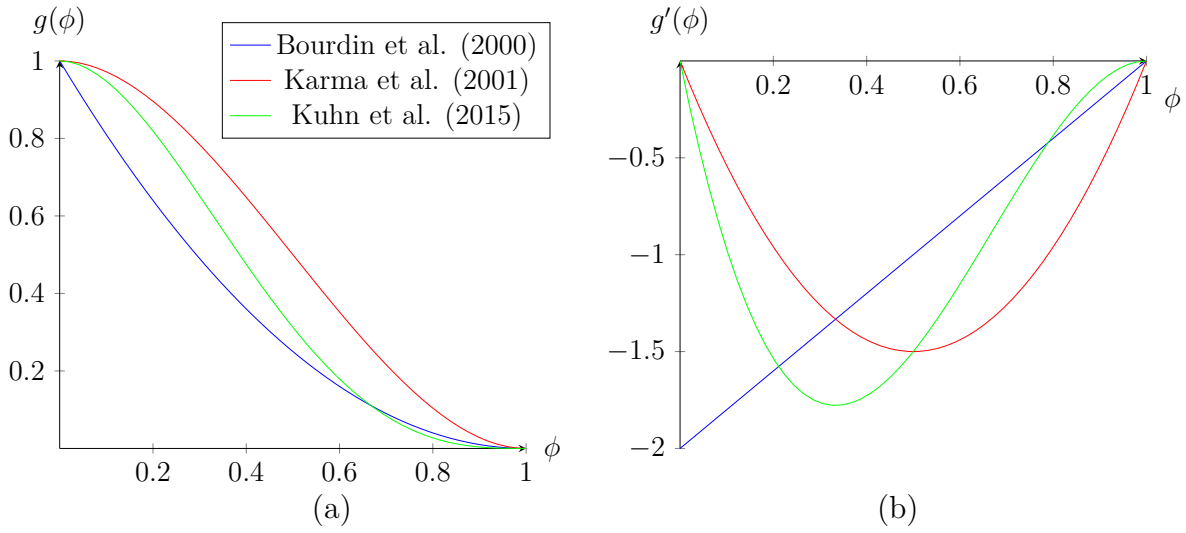

Figure 2.4: (a) Energetic degradation function ($g(\phi)$), and (b) Derivative of energetic degradation function ($g'(\phi)$).

2.2.4 Generic crack surface density function

The *crack surface density function* used by Miehe et al. (2010a) has been presented in Eq. (2.17). This is only one of the several forms to describe the distribution of crack surfaces in a certain volume. Wu (2017) proposed a general equation to describe the crack surface distribution:

$$\gamma(\phi, \nabla\phi) = \frac{1}{C_0}\left[\frac{1}{l_0}\alpha(\phi) + l_0|\nabla\phi|^2\right] \tag{2.32a}$$

$$\delta_\phi\gamma = \frac{1}{C_0}\left[\frac{1}{l_0}\alpha'(\phi) - 2l_0\Delta\phi\right] \tag{2.32b}$$

where $\alpha(\phi)$ is the *geometrical crack function* and the parameter $C_0 = 4\int_0^1 \alpha^{1/2}(\phi)d\phi$.

The function $\alpha(\phi)$ has to satisfy the properties of Eq. (2.33) and it determines how the phase-field will be distributed. Table 2.2 and Fig. 2.5 relates the phase-field distribution in function of the chosen α for a bar under traction with length L. The crack is localized in $x = 0$, where x represents the bar axis.

$$\alpha(0) = 0 \quad \text{and} \quad \alpha(1) = 1 \tag{2.33}$$

Table 2.2: Geometric crack functions and its corresponding phase-field distribution (Wu et al., 2020).

$\alpha(\phi)$	$\phi(x)$
ϕ^2	$e^{-\lvert x\rvert/l_0}$
ϕ	$\left(1-\frac{\lvert x\rvert}{2l_0}\right)^2$
$2\phi-\phi^2$	$1-\sin\left(\frac{\lvert x\rvert}{l_0}\right)$

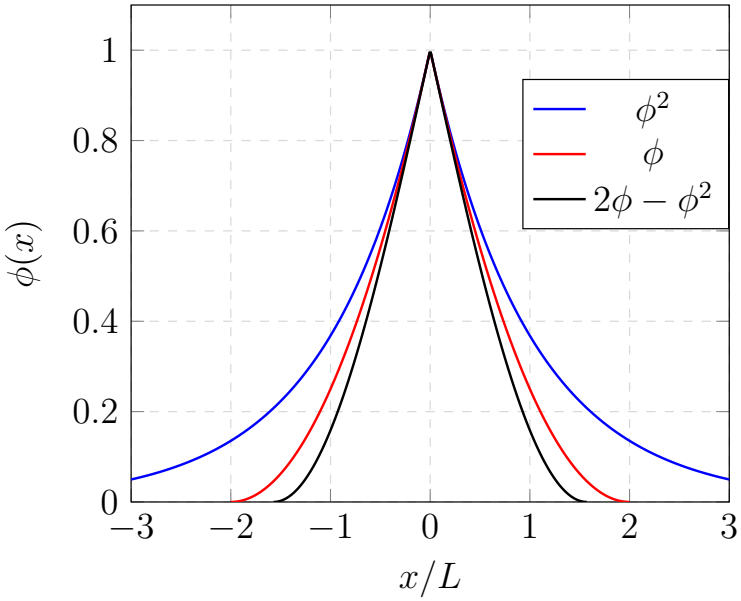

Figure 2.5: Phase-field distribution in function of α

2.2.5 The strain energy density

Whereas in Griffith's approach the strain energy density (ψ) depends on the crack length (Eq. (2.3b)), in phase-field that depends on the energy degradation function ($g(\phi)$). To describe ψ it is used the *initial strain energy density function* $\psi_0(\underline{\varepsilon})$ that, assuming the material to be linear elastic, is given by:

$$\psi_0(\underline{\varepsilon}) = \frac{1}{2}\underline{\sigma} : \underline{\varepsilon} = \frac{1}{2}\underline{\varepsilon} : \hat{\mathbf{E}}_0 : \underline{\varepsilon} = \frac{1}{2}\lambda_0(\mathrm{tr}(\underline{\varepsilon}))^2 + \mu_0\underline{\varepsilon} : \underline{\varepsilon} \tag{2.34}$$

where λ_0 and μ_0 are the Lamé constants.

In order to prevent crack formation in compressed regions, it was proposed an anisotropic formulation based on the following additive decomposition of the elastic strain energy:

$$\psi_0(\underline{\varepsilon}) = \psi_0^+(\underline{\varepsilon}) + \psi_0^-(\underline{\varepsilon}) \tag{2.35}$$

where $\psi_0^+(\underline{\varepsilon})$ is the part that comes from tensile strains (active strain energy density) and $\psi_0^-(\underline{\varepsilon})$ is the part of compression strains (inactive strain energy density). The degradation is then assumed to affect just the tensile part:

$$\psi(\underline{\varepsilon}) = g(\phi)\psi_0^+(\underline{\varepsilon}) + \psi_0^-(\underline{\varepsilon}) \tag{2.36}$$

where the therms ψ_0^+ and ψ_0^- depend on the adopted constitutive model which will be discussed later in Section 2.5.

From Eq. (2.36), the stress field, the constitutive tensor $\hat{\mathbf{C}}$ and the evolution phase-field law becomes:

$$\underline{\sigma} = \frac{\partial \psi}{\partial \underline{\varepsilon}} = g(\phi)\frac{\partial \psi_0^+(\underline{\varepsilon})}{\partial \underline{\varepsilon}} + \frac{\partial \psi_0^-(\underline{\varepsilon})}{\partial \underline{\varepsilon}} \tag{2.37a}$$

$$\hat{\mathbf{C}} = \frac{\partial \underline{\sigma}}{\partial \underline{\varepsilon}} = g(\phi)\frac{\partial^2 \psi_0^+(\underline{\varepsilon})}{\partial \underline{\varepsilon}^2} + \frac{\partial^2 \psi_0^-(\underline{\varepsilon})}{\partial \underline{\varepsilon}^2} \tag{2.37b}$$

$$Y = G_c \delta_\phi \gamma = -g'(\phi)\bar{Y},\ \bar{Y} = \frac{\partial \psi}{\partial g} = \psi_0^+(\underline{\varepsilon}) \tag{2.37c}$$

2.3 Equations of PFM in weak form

From the strong form of PFM presented in Section 2.2.2, the following weak form can be obtained:

$$\begin{cases} \displaystyle\int_\Omega \underline{\sigma} : \delta\underline{\varepsilon}\ \mathrm{d}\mathcal{V} = \delta P_{ext} & (2.38a) \\ \displaystyle\int_\mathcal{B} \left[g'(\phi)\bar{Y}\delta\phi + G_c\delta\gamma \right]\ \mathrm{d}\mathcal{V} \geq 0 & (2.38b) \end{cases}$$

with:

$$\delta\gamma = \frac{1}{C_0}\left[\frac{1}{l_0}\alpha'(\phi)\delta\phi + 2l_0 \nabla\phi \cdot \nabla\delta\phi \right] \tag{2.39}$$

where Eq. (2.38a) is the standard weak form of classical elasticity and the proof of Eqs. (2.38b) and (2.39) can be found in Appendix A.7.

Eq. (2.38) allow to solve a diffuse crack problem in terms of the displacement u and of the phase-field ϕ, under given natural and essential boundary conditions. While essential boundary conditions on the displacement are the same as in a classic elasticity problem, essential boundary conditions on the phase-field can be used to induce a certain cracking behaviour. For example, setting $\phi = 1$ allows to introduce a pre-defined crack in the model, as an alternative to a discrete representation of such crack with the mesh. On the other hand a prescribed zero value of the phase field indicates a region where the formation of a crack is prevented (i.e. where the material remains elastic); to the same purpose, a high value of the fracture energy G_c can be adopted.

While solving Eq. (2.38b), it's important to guarantee the irreversibility condition of the phase-field, $\delta\phi \geq 0$, and the bounds to the phase-field values, $\phi \in [0, 1]$. Among

the possible approaches, Miehe et al. (2010b) introduced a historical variable $\mathcal{H}$ in the formulation, that represents the maximum value of ψ_0^+ attained by the material, i.e. the maximum value of the effective driving force $\bar{Y}$ defined in Eq. (2.37c). With that consideration and using $\alpha(\phi) = \phi^2$, Eq. (2.38b) can be solved as an equality, with the guarantee that the irreversibility and the phase-field bounds are automatically satisfied. The major disadvantage of this approach is that the model is limited to the above geometrical crack function ($\alpha(\phi) = \phi^2$). Another way to deal with that is to use a bounded constrained solver to verify, at each iteration, the problem conditions. This kind of solver is more general and it is able to solve phase-field equations for any functions adopted.

In this work, Miehe et al. (2010b) historical variable method was adopted.

2.4 FEM Discretization

In the Finite Element Method (FEM) formulation, the displacement field and the strain field are written in terms of nodal displacements:

$$\bar{u}(\bar{x}) = [\mathbf{N}]_I^u \, \bar{d}_I \tag{2.40a}$$

$$\bar{\varepsilon}(\bar{x}) = [\mathbf{B}]_I^u \, \bar{d}_I \tag{2.40b}$$

where $\bar{d}_I$ is the nodal displacement vector and, for each node I it has, for 2D case:

$$[\mathbf{N}]_I^u = \begin{bmatrix} N_I^u & 0 \\ 0 & N_I^u \end{bmatrix}, \quad [\mathbf{B}]_I^u = \begin{bmatrix} N_{I,x}^u & 0 \\ 0 & N_{I,y}^u \\ N_{I,y}^u & N_{I,x}^u \end{bmatrix} \tag{2.41}$$

In a similar way, the phase-field is interpolated from its nodal values:

$$\phi(\bar{x}) = [\mathbf{N}]_I^\phi \, \bar{a}_I \tag{2.42a}$$

$$\nabla\phi(\bar{x}) = [\mathbf{B}]_I^\phi \, \bar{a}_I \tag{2.42b}$$

where $\bar{a}_I$ is the nodal phase-field vector and, for each node I:

$$[\mathbf{N}]_I^\phi = \begin{bmatrix} N_I^\phi \end{bmatrix} \tag{2.43}$$

$$[\mathbf{B}]_I^\phi = \begin{bmatrix} N_{I,x}^\phi \\ N_{I,y}^\phi \end{bmatrix} \tag{2.44}$$

From those definitions, it can be shown (Appendix C) that the FEM discretization of

Eq. (2.38) can be written as

$$\begin{cases} \displaystyle\int_{\Omega} [\mathbf{B}]_I^{u,T}\, \bar{\sigma}\ \mathrm{d}\mathcal{V} = \bar{f}_I & \text{(2.45a)} \\ \displaystyle\int_{\mathcal{B}} g'\bar{Y}\, [\mathbf{N}]_I^{\phi,T}\ \mathrm{d}\mathcal{V} + \int_{\mathcal{B}} \frac{G_c}{C_0}\left(\frac{1}{l_0}\alpha'\, [\mathbf{N}]_I^{\phi,T} + 2l_0\, [\mathbf{B}]_I^{\phi,T}\, \nabla\phi\right)\ \mathrm{d}\mathcal{V} \geq \bar{0}_I & \text{(2.45b)} \end{cases}$$

and from that, it can be obtained the residual form

$$\bar{r}_I^u = \int_{\Omega} [\mathbf{B}]_I^{u,T}\, \bar{\sigma}\ \mathrm{d}\mathcal{V} - \bar{f}_I = \bar{0}_I \qquad \text{(2.46a)}$$

$$\bar{r}_I^{\phi} = -\int_{\mathcal{B}} [\mathbf{N}]_I^{\phi,T}\left(g'\bar{Y} + \frac{1}{C_0 l_0}\alpha' G_c\right)\ \mathrm{d}\mathcal{V} - \int_{\mathcal{B}} \frac{2l_0}{C_0} G_c\, [\mathbf{B}]_I^{\phi,T}\, \nabla\phi\ \mathrm{d}\mathcal{V} \leq \bar{0}_I \qquad \text{(2.46b)}$$

that allow to obtain the following tangent stiffness matrix

$$[\mathbf{K}] = \begin{bmatrix} [\mathbf{K}^{\mathbf{uu}}] & [\mathbf{K}^{\mathbf{u}\phi}] \\ [\mathbf{K}^{\phi\mathbf{u}}] & [\mathbf{K}^{\phi\phi}] \end{bmatrix} \qquad \text{(2.47)}$$

where:

$$[\mathbf{K}^{\mathbf{uu}}]_{IJ} = \int_{\Omega} [\mathbf{B}]_I^{u,T}\, \frac{\partial\bar{\sigma}}{\partial\bar{\varepsilon}}\, [\mathbf{B}]_J^{u}\ \mathrm{d}\mathcal{V} \qquad \text{(2.48a)}$$

$$\left[\mathbf{K}^{\mathbf{u}\phi}\right]_{IJ} = \int_{\Omega} [\mathbf{B}]_I^{u,T}\, \frac{\partial\bar{\sigma}}{\partial\phi}\, [\mathbf{N}]_J^{\phi}\ \mathrm{d}\mathcal{V} \qquad \text{(2.48b)}$$

$$\left[\mathbf{K}^{\phi\mathbf{u}}\right]_{IJ} = \int_{\mathcal{B}} [\mathbf{N}]_I^{\phi,T}\, g'\frac{\partial\bar{Y}}{\partial\bar{\varepsilon}}\, [\mathbf{B}]_J^{u}\ \mathrm{d}\mathcal{V} \qquad \text{(2.48c)}$$

$$\left[\mathbf{K}^{\phi\phi}\right]_{IJ} = \int_{\mathcal{B}} [\mathbf{N}]_I^{\phi,T}\left(g''\bar{Y} + \frac{1}{C_0 l_0}\alpha'' G_c\right)[\mathbf{N}]_J^{\phi}\ \mathrm{d}\mathcal{V} + \int_{\mathcal{B}} \frac{2l_0}{C_0} G_c\, [\mathbf{B}]_I^{\phi,T}\, [\mathbf{B}]_J^{\phi}\ \mathrm{d}\mathcal{V} \qquad \text{(2.48d)}$$

As already discussed above in Section 2.3, to ensure the crack irreversibility ($\dot{\phi} \geq 0$) and the boundedness conditions ($\phi \in [0, 1]$) this work has adopted the historical variable of Miehe et al. (2010b), in which $\bar{Y}$ of Eqs. (2.46) and (2.47) assumes the maximum value reached by the active strain energy density (ψ_0^+) along the solver process.

2.5 Phase-field constitutive models

The phase-field models implemented as part of this work will be presented in this section. They are the isotropic constitutive model and the anisotropic constitutive models of Lancioni and Royer-Carfagni (2009), Amor et al. (2009) and Miehe et al. (2010b). It's very important to emphasize that, when dealing with phase-field models, the therms isotropic and anisotropic is not related to material proprieties, but to the separation of regions under tension and compression.

In the implemented constitutive models, the following functions will be used:

- **Ramp function:**

$$\langle x \rangle_+ = \frac{|x| + x}{2}, \quad \langle x \rangle_- = \frac{|x| - x}{2} \tag{2.49}$$

In the first equation, the ramp function returns the value of x, if x is positive, or zero for other values. The second expression in Eq. (2.49) returns the modulus of x, if x is negative, or zero for other values.

- **Sign function:**

$$\text{sgn}(x) = \begin{cases} -1 & \text{, if } x < 0 \\ 0 & \text{, if } x = 0 \\ 1 & \text{, if } x > 0 \end{cases} \tag{2.50}$$

- **Heaviside Function:**

$$\text{H}(x) = \frac{1 + \text{sgn}(x)}{2} \tag{2.51}$$

The Heaviside function returns 0 if $x < 0$, 0.5 if $x = 0$ and 1 if $x > 0$.

- $R_n^{\pm}$ **functions:** Applied to verify the signal of the strain tensor trace and are defined as:

$$R_n^+ = \text{H}(\text{tr}(\underline{\varepsilon})) \tag{2.52a}$$

$$R_n^- = \text{H}(-\text{tr}(\underline{\varepsilon})) \tag{2.52b}$$

From Eq. (2.52) it is observed that:

$$\langle \text{tr}(\underline{\varepsilon}) \rangle_+ = R_n^+ \text{tr}(\underline{\varepsilon}) \tag{2.53a}$$

$$\langle \text{tr}(\underline{\varepsilon}) \rangle_- = R_n^- \text{tr}(\underline{\varepsilon}) \tag{2.53b}$$

Those definitions will help to demonstrate the constitutive and stress tensors of the Amor et al. (2009) and Miehe et al. (2010b) models.

2.5.1 Isotropic constitutive model

In this model, adopted by Bourdin et al. (2000), there is no separation between active and inactive strain energy density. In this way, to become coherent with the theory discussed in Section 2.2.5 it is defined:

$$\psi_0^+(\underline{\varepsilon}) = \psi_0(\underline{\varepsilon}), \ \psi_0^-(\underline{\varepsilon}) = 0 \tag{2.54a}$$

$$\underline{\sigma} = \frac{\partial \psi}{\partial \underline{\varepsilon}} = g(\phi)\bar{\underline{\sigma}}, \ \text{where } \bar{\underline{\sigma}} = \frac{\partial \psi_0}{\partial \underline{\varepsilon}} = \hat{\mathbf{E}}_0 : \underline{\varepsilon} \tag{2.54b}$$

and with these considerations, the energy density function, and the effective crack driving force become:

$$\psi(\underline{\varepsilon}, \phi) = g(\phi)\psi_0(\underline{\varepsilon}) \tag{2.55a}$$

$$\bar{Y} = \psi_0(\underline{\varepsilon}) \tag{2.55b}$$

It is important to point out that the applicability of this constitutive model is limited, since it considers crack propagation in the compressed region.

2.5.2 Lancioni and Royer-Carfagni (2009) constitutive model

This model, used to analyse a structural failure of the Panthéon, considers that the crack occurs because of shear forces, and it takes into account the decomposition of the strain tensor into its spherical ($\underline{\varepsilon}_V$) and deviatoric ($\underline{\varepsilon}_D$) parts:

$$\psi_0^+(\underline{\varepsilon}) = \mu_0 \underline{\varepsilon}_D : \underline{\varepsilon}_D \tag{2.56a}$$

$$\psi_0^-(\underline{\varepsilon}) = \frac{1}{2} K_0 (\mathrm{tr}(\underline{\varepsilon}))^2 \tag{2.56b}$$

$$\underline{\varepsilon} = \underline{\varepsilon}_V + \underline{\varepsilon}_D \tag{2.56c}$$

$$\underline{\varepsilon}_V = \frac{1}{3}\mathrm{tr}(\underline{\varepsilon})\underline{I} \tag{2.56d}$$

$$\underline{\varepsilon}_D = \underline{\varepsilon} - \frac{1}{3}\mathrm{tr}(\underline{\varepsilon})\underline{I} \tag{2.56e}$$

where $\underline{I}$ is the identity matrix and $K_0 = \lambda_0 + \frac{2}{3}\mu_0$. Hence, the constitutive tensor $\hat{\mathbf{C}}$ and the stress field $\underline{\sigma}$ become (Appendix D.1):

$$\sigma = g(\phi)\ 2\mu_0 \underline{\varepsilon}_D + K_0 \mathrm{tr}(\underline{\varepsilon})\underline{I} \tag{2.57a}$$

$$\hat{\mathbf{C}} = 2g(\phi)\mu_0 \underline{\varepsilon}_V + K_0 \underline{I} \otimes \underline{I} \tag{2.57b}$$

2.5.3 Amor et al. (2009) constitutive model

The model of Amor et al. (2009) is an evolution of Lancioni and Royer-Carfagni (2009) and considers the volumetric part as active if the trace of strain tensor is positive:

$$\psi_0^+ = \frac{1}{2} K_0 R_n^+ (\mathrm{tr}(\underline{\varepsilon}))^2 + \mu_0 \underline{\varepsilon}_D : \underline{\varepsilon}_D \tag{2.58a}$$

$$\psi_0^- = \frac{1}{2} K_0 R_n^- (\mathrm{tr}(\underline{\varepsilon}))^2 \tag{2.58b}$$

$$\hat{\mathbf{C}} = g(\phi)\left[K_0 R_n^+ \underline{I} \otimes \underline{I} + 2\mu_0 \left(\hat{\mathbf{I}} - \frac{1}{3}\underline{I} \otimes \underline{I}\right)\right] + K_0 R_n^- \underline{I} \otimes \underline{I} \tag{2.58c}$$

$$\underline{\sigma} = g(\phi)\left[K_0 R_n^+ \underline{\varepsilon} : \underline{I} \otimes \underline{I} + 2\mu_0 \left(\underline{\varepsilon} - \frac{1}{3}\underline{\varepsilon} : \underline{I} \otimes \underline{I}\right)\right] + K_0 R_n^- \underline{\varepsilon} : \underline{I} \otimes \underline{I} \tag{2.58d}$$

where K_0 is defined in Section 2.5.2 and the proof of the expressions of the constitutive and stress tensors can be found in Appendix D.2. According to Wu et al. (2020) this models limit but doesn't prevents crack in compressed regions.

2.5.4 Miehe et al. (2010b) constitutive model

The model proposed by Miehe et al. (2010b) is capable to completely suppress crack growth in compressed regions. This property is obtained by using the following spectral decomposition of the strain tensor:

$$\underline{\varepsilon} = \sum_{n=1}^{3} \varepsilon_n \bar{p}_n \otimes \bar{p}_n = \underline{\varepsilon}^+ + \underline{\varepsilon}^- \tag{2.59}$$

where $\underline{\varepsilon}^+$ and $\underline{\varepsilon}^-$ are, respectively, the active and inactive strain tensors, defined by:

$$\underline{\varepsilon}^+ = \sum_{n=1}^{3} \langle \varepsilon_n \rangle_+ \bar{p}_n \otimes \bar{p}_n \tag{2.60a}$$

$$\underline{\varepsilon}^- = \sum_{n=1}^{3} \langle \varepsilon_n \rangle_- \bar{p}_n \otimes \bar{p}_n \tag{2.60b}$$

where ε_n and $\bar{p}_n$ represent, respectively, the eigenvalues and eigenvectors of the strain tensor. Using this decomposition, the strain energy density can be recasted as

$$\psi_0^+ = \frac{1}{2}\lambda_0 R_n^+ (\mathrm{tr}(\underline{\varepsilon}))^2 + \mu_0 \underline{\varepsilon}^+ : \underline{\varepsilon}^+ \tag{2.61a}$$

$$\psi_0^- = \frac{1}{2}\lambda_0 R_n^- (\mathrm{tr}(\underline{\varepsilon}))^2 + \mu_0 \underline{\varepsilon}^- : \underline{\varepsilon}^- \tag{2.61b}$$

In order to obtain the expressions of the stress and constitutive tensors, it is first necessary to introduce the fourth-order tensors $\hat{\mathbf{P}}^+$ and $\hat{\mathbf{P}}^-$ (see Section D.3.1), that allow to express the active and inactive parts of the strain tensor in terms of the strain tensor itself as

$$\underline{\varepsilon}^+ = \hat{\mathbf{P}}^+ : \underline{\varepsilon}, \quad \underline{\varepsilon}^- = \hat{\mathbf{P}}^- : \underline{\varepsilon} \tag{2.62a}$$

$$\hat{\mathbf{P}}^+ = \sum_{n=1}^{3} \mathrm{H}(\varepsilon_n) \bar{p}_n \otimes \bar{p}_n \otimes \bar{p}_n \otimes \bar{p}_n, \quad \hat{\mathbf{P}}^- = \hat{\mathbf{I}} - \hat{\mathbf{P}}^+ \tag{2.62b}$$

From these definitions it can be shown that (Section D.3.2) the constitutive and stress tensors are given by:

$$\hat{\mathbf{C}} = g(\phi) \left[\lambda_0 R_n^+ \underline{I} \otimes \underline{I} + 2\mu_0 \hat{\mathbf{P}}^+ \right] + \lambda_0 R_n^- \underline{I} \otimes \underline{I} + 2\mu_0 \hat{\mathbf{P}}^- \tag{2.63a}$$

$$\underline{\sigma} = g(\phi) \left[\lambda_0 R_n^+ \mathrm{tr}(\underline{\varepsilon}) \underline{I} + 2\mu_0 \hat{\mathbf{P}}^+ : \underline{\varepsilon} \right] + \lambda_0 R_n^- \mathrm{tr}(\underline{\varepsilon}) \underline{I} + 2\mu_0 \hat{\mathbf{P}}^- : \underline{\varepsilon} \tag{2.63b}$$

2.5.5 Plane case

As it is already known, in plane case, the third component of stress (in case of plane stress) or strain (in case of plane strain) is zero and the strain energy density has to be particularized to those cases. Table 2.3 shows the particularized form of active and inactive strain energy for the presented constitutive models (Demonstrations in Appendix E).

Table 2.3: Active and inactive strain energy density

Const. Model	$\psi_0^{\pm}$	
Isotropic	$\psi_0^+ = \frac{1}{2}\lambda_0 \mathrm{tr}(\varepsilon_{ij})(\varepsilon_{11}+\varepsilon_{22}) + \mu(\varepsilon_{11}^2+\varepsilon_{22}^2+2\varepsilon_{12}^2)$ $\psi_0^- = 0$	(2.64)
Lancioni and Royer-Carfagni (2009)	$\psi_0^+ = \mu_0 \underline{\varepsilon}_{pl}^D : \underline{\varepsilon}_{pl}^D$ $\psi_0^- = \frac{1}{2}\lambda \mathrm{tr}(\underline{\varepsilon})(\varepsilon_{11}+\varepsilon_{22}) +$ $+\mu_0\left(\frac{2}{3}\mathrm{tr}(\underline{\varepsilon})(\varepsilon_{11}+\varepsilon_{22}) - \frac{2}{9}(\mathrm{tr}(\underline{\varepsilon}))^2\right)$	(2.65)
Amor et al. (2009)	$\psi_0^+ = \mu_0 \underline{\varepsilon}_{pl}^D : \underline{\varepsilon}_{pl}^D + \frac{1}{2}\lambda_0 R_n^+ \mathrm{tr}(\varepsilon)(\varepsilon_{11}+\varepsilon_{22}) +$ $+\mu_0 R_n^+\left(\frac{2}{3}\mathrm{tr}(\varepsilon)(\varepsilon_{11}+\varepsilon_{22}) - \frac{2}{9}(\mathrm{tr}(\varepsilon))^2\right)$ $\psi_0^- = \frac{1}{2}\lambda_0 R_n^- \mathrm{tr}(\varepsilon)(\varepsilon_{11}+\varepsilon_{22}) +$ $+\mu_0 R_n^-\left(\frac{2}{3}\mathrm{tr}(\varepsilon)(\varepsilon_{11}+\varepsilon_{22}) - \frac{2}{9}(\mathrm{tr}(\varepsilon))^2\right)$	(2.66)
Miehe et al. (2010b)	$\psi_0^+ = \frac{1}{2}\lambda_0 R_n^+ \mathrm{tr}(\underline{\varepsilon})(\varepsilon_{11}+\varepsilon_{22}) + \mu_0 \underline{\varepsilon}_{pl}^+ : \underline{\varepsilon}_{pl}^+$ $\psi_0^- = \frac{1}{2}\lambda_0 R_n^- \mathrm{tr}(\underline{\varepsilon})(\varepsilon_{11}+\varepsilon_{22}) + \mu_0 \underline{\varepsilon}_{pl}^- : \underline{\varepsilon}_{pl}^-$	(2.67)

where $\underline{\varepsilon}_{pl}^D$, $\underline{\varepsilon}_{pl}^+$ and $\underline{\varepsilon}_{pl}^-$ contain just the plane case components of the respective tensors.

2.6 Solvers

There are two solution strategies that allow to solve the PFM problem illustrated in Section 2.3: *monolitic solvers* and *staggered solvers*. Both of them are implemented in this work.

Monolithic solvers are based on the Newton-Raphson method, and aim to solve each iteration in both the displacement field and phase-field. The solution process relies on the tangent stiffness matrix of Eq. (2.47). As pointed out by Wu et al. (2020), monolithic

solvers present some issues due to the fact that the energy functional of Eq. (2.20) is not convex with respect to both displacement and phase-field variables (Bourdin et al., 2008, Wu et al., 2020). For the models analysed during this work, using monolithic solvers, it was observed that the analysis stop converging when the structure starts to be non linear.

Staggered solvers aim to overcome some of the issues of monolithic solvers, by uncoupling the problem and solving the displacement and the phase-field one at a time resulting in a more robust process. This kind of solver calculates the displacements ($\bar{d}$) for phase-field ($\bar{a}$) given by the last iteration, and then, the updated displacements are used to calculate the phase-field over again. Therefore just the $[\mathbf{K}_\mathbf{I}^{\mathbf{uu}}]$ and $\left[\mathbf{K}_\mathbf{I}^{\phi\phi}\right]$ parts of the tangent stiffness matrix of Eq. (2.47) are used. The process goes on until a convergence criterion is reached. Fig. 2.6 illustrates that process. Starting from point A, and solving Eq. (2.46a) for a fixed phase-field value, it goes to point B. Now, fixing the displacements values and solving Eq. (2.46b), it will reach at point C. The process will be iterated until reaches at the convergent point.

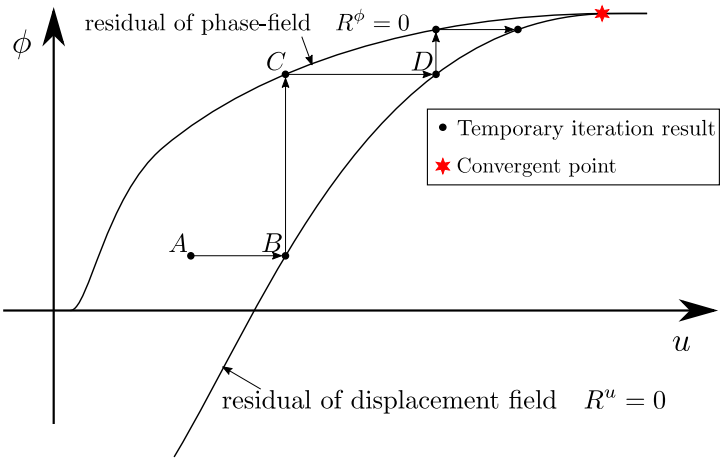

Figure 2.6: Iterative procedure for staggered solver (Adapted from Zang et al. (2018)).

Different solvers have already been proposed in the literature, each one optimized for a specific problem. More informations on the solvers can be found in Chapter 3.

Chapter 3

Implementation

In this chapter the *INSANE* system will be presented together with all the changes that was necessary to implement each kind of solver: monolithic and staggered.

3.1 A brief introduction to *INSANE*

The *INSANE* System (INteractive Structural ANalysis Environment) is an open-source software developed at the Structural Engineering Department of UFMG. Almost all the code is developed in Java and the full potential of object-oriented programming (OOP) is used.

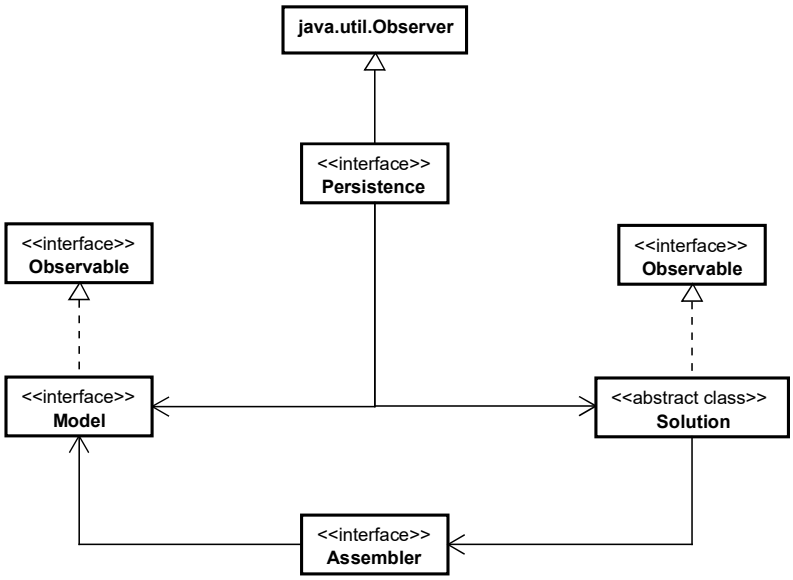

Figure 3.1: *INSANE* core organization (Penna, 2011)

As pointed out in Fig. 3.1, *INSANE* core is composed by the interfaces `Model`, `Solution` and `Assembler` that are responsible to abstract and to solve the model. The `Persistence`

collects and writes the input and output data in files and `Model` stores the lists of nodes, elements, loadings, etc. `Assembler` is responsible to mount the system of equations and `Solution` has the necessary methods to solve the problem.

Some classes and interfaces are of fundamental importance for the development of this work. They are:

- `Material`: Stores the material parameters;
- `ConstitutiveModel`: Responsible to calculate the constitutive material relations and the stress;
- `AnalysisModel`: Has the necessary methods to return all information inherent to the analysis model, for example, the degrees of freedom and the internal variables operator;
- `Degeneration`: Represents the degeneration of the geometry. In 2D case, it represents the degeneration of the thickness, represented by the integration points. It is responsible to ask the constitutive model for the constitutive matrix;
- `ProblemDriver`: Defines the type of problem to be solved (Physically non linear, frame, meshfree, etc) and it is responsible to mount the element incremental stiffness matrix;
- `Assembler`: Mounts all vectors and matrices that are necessary to solve system of equations;
- `Step`: Implements the necessary methods to solve each step of a non linear analysis, for example, the Standard Newton Raphson.

More information of *INSANE* working and its organization is very well described in Penna (2011).

3.2 Modifications in *INSANE* structure

To implement the phase-field models, the entire process was designed in order to reduce the intervention in the code. In the UML diagrams presented throughout this section, the modified classes will be depicted in yellow, the new classes in green and the non modified classes in white (Fig. 3.2).

Figure 3.2: Classes representation in UML diagram.

To implement the monolithic solver, the already implemented Standard Newton Raphson method was sufficient, requiring no changes. For that, the `AnalysisModel` and the `ConstitutiveModel` was thought in order to obtain the tangent stiffness matrix defined

in Eq. (2.47) by

$$[\mathbf{K}] = \int_{\Omega} [\mathbf{B}]^T [\mathbf{C}] [\mathbf{B}] \ \mathrm{d}\mathcal{V} \tag{3.1}$$

where $[\mathbf{B}]$ is the internal variables operator matrix and $[\mathbf{C}]$ is the constitutive matrix.

The implementation of the staggered solver is more complex and needed more intervention in the code, due to the decoupling of the problem. It was necessary to implement different `ConstitutiveModel`, `AnalysisModel`, `ProblemDriver`, `Assembler` and `Step`.

The intervention in the *INSANE* code are described in details along the following items of this section.

3.2.1 Phase-field functions

To bring the phase-field functions together, a package was created to store the energy degradation functions ($g(\phi)$) and the geometric crack functions ($\alpha(\phi)$). Abstract classes

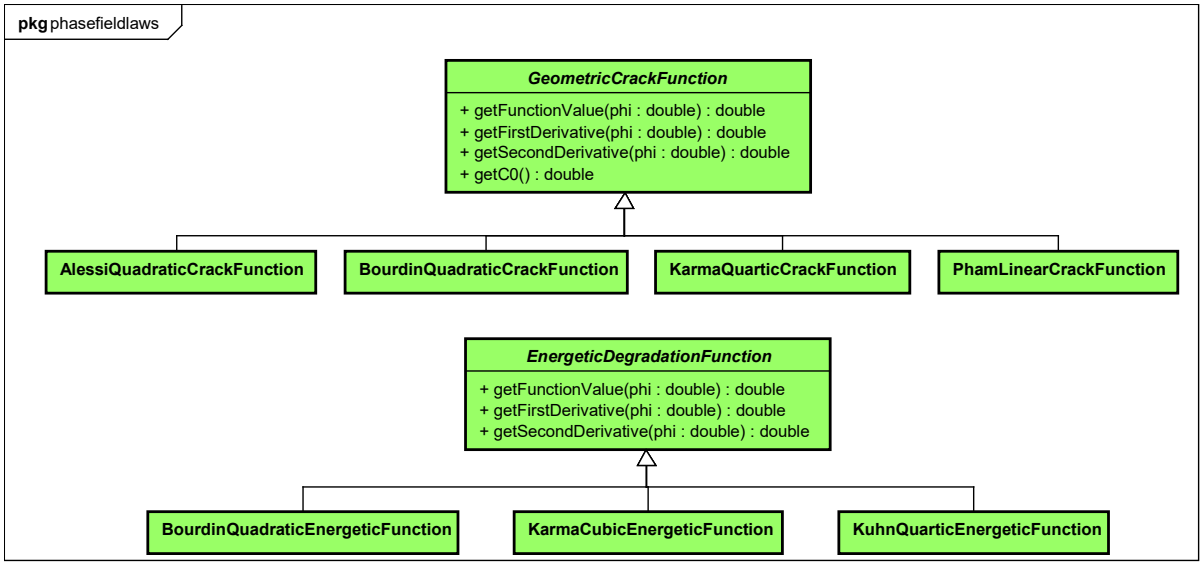

Figure 3.3: Package with crack geometric functions and energetic degradation functions.

were implemented in order to generalize those functions and the inheritance ensures the necessary methods will be implemented for each specific one (See Fig. 3.3). The energetic degradation functions are presented in Table 2.1 and the crack surface functions are in Table 3.1.

Table 3.1: Implemented crack geometric functions

$\alpha(\phi)$	C_0	authors
ϕ^2	2.0	Bourdin et al. (2000)
$16\phi^2(1-\phi^2)$	8/3	Karma et al. (2001)
ϕ	8/3	Pham et al. (2011)
$1-(1-\phi)^2$	π	Alessi et al. (2015)

Although only one function of each has been used in this work, the implementation of some of them has already been done for future use.

3.2.2 Material

Inside of package `phasefieldmaterial`, the class `PhaseFieldMaterial` extends `Material` and is responsible to store the parameters previously defined, including functions $\alpha(\phi)$ and $g(\phi)$ (See Fig. 3.4). Thinking in a future attempt to use the phase-field analysis with exis-

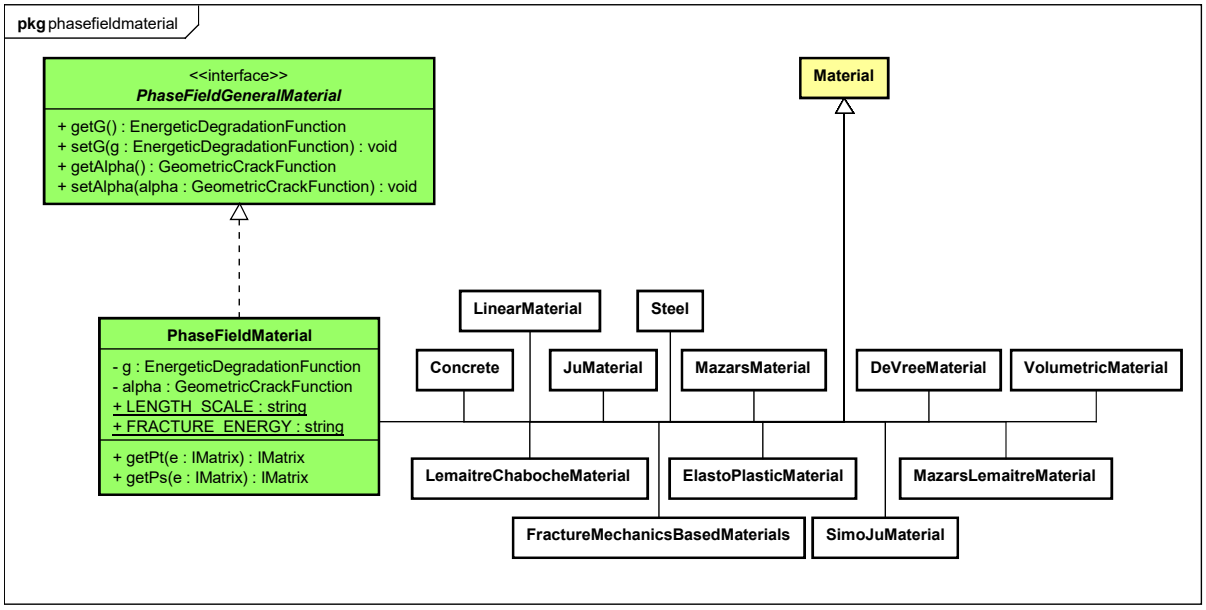

Figure 3.4: Package with phase-field material.

tent materials already implemented in *INSANE*, the interface `PhaseFieldGeneralMaterial` was also created.

3.2.3 Constitutive model

Only the isotropic constitutive model was implemented for the monolithic solver. For the staggered, in addition to the isotropic, it has the anisotropic models of Lancioni and Royer-Carfagni (2009), Amor et al. (2009) and Miehe et al. (2010a). The organization of classes and inheritances is illustrated in Fig. 3.5 and, as it can been seen, the staggered constitutive models count with the interface `PhaseFieldConstitutiveModel` that is responsible to implement the staggered solver additional methods.

To be the superclass of any phase-field staggered constitutive model, the abstract class `PhaseFieldStaggeredConstitutiveModel` counts with the methods that calculates the stress and update all necessary variables in analysis, including the historical variable ($\mathcal{H}$) that ensures the crack irreversibility[1].

[1]This historical variable is presented in Section 2.3

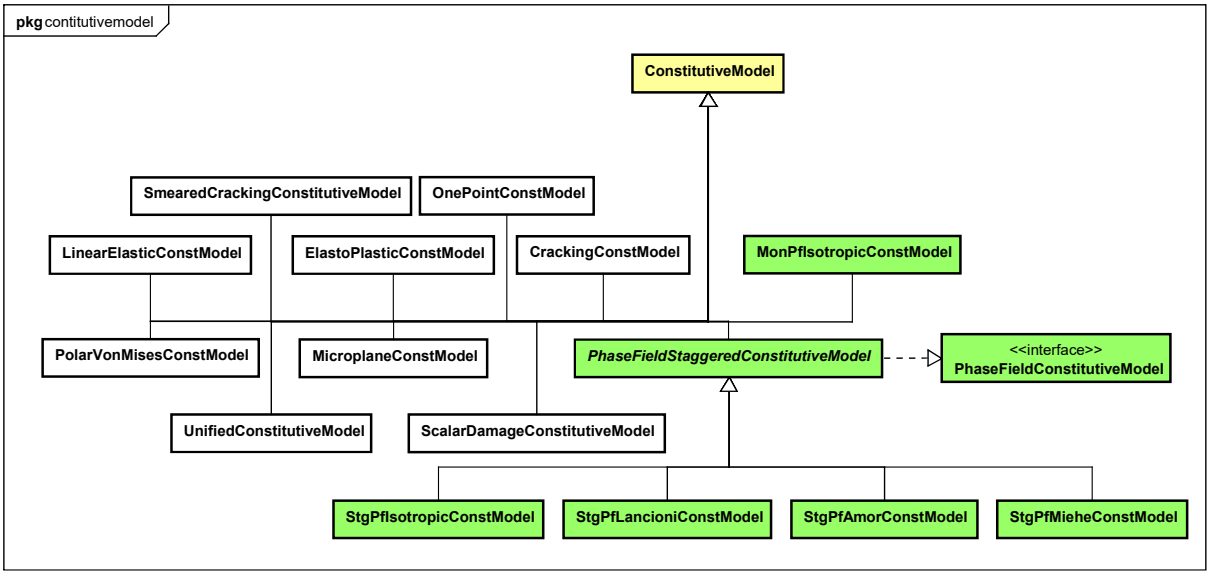

Figure 3.5: Diagram with phase-field constitutive models.

Some particularities of each type of constitutive model are:

- **Phase-field monolithic constitutive model**: As this model doesn't decouple the problem, it has only one constitutive matrix. For the implemented plane case it is given by

$$[\mathbf{C}]_{\text{mon}} = \begin{bmatrix} \left[\dfrac{\partial \bar{\sigma}}{\partial \bar{\varepsilon}}\right]_{3\times 3} & \left[\dfrac{\partial \bar{\sigma}}{\partial \phi}\right]_{3\times 1} & [\mathbf{0}]_{3\times 2} \\ \left[g'\dfrac{\partial \bar{Y}}{\partial \bar{\varepsilon}}\right]_{1\times 3} & \left[g''\bar{Y} + \dfrac{1}{C_0 l_0}\alpha'' G_c\right]_{1\times 1} & [\mathbf{0}]_{1\times 2} \\ [\mathbf{0}]_{2\times 3} & [\mathbf{0}]_{2\times 1} & 2\dfrac{l_0}{C_0} G_c\,[\mathbf{I}]_{2\times 2} \end{bmatrix} \tag{3.2}$$

  and the dual internal variable vector (stress vector) must have the form (Appendix F.1):

$$\bar{\sigma}_{\text{mon}} = \left\{\sigma_x \quad \sigma_y \quad \tau_{xy} \quad g'\bar{Y} + \frac{G_c}{C_0 l_0}\alpha' \quad 2\frac{G_c l_0}{C_0}\phi_{,x} \quad 2\frac{G_c l_0}{C_0}\phi_{,y}\right\}^T \tag{3.3}$$

- **Phase-field staggered constitutive model**: Due to decoupling the problem, it was implemented two different tangent constitutive matrices: one for displacements ($[\mathbf{C}]^u$, given by method `mountCt`) and another one for phase-field ($[\mathbf{C}]^\phi$, given by method `mountPfCt`):

$$[\mathbf{C}]^u_{\text{stg}} = \frac{\partial \bar{\sigma}}{\partial \bar{\varepsilon}}, \quad [\mathbf{C}]^\phi_{\text{stg}} = \begin{bmatrix} g''\bar{Y} + \dfrac{1}{C_0 l_0}\alpha'' G_c & 0 & 0 \\ 0 & 2\dfrac{G_c l_0}{C_0} & 0 \\ 0 & 0 & 2\dfrac{G_c l_0}{C_0} \end{bmatrix} \tag{3.4}$$

Observe that the constitutive matrix of the staggered solver are parts of the monolithic one. Similarly, the dual internal variable operator becomes:

$$\bar{\sigma}^{u}_{\text{stg}} = \begin{Bmatrix} \sigma_x & \sigma_y & \tau_{xy} \end{Bmatrix}^T, \quad \bar{\sigma}^{\phi}_{\text{stg}} = \begin{Bmatrix} g'\bar{Y} + \dfrac{G_c}{C_0 l_0}\alpha' & 2\dfrac{G_c l_0}{C_0}\phi_{,x} & 2\dfrac{G_c l_0}{C_0}\phi_{,y} \end{Bmatrix}^T \tag{3.5}$$

3.2.4 Analysis model

The organization of the analysis model classes is depicted in Fig. 3.6 and the details for them are listed:

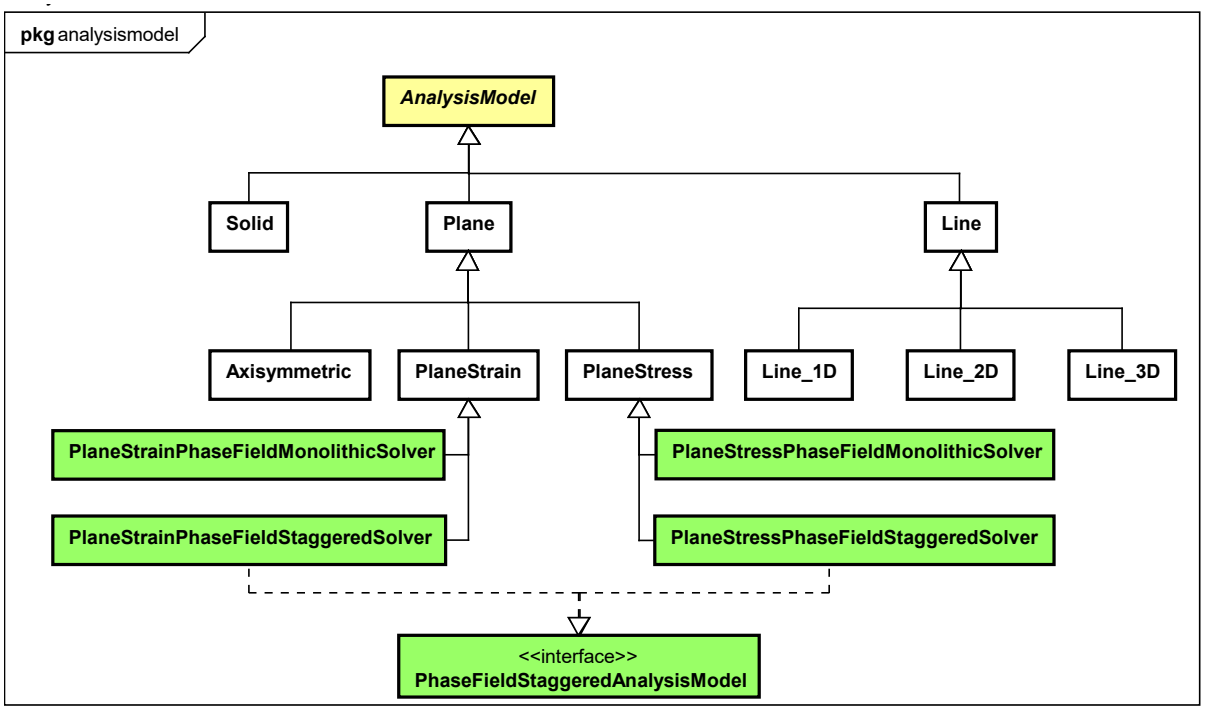

Figure 3.6: Diagram with phase-field analysis model.

- `PlaneStressPhaseFieldMonolithicSolver` and `PlaneStrainPhaseFieldMonolithicSolver`: As the phase-field is a nodal variable, the state variable operator ($[\mathbf{N}]_{\text{mon}}$) was thought in order to get the nodal variables vector by the multiplication:

$$\bar{u}_{\text{mon}} = [\mathbf{N}]_{\text{mon}}\, \bar{d}_{\text{mon}} \tag{3.6}$$

with:

$$\bar{u}_{\text{mon}} = \begin{Bmatrix} u \\ v \\ \phi \end{Bmatrix}, \qquad [\mathbf{N}]_{I_{\text{mon}}} = \begin{bmatrix} N_I & 0 & 0 \\ 0 & N_I & 0 \\ 0 & 0 & N_I \end{bmatrix}, \qquad \bar{d}_{\text{mon}} = \begin{Bmatrix} dx \\ dy \\ a \end{Bmatrix} \tag{3.7}$$

where dx, dy and a are the nodal values of displacement and phase-field, and u, v and ϕ is the interpolated horizontal displacement, vertical displacement and phase-field, respectively.

For the reason already mentioned in Section 3.2, the internal variables operator ($[\mathbf{B}]_{\text{mon}}$) was defined by:

$$[\mathbf{B}]_{I_{\text{mon}}} = \begin{bmatrix} N_{I,x} & 0 & 0 \\ 0 & N_{I,y} & 0 \\ N_{I,x} & N_{I,y} & 0 \\ 0 & 0 & N_I \\ 0 & 0 & N_{I,x} \\ 0 & 0 & N_{I,y} \end{bmatrix} \tag{3.8}$$

- `PhaseFieldStaggeredAnalysisModel`: This interface implements the additional methods for the staggered analysis model as, for example, the responsible to get the internal variables operator:

$$[\mathbf{B}]^u_{I_{\text{stg}}} = \begin{bmatrix} N_{I,x} & 0 \\ 0 & N_{I,y} \\ N_{I,y} & N_{I,x} \end{bmatrix}, \quad [\mathbf{B}]^\phi_{I_{\text{stg}}} = \begin{bmatrix} N_I \\ N_{I,x} \\ N_{I,y} \end{bmatrix} \tag{3.9}$$

  This interface also has a method called `reduceToVoigtMatrix` that transforms the constitutive tensor in the constitutive matrix (in Voigth notation).
- `PlaneStressPhaseFieldStaggeredSolver`: This class implements the interface `PhaseFieldStaggeredAnalysisModel` and its `reduceToVoigtMatrix` method mounts the constitutive displacement matrix according to Eq. (3.10) (Demonstration in Appendix F.2):

$$[\mathbf{C}]^u_{\text{stg}} = \begin{bmatrix} \left(c_{1111} - \dfrac{c_{1133}c_{3311}}{c_{3333}}\right) & \left(c_{1122} - \dfrac{c_{1133}c_{3322}}{c_{3333}}\right) & 0 \\ \left(c_{2211} - \dfrac{c_{2233}c_{3311}}{c_{3333}}\right) & \left(c_{2222} - \dfrac{c_{2233}c_{3322}}{c_{3333}}\right) & 0 \\ 0 & 0 & \dfrac{1}{2}(c_{1212} + c_{1221}) \end{bmatrix} \tag{3.10}$$

  where c_{ijkl} are the components of the constitutive tensor ($\hat{\mathbf{C}}$).
- `PlaneStrainPhaseFieldStaggeredSolver`: As there isn't deformation in the third plane, the `reduceToVoigtMatrix` method of this class returns:

$$[\mathbf{C}]^u_{\text{stg}} = \begin{bmatrix} c_{1111} & c_{1122} & 0 \\ c_{2211} & c_{2222} & 0 \\ 0 & 0 & \dfrac{1}{2}(c_{1212} + c_{1221}) \end{bmatrix} \tag{3.11}$$

3.2.5 Degeneration

The degeneration is responsible to ask the constitutive model for the constitutive matrix. Due to decoupling promoted by the staggered solver, a new class needed to be created (`PhaseFieldPrescribedDegeneration`) to get the matrix regarding to the phase-field calculation process (method `mountPfCt`, in `PhaseFieldConstitutiveModel`). The class diagram is depicted in Fig. 3.7.

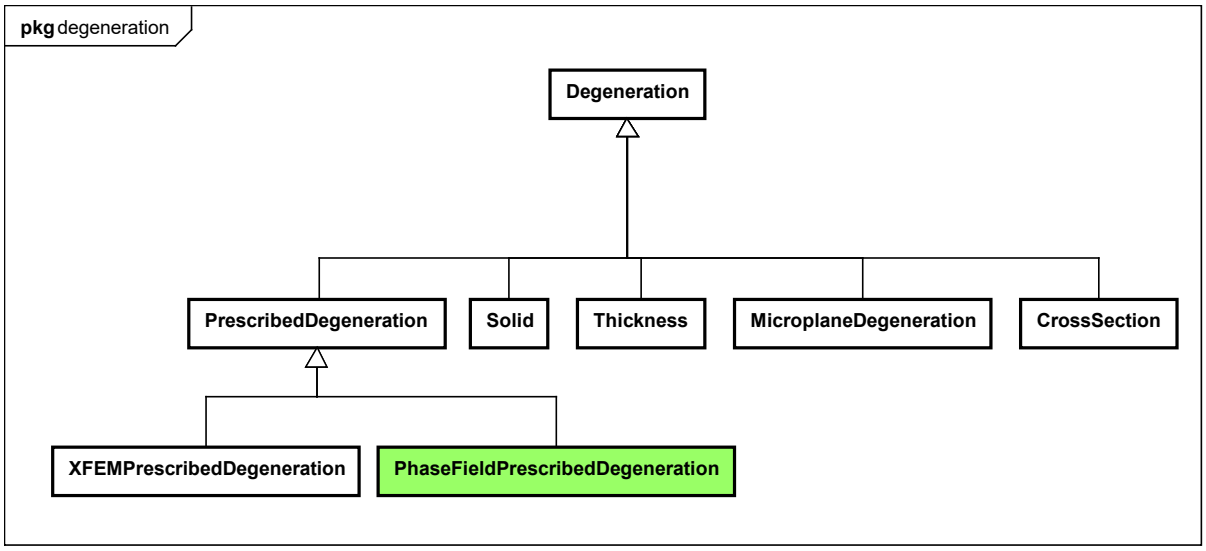

Figure 3.7: Diagram with `PhaseFieldPrescribedDegeneration`

3.2.6 Problem driver

A new problem driver that extends `PhysicallyNonLinear` was created in order to calculate, for each element, the incremental phase-field stiffness matrix (`getPfIncrementalC`) and the vector with the phase-field internal variables (`calculatesPfGradients`). See the implementation diagram in Fig. 3.8.

3.2.7 Assembler

The implemented class `PhaseFieldFemAssembler` extends `FemAssembler` and it has a method called `initAditionalKeys` that is responsible for initializing the additional variables necessary of phase-field. The said assembler has methods to get the reduced phase-field state variable vector (`getXufi`), the reduced residual vector (`getPfFp`) and to number the equations for phase-field and displacements (`numberEquations`). The implemented class among the already existent ones is depicted in Fig. 3.9.

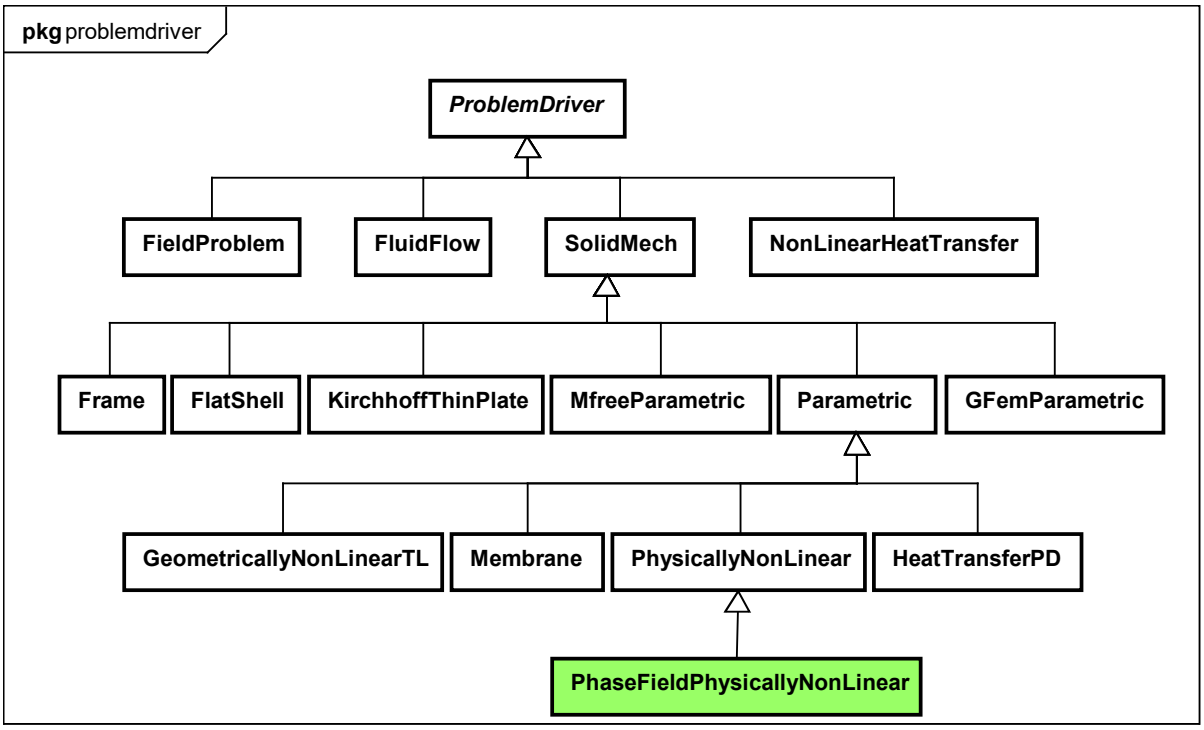

Figure 3.8: Diagram with `PhaseFieldPhysicallyNonLinear`

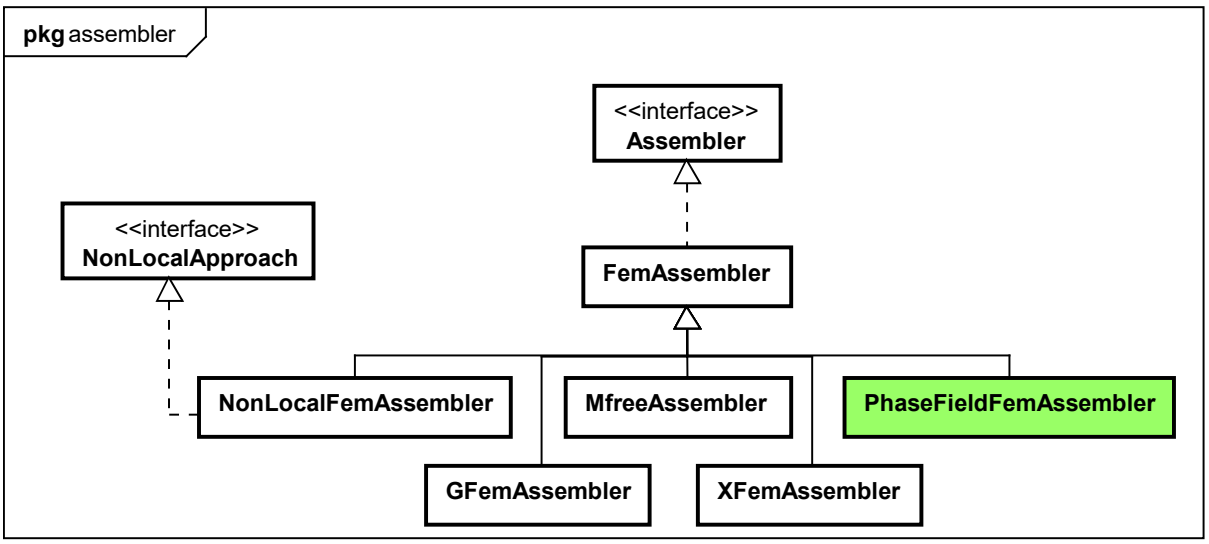

Figure 3.9: Diagram with `PhaseFieldFemAssembler`

3.2.8 Step

The class `PhaseFieldStandardNewtonRaphsonStaggeredSolver` was implemented to be a new Standard Newton Raphson method that solves displacements and phase-field in alternating iterations (See Fig. 3.10). The activities diagrams of the algorithm used is

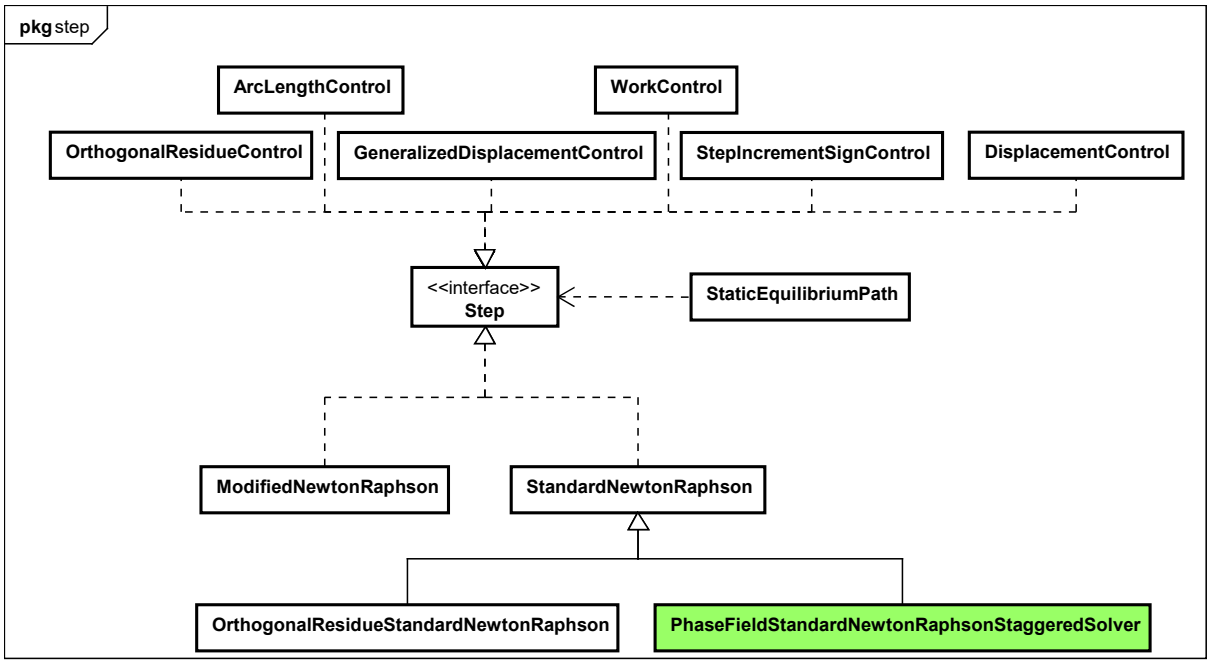

Figure 3.10: Diagram with `PhaseFieldStandardNewtonRaphsonStaggeredSolver`

shown in Fig. 3.11 and Fig. 3.12.

As it can been seen, the predictor is calculated as soon as the step starts (displacements and residual forces vector). This part is calculated only once, at the beginning of the step. After that, the solver enters in an iterative procedure to converge the displacements with the phase-field values of the last iteration and then, another iterative process is triggered to converge the phase-field variables with displacements just obtained.

In the process, the convergence is verified locally, when the displacement or the phase-field is being calculated, and globally, when the step convergence is checked. The local convergence is reached when the error calculated by

$$\text{Error} = \frac{\left\|\delta\bar{X}\right\|}{\left\|\bar{X}\right\|} \tag{3.12}$$

is smaller then a defined tolerance, where $\delta\bar{X}$ and $\bar{X}$ can be the residual load and the forces vector, or the incremental displacements and the displacements vector, depending on the convergence type. After the phase-field is calculated, the residual forces and the incremental displacements vector are updated, and then Eq. (3.12) is used to check the global convergence by testing if the obtained error is less then an specified tolerance.

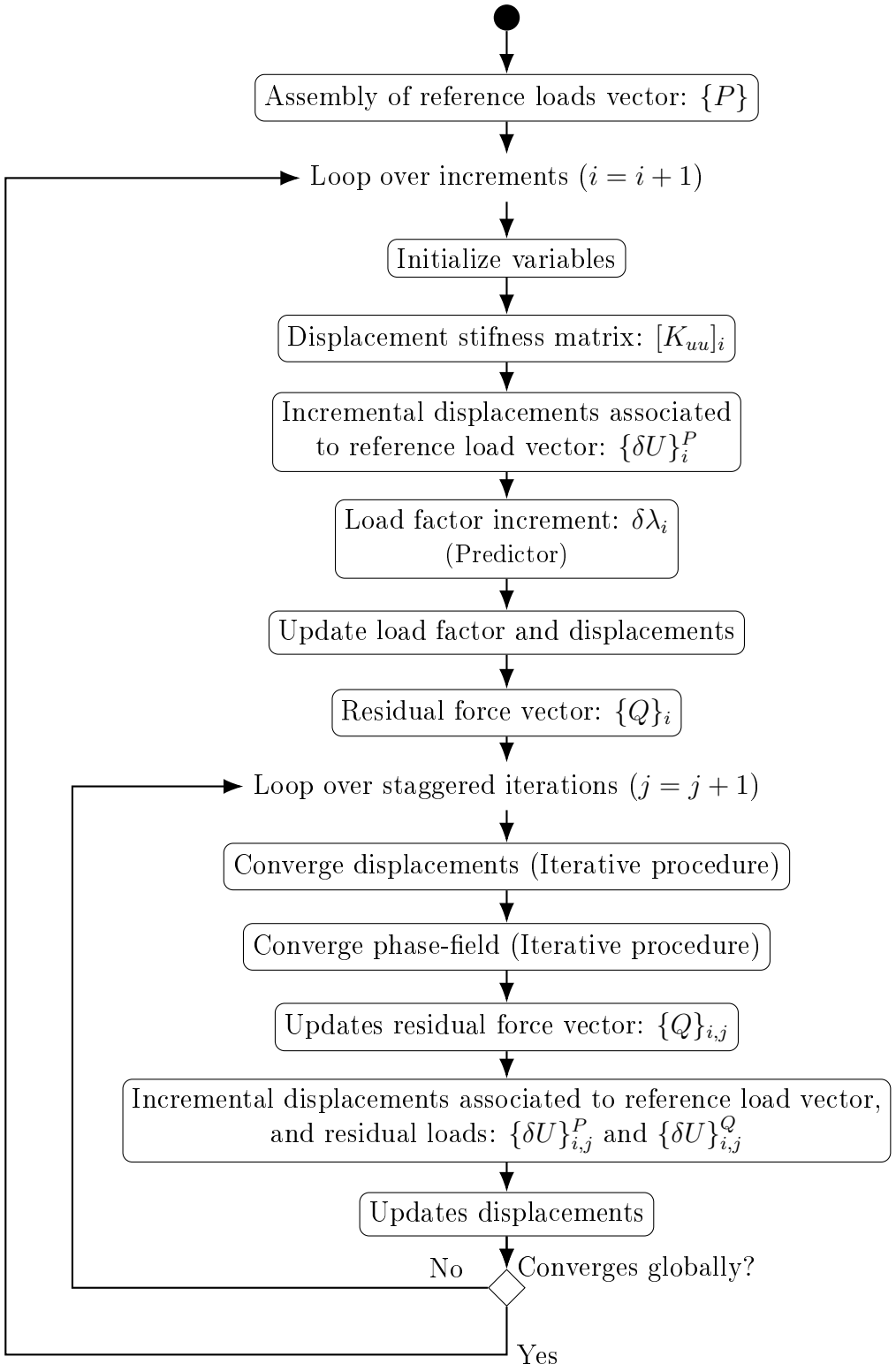

Figure 3.11: Global activity diagram

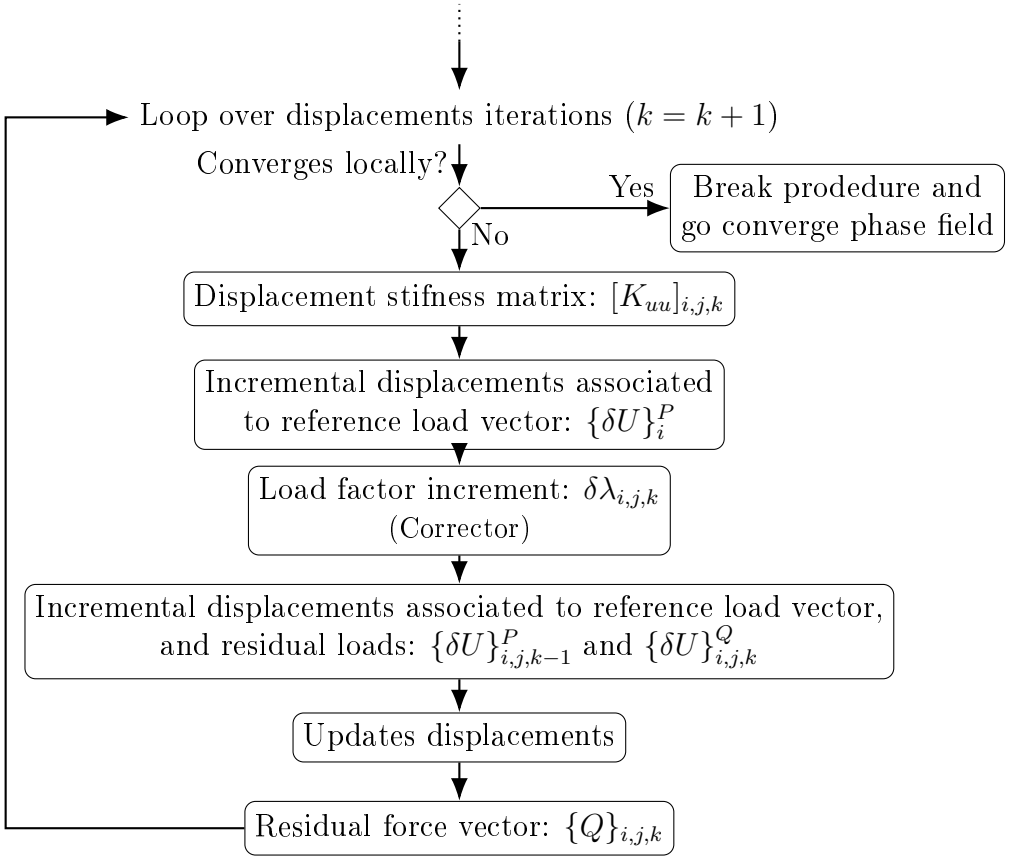

(a) Activity diagram to converge displacements.

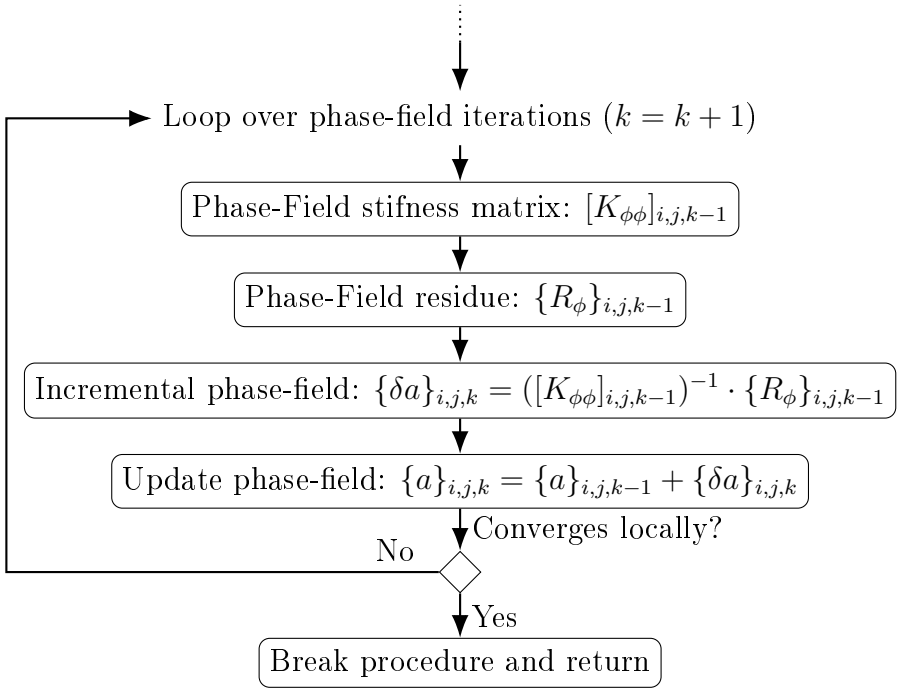

(b) Activity diagram to converge displacements.

Figure 3.12: Iterative procedure activities diagram of the phase-field and displacement convergence.

Chapter 4

Implementation validation

In this chapter, divided in three sections, the implementation in INSANE code will be verified. In the first section, a comparison is made between the monolithic and staggered solver. Then, analytical and numerical solutions will be confronted and, in the last section, tests for each implemented constitutive model are presented. In all examples were used $\alpha(\phi) = \phi^2$ and $g(\phi) = (1-\phi)^2$.

4.1 Monolithic versus staggered solver

The setting depicted in Fig. 4.1 is used to compare the monolithic and staggered solver. The model is subject to a plane strain state with the bottom edge fixed and the other

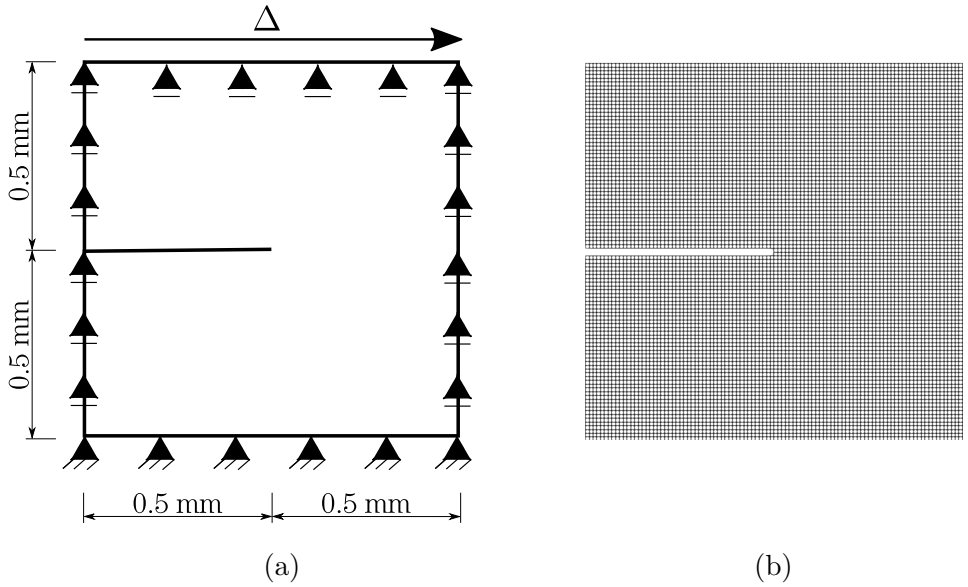

Figure 4.1: Shear test. (a) Problem setting, (b) Q4 mesh.

edges fixed in vertical direction. A constant horizontal displacement is imposed in all

nodes of the top edge. The mesh is composed by quadrilateral elements (Q4) with size of 0.01 mm.

In the analysis the horizontal displacement of the top left node was controlled with increments of 1.0×10^{-4} mm and the convergence was verified in residual force with tolerance of 1.0×10^{-3}. The isotropic constitutive model was considered with the following material proprieties: $E_0 = 210$ kN/mm^2, $\nu = 0.2$, $G_c = 0.0027$ kN/mm and $l_0 = 0.02$ mm.

Fig. 4.2 shows the load versus displacement curve for the controlled node. It can be

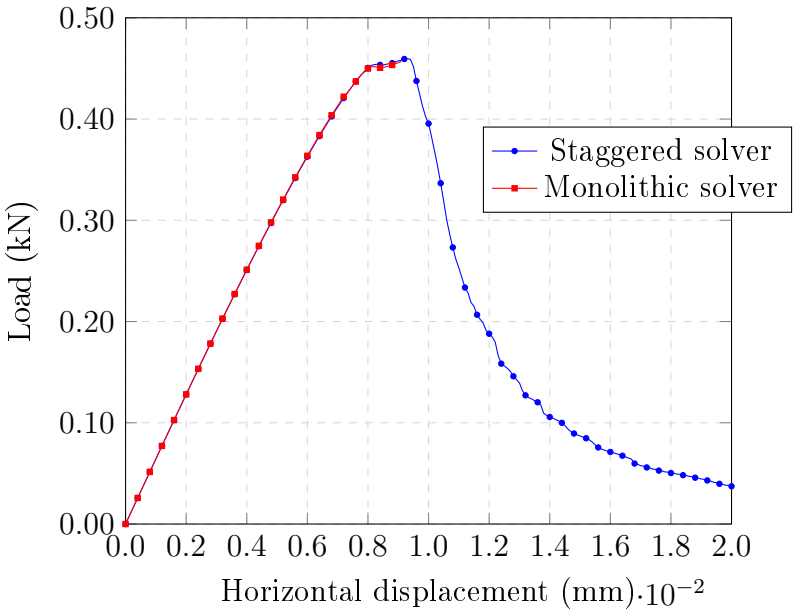

Figure 4.2: Comparison between monolithic and staggered solver for shear test of Fig. 4.1

observed that the monolithic solver stops converging when the crack starts to propagate. On the other hand, the staggered solver is able to continue the analysis until it reaches the defined step limit.

4.2 Comparisson between numerical and analytical solution

In this section the analytical solution presented in Appendix B will be compared with the numerical results obtained from INSANE. The homogeneous and the localized solution will be analysed.

4.2.1 Homogeneous solution

To verify the homogeneous solution the material test depicted in Fig. 4.3 was considered. The model consists in only one Q4 element, subject to plane stress with thickness of 1 mm. The analysis was performed with the isotropic constitutive model, and the

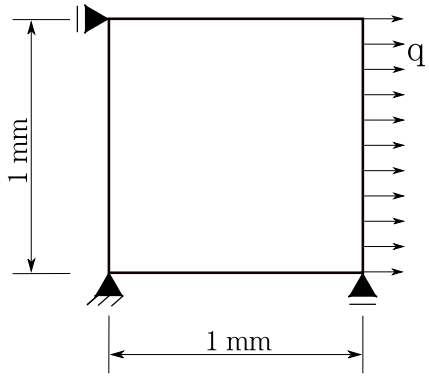

Figure 4.3: Material test setting. Thickness of 1 mm.

following material parameters: $E_0 = 25850$ N/mm^2, $\nu = 0.18$, $G_c = 0.065$ N/mm and $l_0 = 24.31$ mm.

The numerical solution was obtained by controlling the horizontal displacement of the right top node with increments of 1.0×10^{-6}, and the analytical one was obtained using Eq. (4.1) below, whose demonstration is in Appendix B.1. Fig. 4.4 shows the stress-strain plot for each case.

$$\sigma = \sqrt{A_0 \frac{\alpha'(\phi)}{\omega'(\phi)}}, \quad \varepsilon = \frac{1}{\mathbb{E}_0}\sqrt{-A_0 \frac{\alpha'(\phi)}{g'(\phi)}}, \quad u = \varepsilon L = \frac{L}{E_0}\sqrt{-A_0 \frac{\alpha'(\phi)}{g'(\phi)}} \tag{4.1}$$

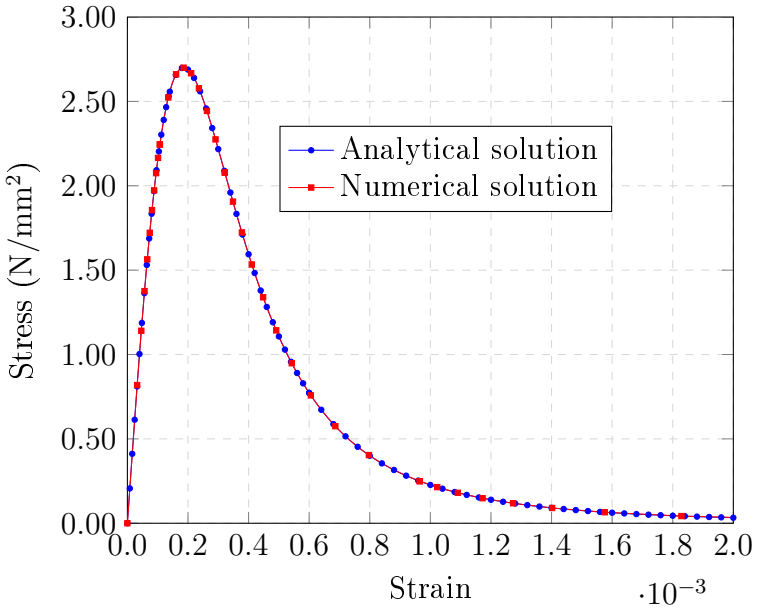

Figure 4.4: Comparison between monolithic and staggered solver for shear test of Fig. 4.1

4.2.2 Localized solution

The setting depicted in Fig. 4.5 is used to simulate the localized solution. The bar has dimensions of $100 \times 1 \times 1$ mm^3 and is subjected to a uniform traction force. Due to the

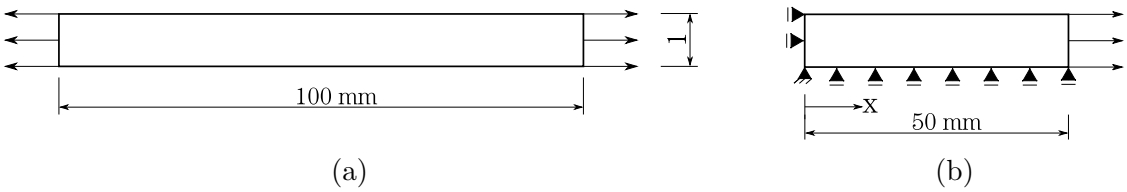

Figure 4.5: Shear test. Thickness of 1 mm. (a) Problem setting, (b) Modelling, take advantage of symmetry.

symmetry, only half of the bar was modelled. The mesh was composed by quadrilateral elements (Q4) with size of 0.5 mm. The specimen was subject to plane stress with $E_0 = 25850$ N/mm^2, $\nu = 0.18$, $G_c = 0.065$ N/mm and $l_0 = 24.31$ mm. In order to ensure that the localization will start in the center of the bar, the first elements on the left in the modelling were defined with $G_c = 0.064$ N/mm.

Fig. 4.6 shows the phase-field evolution along the bar axis and it is noted that the damaged region extends across the entire domain, that is, there isn't a damaged region whose size is much smaller than the bar length as defined in demonstration (See Appendix B.2). In fact, that was already expected since the geometric crack function ($\alpha(\phi) = \phi^2$) used

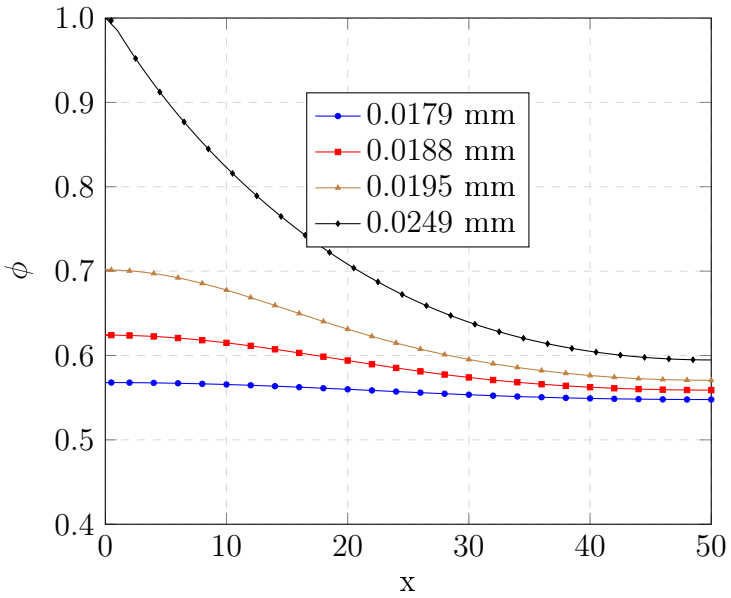

Figure 4.6: Phase-field value along the axis of the bar, for various displacement values of the bar end.

induces the exponential behaviour of ϕ along the axis[1]. Therefore, for the numerical

[1]See Eq. (2.13a)

solution to present results consistent with the analytical solution it is necessary to use α functions that allow a well-defined degraded region. With the historical based solver implemented in this work it is impossible to use them.

4.3 Validation of implemented constitutive models

As previously said, the constitutive models implemented in this work are: the isotropic constitutive model and the anisotropic constitutive models of Lancioni and Royer-Carfagni (2009), Amor et al. (2009) and Miehe et al. (2010b). In this section, the results obtained with INSANE will be compared with the already existent in literature.

It is important to make some observations:

- Phase-field models are very dependent on the mesh size (h). Therefore the finite element mesh requires a minimum element size to be able to solve the model. Miehe et al. (2010a) says that for elements inside the crack band the size $h \leq l_0/2$. For cohesive fracture Wu (2017) suggests $h \leq 5l_0$.
- Due to the hardware limitation, some analysis were made with a less refined mesh than that of the reference articles. In this way, the similarity of the results was verified.

4.3.1 Isotropic constitutive model

To validate the isotropic constitutive model the setting and parameters of Section 4.2.1 were used. Fig. 4.7 shows the phase-field evolution when the horizontal displacement is

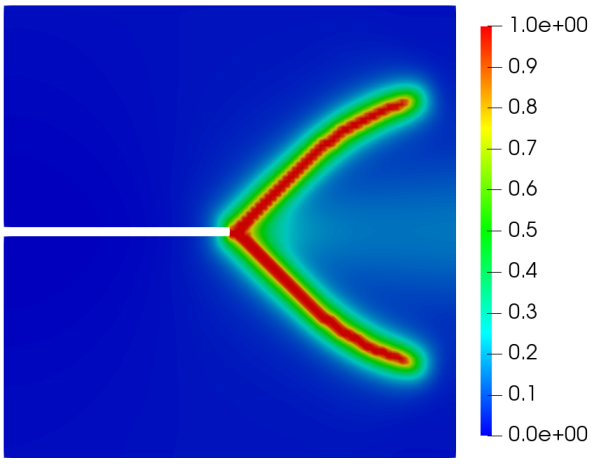

Figure 4.7: Phase-field profile for shear test.

0.02 mm. It can be observed that, the crack path is similar to that obtained by Wu et al. (2020).

4.3.2 Lancioni and Royer-Carfagni (2009) constitutive model

To validate the constitutive model of Lancioni and Royer-Carfagni (2009) the setting depicted in Fig. 4.8 was used.

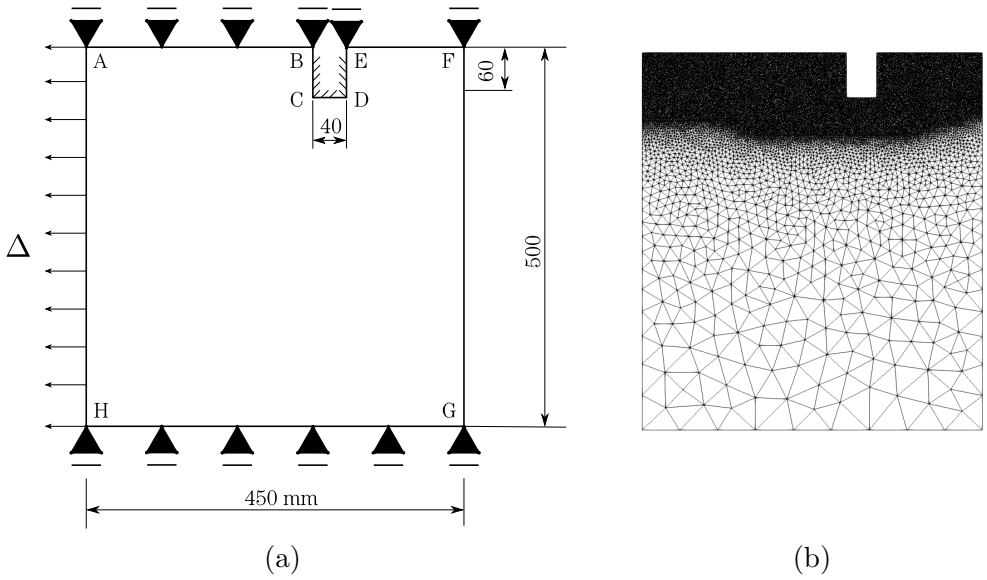

Figure 4.8: French Panthéon Fracture. (a) Problem setting, (b) T3 mesh.

As it can be seen in Fig. 4.8, the edge AH is subject to a horizontal and constant displacement; edges GH, AB and EF are fixed in vertical direction; and the nodes of edges BC, CD and DE are fixed.

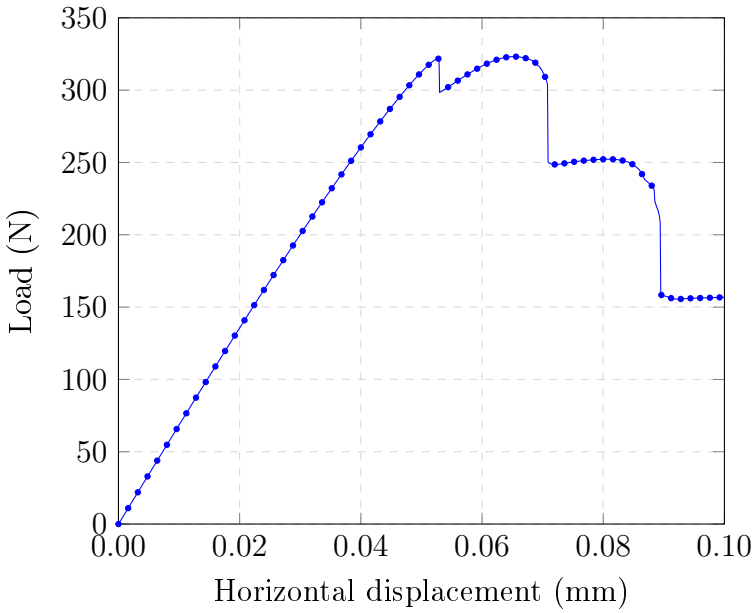

Figure 4.9: Load-displacement curve for french Panthéon fracture test.

The mesh has mean nodal distance of 50 mm, refined in the crack region with size of 2 mm. The analysis was subject to a plane strain state with the following material

parameters: $E_0 = 10000$ N/mm^2, $\nu = 0.1$, $G_c = 25.0 \times 10^{-3}$ N/mm and $l_0 = 5.0$ mm. It was considered displacement control with load-factor of 1×10^{-4} mm, convergence in

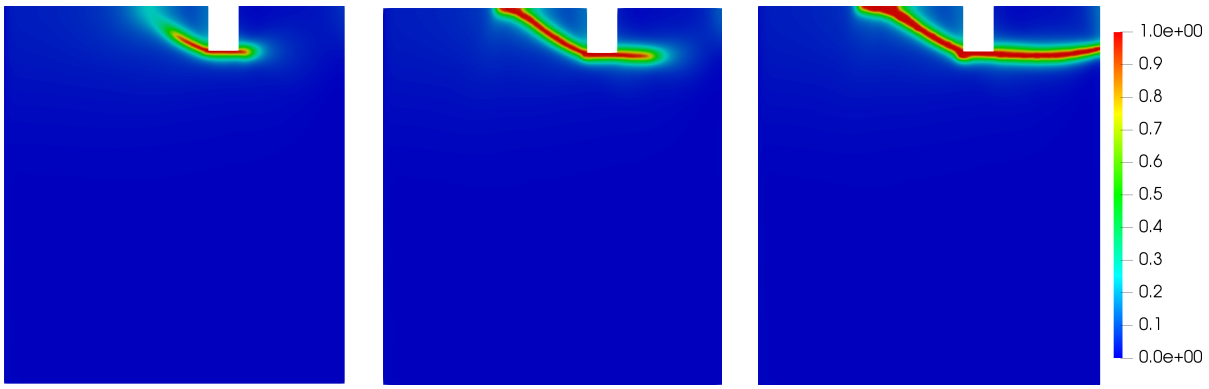

(a) (b) (c)

Figure 4.10: Phase-field evolution in french Panthéon fracture test. (a) $\Delta = 0.070$ mm, (b) $\Delta = 0.085$ mm, (c) $\Delta = 0.090$ mm.

displacement with local tolerance of 1×10^{-4} and global tolerance[2] of 1×10^{-3}.

The phase-field evolution shown in Fig. 4.10 are the same as those presented by Lancioni and Royer-Carfagni (2009), and the obtained load-displacement curve is depicted in Fig. 4.9.

It is important to emphasize that, in the tests performed in this work, this constitutive model has presented good results only in this test.

4.3.3 Amor et al. (2009) constitutive model

The implementation test of the constitutive model of Amor et al. (2009) had used the setting of Fig. 4.11. The nodes of the bottom edge are fixed in the vertical direction and the top edge is subjected to a vertical displacement, constant in all nodes. The plane strain state was considered with $E_0 = 1$ kN/mm^2, $\nu = 0.3$, $G_c = 1.0 \times 10^{-3}$ kN/mm and $l_0 = 0.02$ mm. The mesh has $h = 0.005$ mm in the refined region and $h = 0.04$ mm in unrefined region, where h is the mean nodal distance. The convergence was verified in displacement considering increments of 5×10^{-4} mm with local and global tolerance of 1×10^{-4} and 1×10^{-3}, respectively.

Fig. 4.12.a shows the crack path that is the same as that presented by Wu et al. (2020) and Fig. 4.12.b is the load-displacement curve of the top edge.

4.3.4 Miehe et al. (2010b) constitutive model

The problem setting and mesh are depicted in Fig. 4.13 in which a beam with size of $8 \times 2 \times 1$ mm^3 subjected to a plane stress state and constitutive model of Miehe et al.

[2]See Section 3.2.8

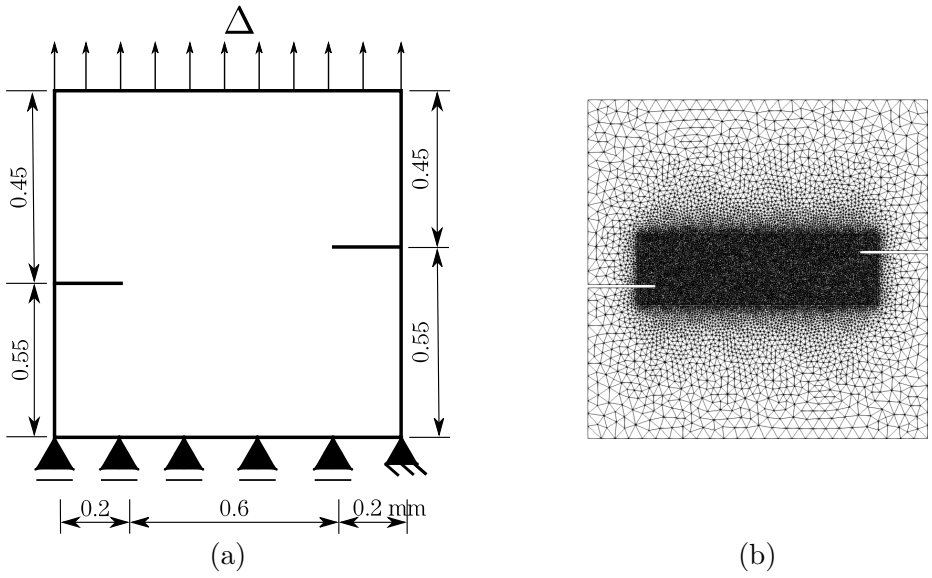

Figure 4.11: Asymmetric traction test. (a) Problem setting (Wu et al., 2020), (b) T3 mesh.

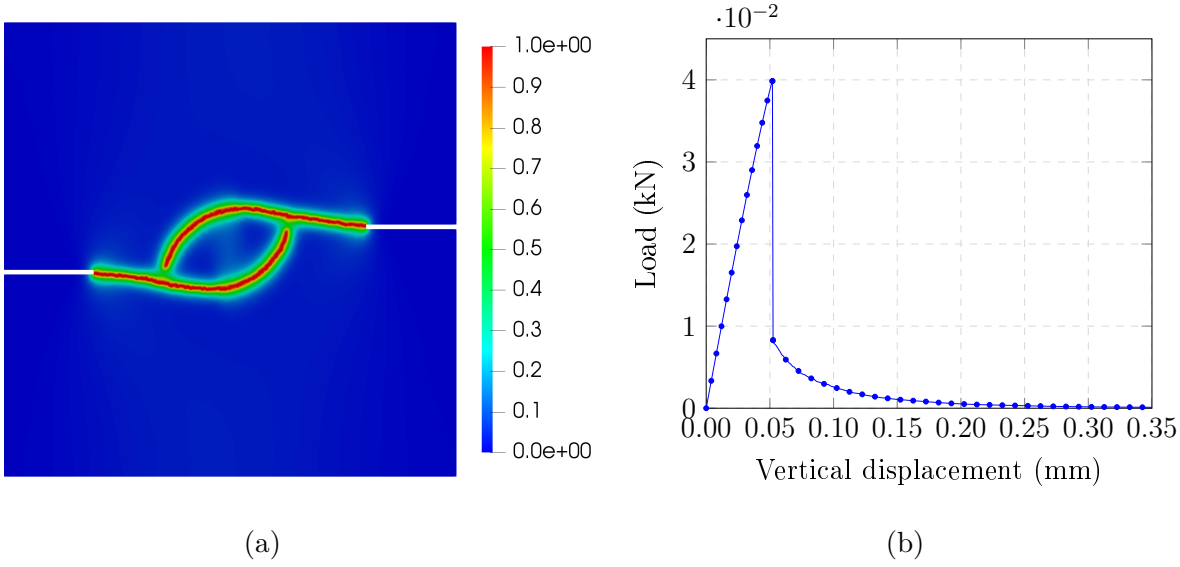

Figure 4.12: Results of asymmetric traction test. (a) Phase-field profile for $\Delta = 0.35$ mm, (b) Load-displacement curve of the top edge.

(2010b), was considered.

The mesh size is 0.0008 mm in the crack path (refined region) and 2.0 mm distant from that. The material parameters are: $E_0 = 20.8$ kN/mm^2, $\nu = 0.3$, $G_c = 0.5$ N/mm and $l_0 = 0.06$ mm.

In the analysis the horizontal displacement of the right crack mouth node was controlled with incremental displacements of 1×10^{-4} mm and tolerance of 1×10^{-4} in displacement. The results for phase-field profile and load-displacements curves are in Fig. 4.14. The obtained results are similar to those of Miehe et al. (2010a) with the ex-

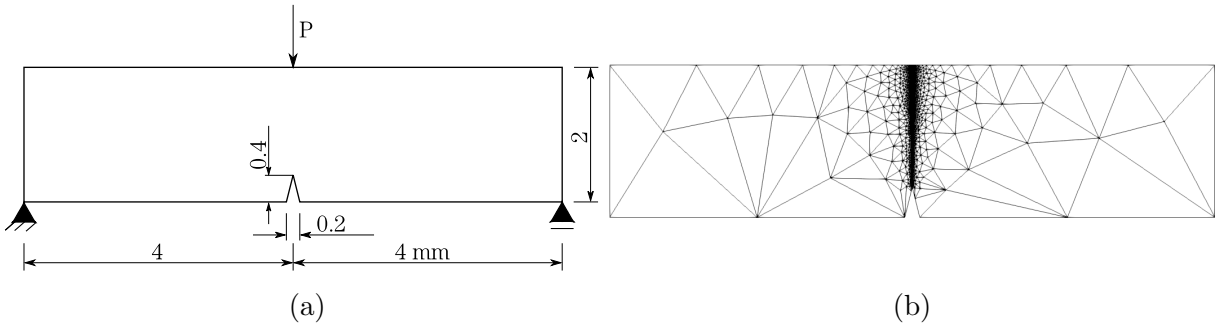

Figure 4.13: Miehe three bending test. Thickness of 1 mm (a) Problem setting (Miehe et al., 2010b), (b) T3 mesh.

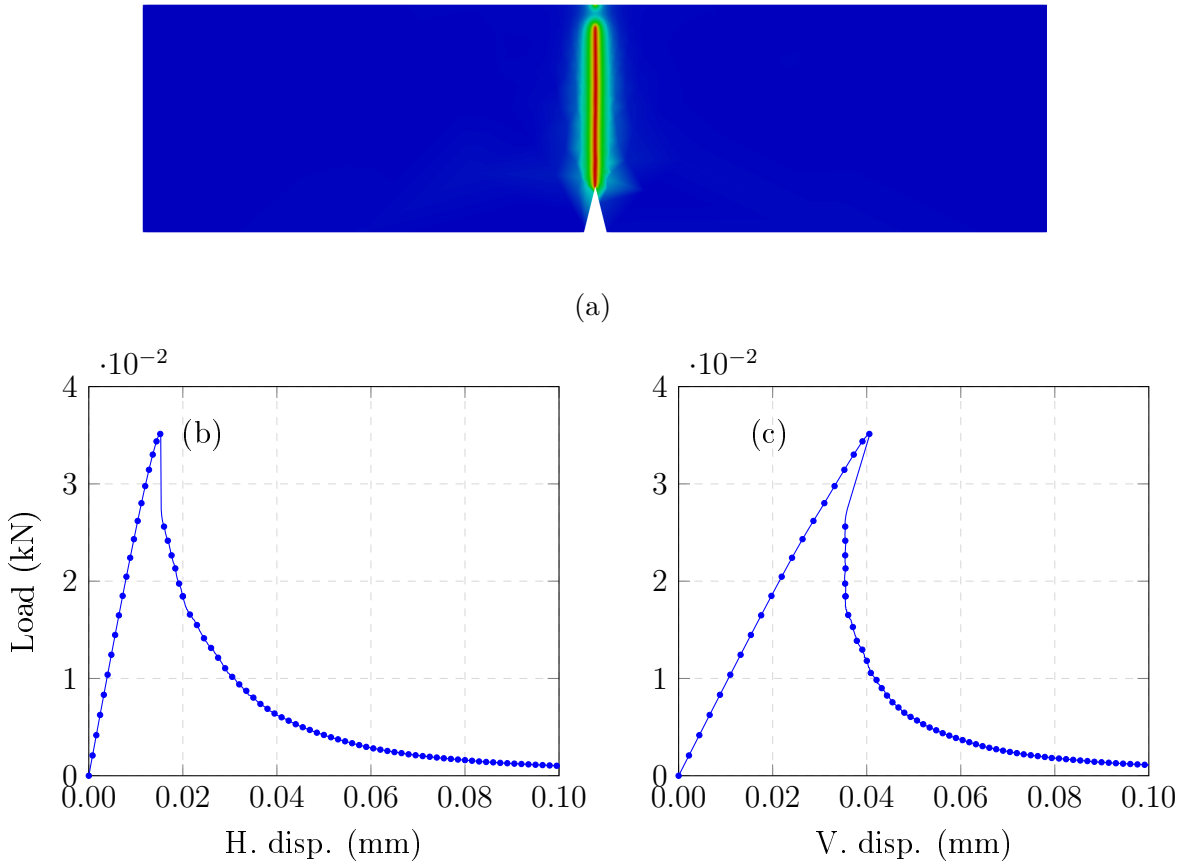

Figure 4.14: Results of Miehe et al. (2010b) bending test. (a) Phase-field profile in 1000th step, (b) Load-displacement curve of the horizontal displacement of the controlled node; (c) Load-displacement curve of the vertical displacement of the loading application node.

ception that Miehe et al. (2010a) is unable to obtain the snap back due to the adopted control node.

Chapter 5

Comparison between constitutive models

This chapter brings a comparison between the implemented constitutive models using a shear test and a tension test. In all examples were used $\alpha(\phi) = \phi^2$ and $g(\phi) = (1-\phi)^2$.

5.1 Shear test

The setting and mesh of Fig. 4.1 was used to compare the implemented constitutive models. The analyses resulted in the crack paths shown in Fig. 5.1 that are different from

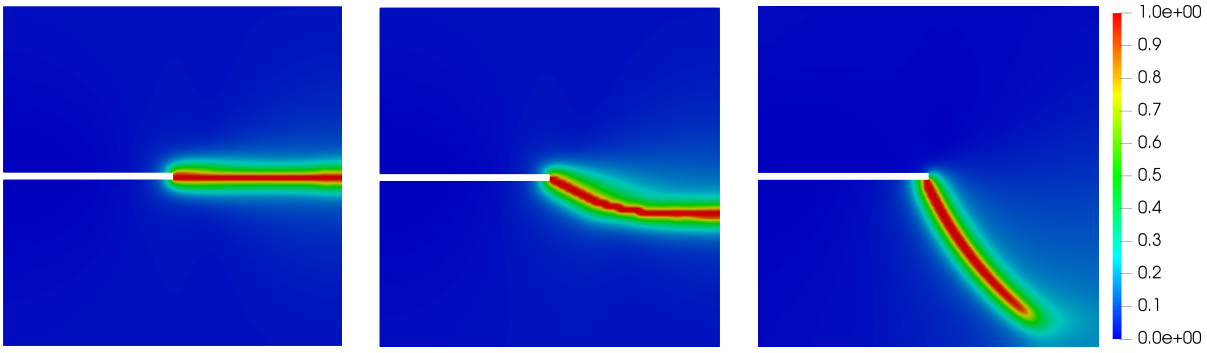

(a) (b) (c)

Figure 5.1: Phase-field profile for shear test. The mesh is depicted in Fig. 4.1.b and the constitutive models used are: (a) Lancioni and Royer-Carfagni (2009), (b) Amor et al. (2009), (c) Miehe et al. (2010b).

the already existent in the literature. Thus, a new mesh was generated (Fig. 5.2) and the analysis was done again.

The results obtained for Lancioni and Royer-Carfagni (2009) constitutive model indicates a horizontal crack growth. Therefore, another mesh was generated and the model

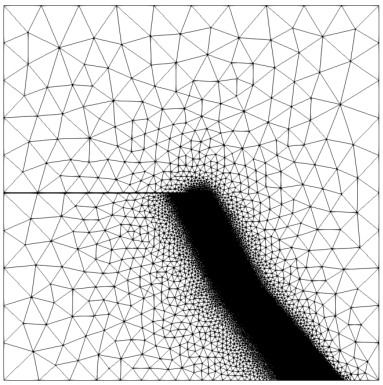

Figure 5.2: Refined mesh used in shear test. $h = 0.1$ mm in the unrefined region and $h = 0.002$ mm in the refined region.

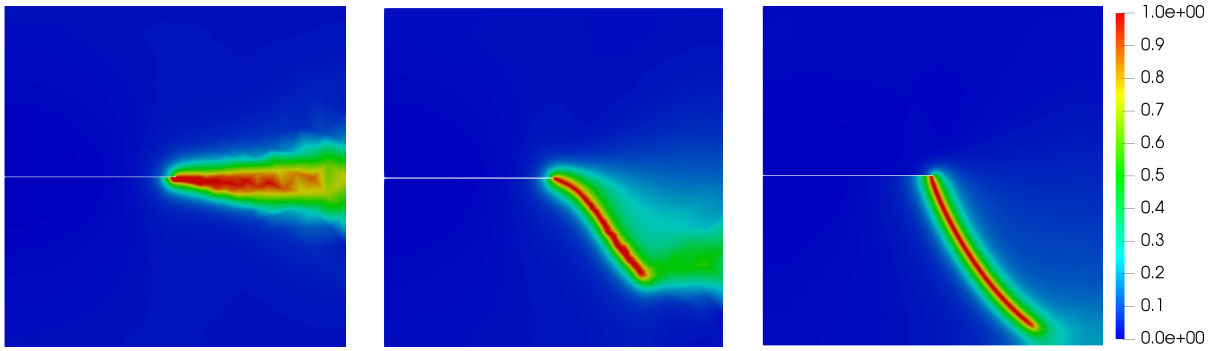

(a) (b) (c)

Figure 5.3: Phase-field profile for shear test. The mesh is depicted in Fig. 5.2 and the constitutive models used are: (a) Lancioni and Royer-Carfagni (2009), (b) Amor et al. (2009), (c) Miehe et al. (2010b).

was analysed over again. The mesh generated and results are presented in Fig. 5.4.

It can be noted that Lancioni and Royer-Carfagni (2009) constitutive model is very unstable and dependent on the mesh. It would be good to repeat the analysis considering the constitutive model of Lancioni and Royer-Carfagni (2009) and a refined mesh in all domain, but that is computationally expensive in such way that is impossible with the hardware utilized in this work.

The constitutive model of Amor et al. (2009) has presented a little instability but, after the refinement, the results agree with already existent in literature, and the constitutive model of Miehe et al. (2010b) was the most stable for this test.

The load-displacement curves obtained for each case are presented in Fig. 5.5.

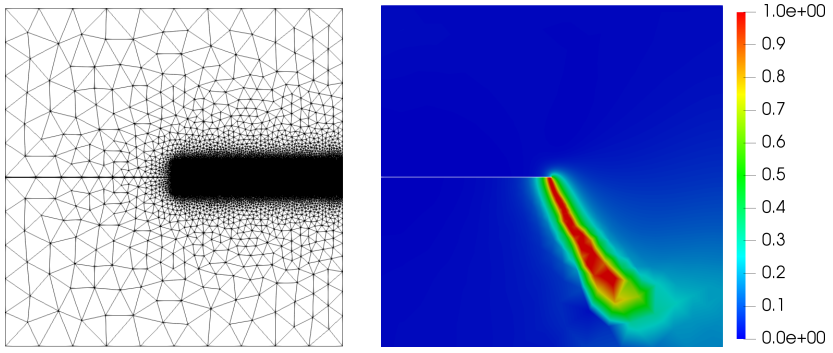

Figure 5.4: Phase-field profile for shear test and Lancioni and Royer-Carfagni (2009) constitutive model. (a) T3 mesh ($h = 0.1$ mm in the unrefined region and $h = 0.002$ mm in the refined region), (b) Phase-field evolution

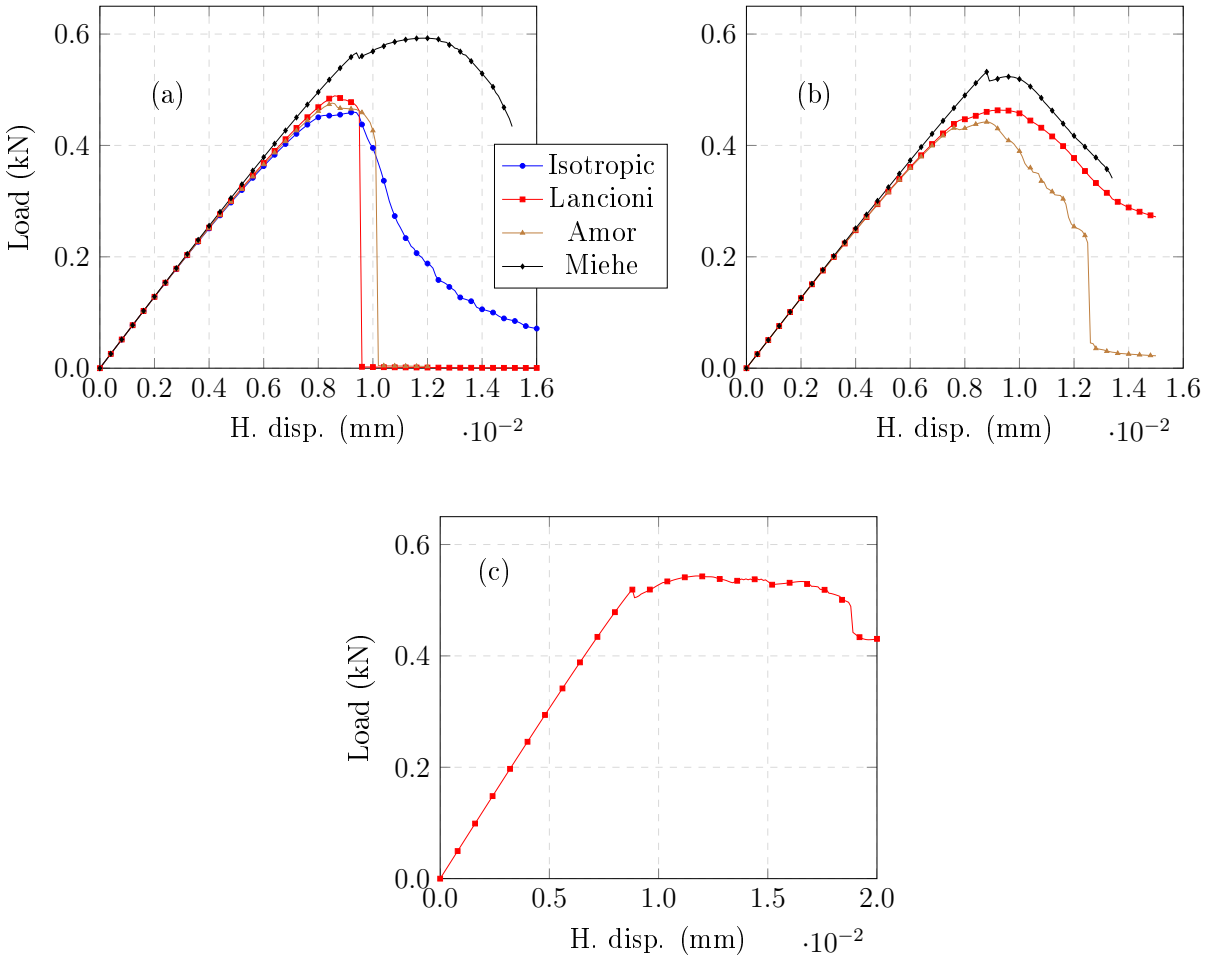

Figure 5.5: Load-displacement curves for shear test. (a) Q4 mesh, (b) Mesh of Fig. 5.2, (c) Mesh of Fig. 5.4.

5.2 Traction test

The setting and mesh utilized in this analysis are depicted in Fig. 5.6. The bottom edge

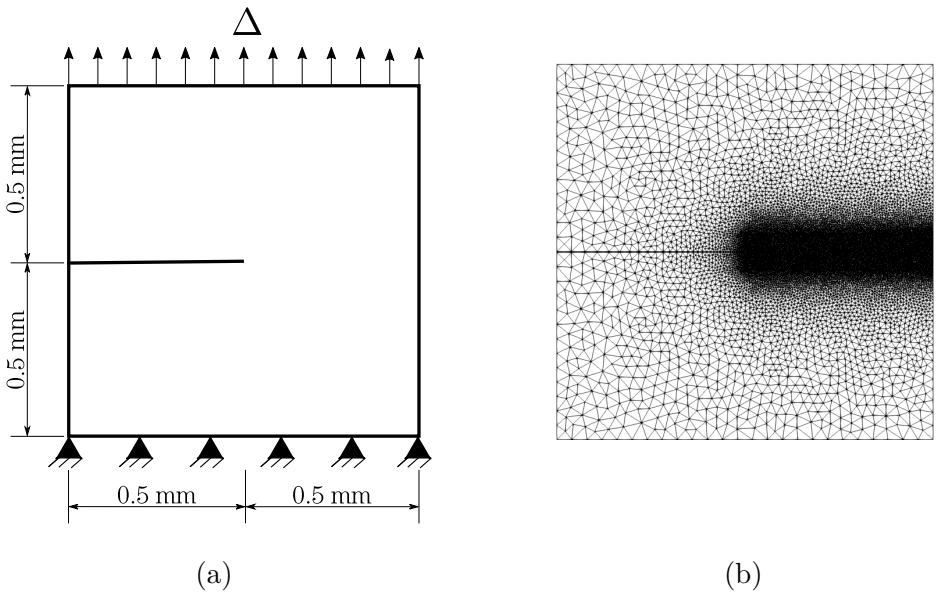

Figure 5.6: Traction test. (a) Problem setting, (b) T3 mesh ($h = 0.05$ mm in the unrefined region and $h = 0.001$ mm in the refined region).

is clamped in vertical direction and a vertical displacement increment of 1.0×10^{-4} mm is applied in all nodes of the top edge. The specimen is subjected to a plane strain

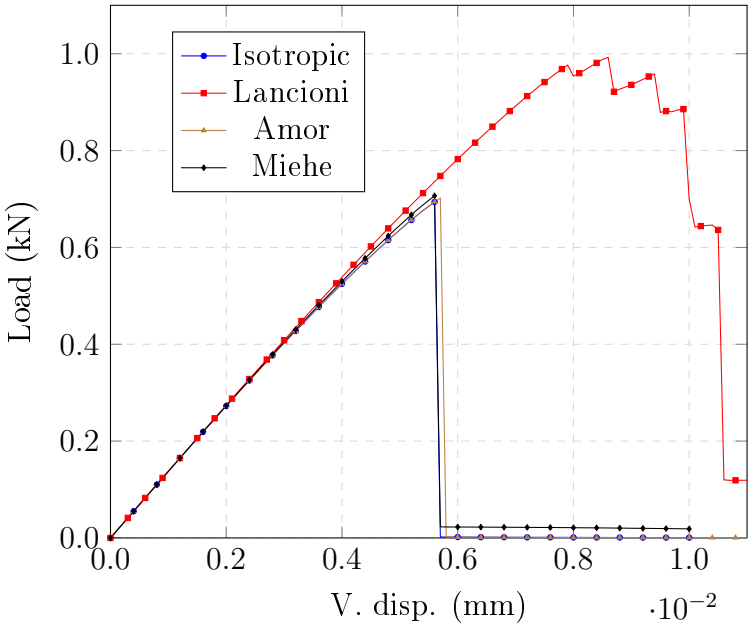

Figure 5.7: Load-displacement curves of the top edge for tension test.

state with $E_0 = 210$ kN/mm^2, $\nu = 0.3$, $G_c = 0.0027$ kN/mm and $l_0 = 0.015$ mm. The

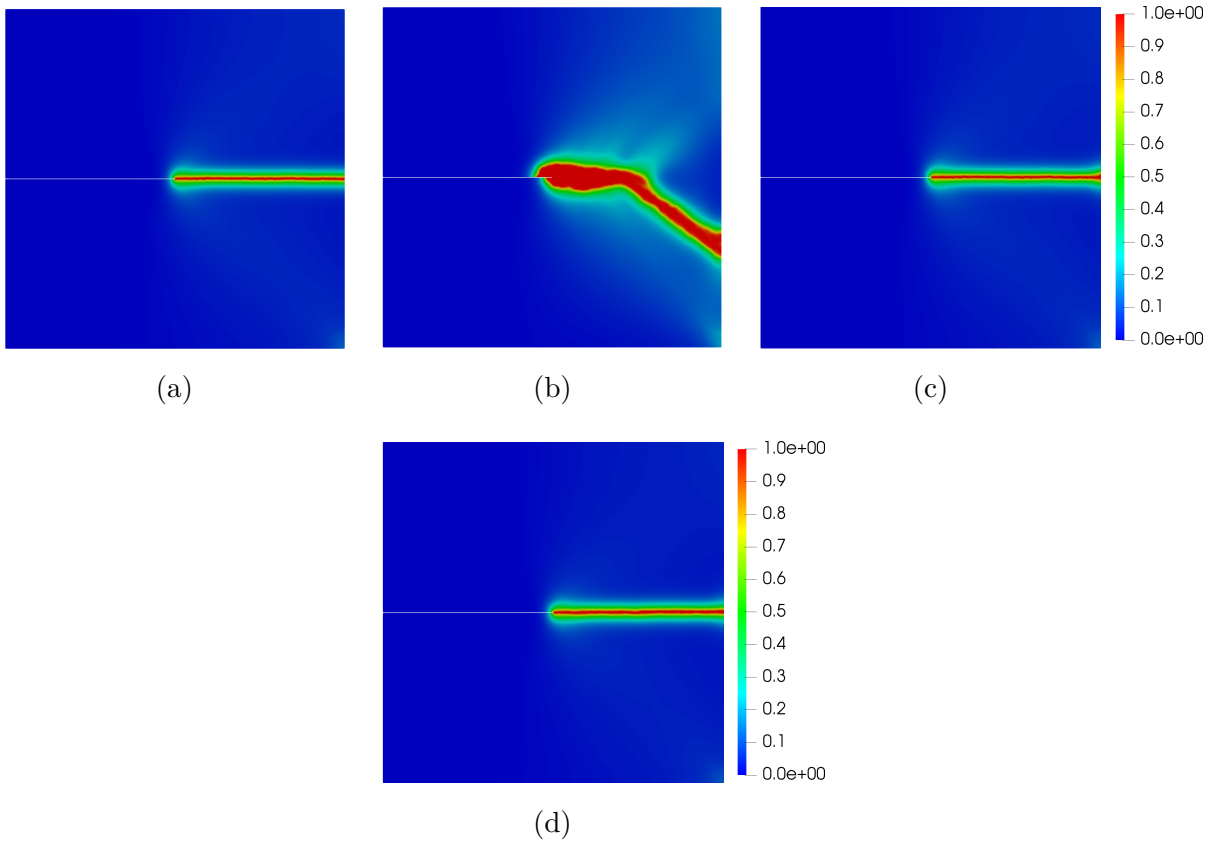

Figure 5.8: Phase-field profile for tension test. (a) Isotropic constitutive model, (b) Lancioni and Royer-Carfagni (2009) constitutive model, (c) Amor et al. (2009) constitutive model, (d) Miehe et al. (2010b) constitutive model.

convergence was verified in displacements with local tolerance of 1×10^{-4} and global tolerance of 1×10^{-3}.

The results obtained for load-displacement curve is presented in Fig. 5.7 and the crack path in Fig. 5.8.

It can be noted that, for this tension test, all constitutive models behaved the same way, except for the constitutive model of Lancioni and Royer-Carfagni (2009) that presented a much higher critical load and a different crack path.

Chapter 6

Material law and structural behaviour

The numerical study developed in this chapter aims to compare the behaviour of the phase-field strategy at the material and structural levels. To this purpose, an uniaxial analysis was first performed, with different values of the phase-field material parameters. Then, these parameters were used in a structural analysis. For the sake of comparison, the same analyses were also performed with an elastic degrading model, the classic smeared crack model (Borst and Gutiérrez, 1999, de Borst, 2002). It were used the constitutive model of Miehe et al. (2010a), $\alpha(\phi) = \phi^2$ and $g(\phi) = (1-\phi)^2$ in phase-field analysis.

6.1 Material behaviour

Starting from a bar under axial traction, Wu et al. (2020) obtained the analytical equations for the stress-strain curve of a generic phase-field model (See Appendix B). Considering the peculiarities of the model adopted in this paper, these equations can be expressed as:

$$\sigma = \sqrt{\frac{E_0 G_c}{l_0}\phi(1-\phi)^3}, \quad \varepsilon = \sqrt{\frac{G_c}{E_0 l_0}\frac{\phi}{1-\phi}} \tag{6.1}$$

As it can be observed, by fixing the elastic modulus (E_0), different materials exhibit the same stress-strain curve as long as the following ratio doesn't change.

$$g_c = G_c/(2l_0) \tag{6.2}$$

This feature has been confirmed by performing a finite elements analysis of an uniaxial problem using the material parameters of Table 6.1, whose results are illustrated in Fig. 6.1.

Table 6.1: Parameters of phase-field materials.

	E_0 (N/mm^2)	ν	G_c (N/mm)	l_0 (mm)
Material 1	25850	0.18	0.089	33.28
Material 2	25850	0.18	0.065	24.31
Material 3	25850	0.18	0.049	18.33

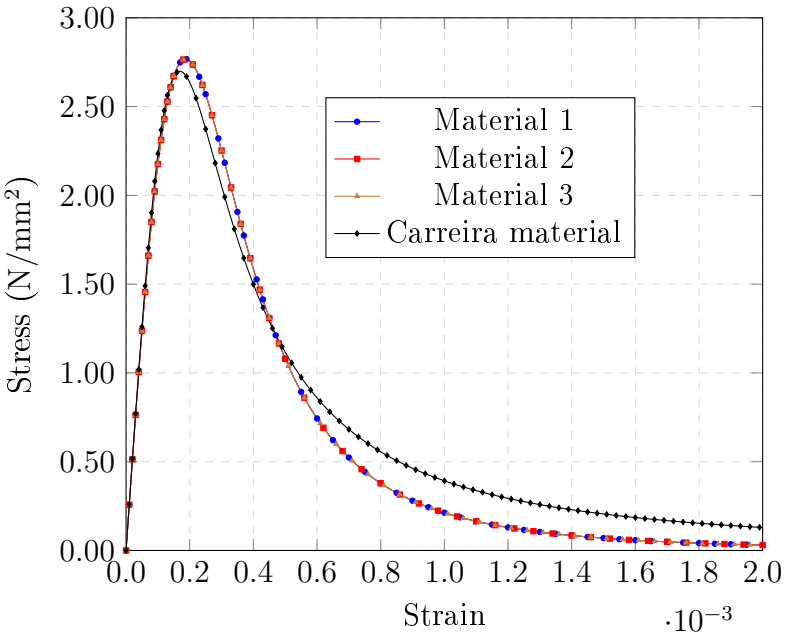

Figure 6.1: Stress-strain curves for materials presented in Table 6.1

Calculating the area below the phase-field material curve by the trapezoid rule the value 1.296×10^{-3} N/mm^2 is obtained. This value is close to $g_c = 1.337 \times 10^{-3}$ N/mm^2 obtained with Eq. (6.2), with a difference of 3.08%. It's worth to note that the definition of g_c given in Eq. (6.2) is similar to the ratio G_c/h, that in smeared crack models represents the area below the curve. Both h and $2l_0$ are closely related to the size of the degraded region.

Because of these similarities, the same uniaxial test were repeated with a smeared crack model, adopting the stress-strain curve proposed by Carreira and Chu (1985, 1986), hereinafter called Carreira material, presented below.

6.1.1 Carreira and Chu (1985, 1986) material

The behaviour of Carreira material can be described by:

$$\sigma_i = f_i \frac{k\left(\frac{\varepsilon}{\varepsilon_i}\right)}{k - 1 + \left(\frac{\varepsilon}{\varepsilon_i}\right)^k}, \qquad \text{with :} \quad k = \frac{1}{1 - \left(\frac{f_i}{\varepsilon_i E_0}\right)} \tag{6.3}$$

where $i = t, c$, σ_i is the tensile or compression stress, f_i is the tensile or compression strength, ε_i is the strain corresponding to the maximum stress (f_i), with $i = t$ for traction and $i = c$ for compression.

After a few attempts, the following values were reached in order to make Carreira material to approach the adopted phase-field material: $\varepsilon_t = 1.69 \times 10^{-4}$, $f_t = 2.7$ N/mm^2, $E_0 = 25850$N/mm^2, $\nu = 0.18$, $\varepsilon_c = 20.0$, $f_c = 300000.0$ N/mm^2. The very high values of ε_c and f_c are necessary to make the material behave linearly in compression like in phase-field model. The stress-strain curve of this material is also depicted in Fig. 6.1. The area below this curve is 1.475×10^{-3} N/mm^2, which is similar to the one of the phase-field material, with a difference of 13.8%.

6.2 Structural behaviour

The structural analysis used to test the material parameters illustrated in the previous section was based on the L-panel (Fig. 6.2.a) investigated by Winkler et al. (2004). It's worth to emphasize that here the objective is not to make a comparison with the experimental results provided by the aforementioned paper, but point out the differences of the phase-field approach when applied to material and structural analyses.

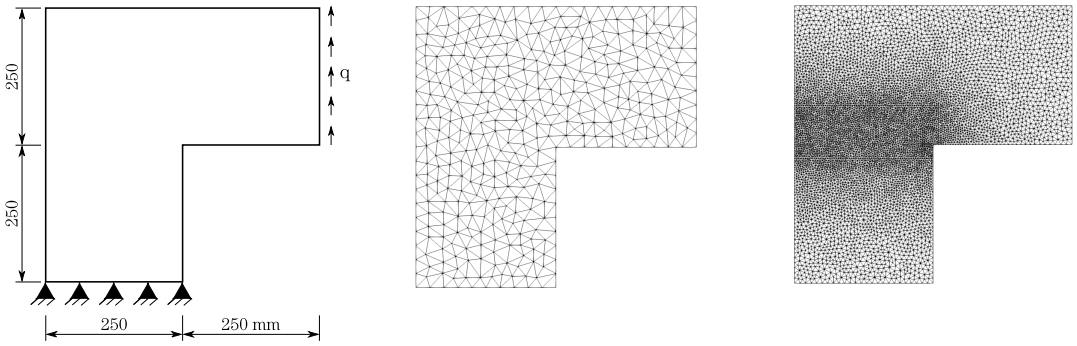

Figure 6.2: L-panel. Thickness of 100 mm. (a) Problem setting (Penna, 2011), (b) Mesh for smeared crack model (c) Mesh for phase-field model.

The panel was discretised with finite elements in a plane-stress state, with a thickness of 100 mm. Three-nodes triangular elements with a mesh size of 25 mm was considered in smeared crack model analysis. The phase-field analyses were instead performed with a mesh made of three-nodes triangular elements, with a mean nodal spacing of 10 mm in the unrefined region and 4 mm in the refined one. The nodal spacing in the phase-field model has been choosen according to the criteria usually adopted in the literature, that suggest a ratio between l_0 and the element size greater than 2 (Miehe et al., 2010a). This refined mesh can't be used in the smeared crack model analysis once it would cause localization effect (Borst, de et al., 1993, Peerlings et al., 2002, Gori, 2018).

The loading process was driven by the displacement control method with a reference load $q = 28$ N/mm, and adopting the reentrant corner node as the control node, where the vertical displacement was incremented of 5×10^{-4} mm. The convergence was measured in relative displacements, using 1×10^{-3} as a tolerance for the global convergence and 1×10^{-4} for the local convergence.

The load factor-displacement curves obtained for the structural analysis are depicted in Fig. 6.3. It can be observed that, even with similar material behaviour, the analyses

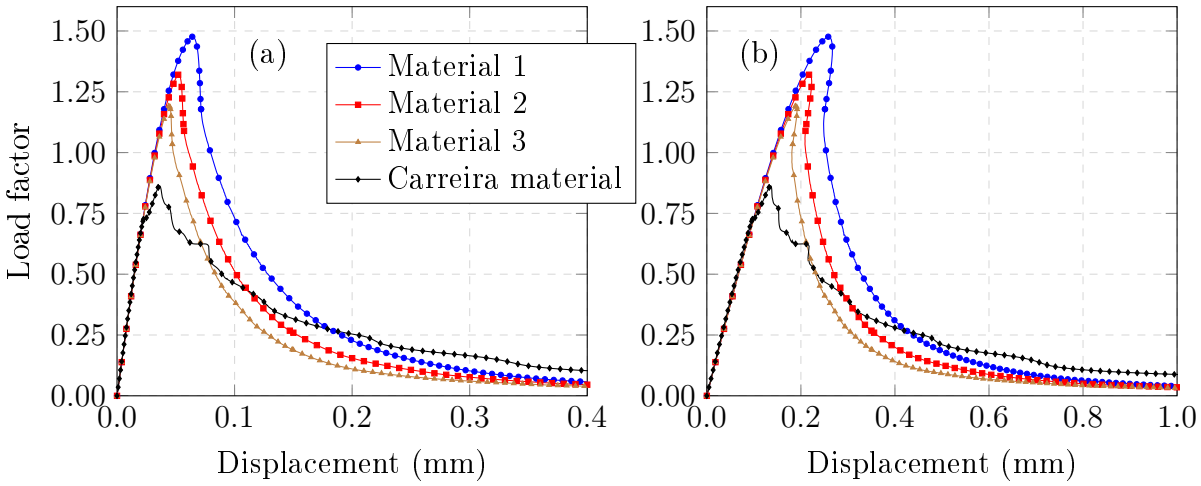

Figure 6.3: Load-displacement curve of L-Panel. (a) Vertical displacement of the reentrant corner node; (b) Vertical displacement of the lower node of the load application line.

lead to different structural responses presenting a higher load limit for materials with higher G_c and l_0 because, although l_0 is linked to the size of the degraded region, it is G_c that indicates the amount of energy that will be consumed to start the crack propagation, which will be later the greater the G_c. In order to illustrate the structural brittleness, Fig. 6.4 shows the normalized load-displacement curves, that were obtained by dividing the original values of load factors and displacements (Fig. 6.3) by the values concerning the limit load points. Fig. 6.4 shows that the phase-field analyses are similar to each other and more brittle than the smeared crack model once Miehe et al. (2010a) model are indicated to represent brittle fracture. One of the main factors that induce this behaviour is the adopted $g(\phi)$ function that depends only on ϕ and doesn't have any material strength limit on its formulation (Wu et al., 2020). Despite this limitation, it is still possible to study the size effect in phase-field models for a fixed material, as presented in Chapter 7.

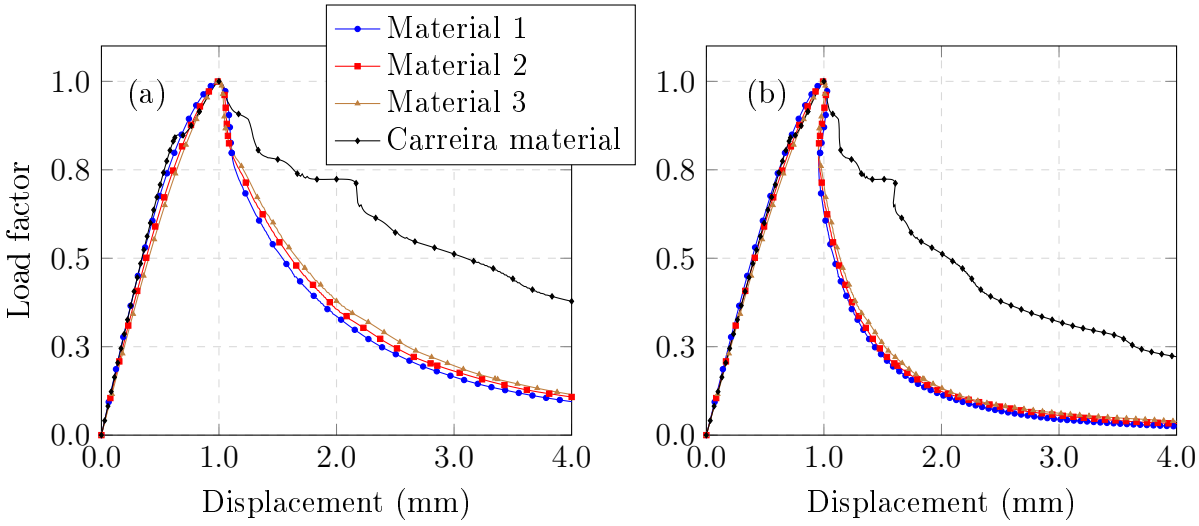

Figure 6.4: Normalized load-displacement curve of L-Panel. (a) Vertical displacement of the reentrant corner node; (b) Vertical displacement of the lower node of the load application line.

6.3 Influence of length scale (l_0) in degraded band

In this section the influence of the length scale in the degraded band will be analysed. For that the setting with the triangular mesh of Fig. 6.2.c will be used with $E_0 = 20000$ N/mm^2, $\nu = 0.18$ and $G_c = 0.130$ N/mm.

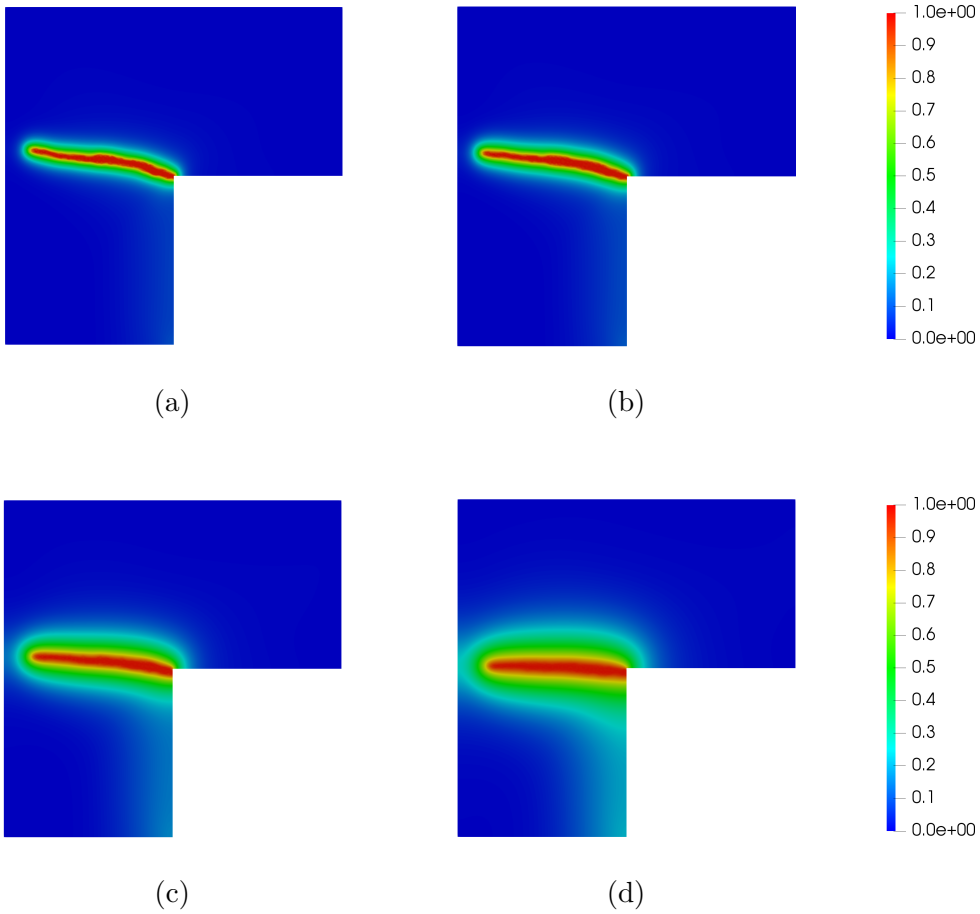

Figure 6.5: Phase-field profile in 1000th step. (a) $l_0 = 8$ mm, (b) $l_0 = 10$ mm, (c) $l_0 = 20$ mm, (d) $l_0 = 30$ mm.

The phase-field profiles obtained for various length scale parameters (l_0) depicted in Fig. 6.5 illustrates that the increase of the length scale increases the size of the degraded band, directly affecting the structural behaviour.

Chapter 7

Size effect

This chapter presents the size effect on failure load and brittleness obtained with the implemented phase-field model for the Brazilian splitting test and for a three-point bending test. It were used the constitutive model of Miehe et al. (2010b), $\alpha(\phi) = \phi^2$ and $g(\phi) = (1 - \phi)^2$.

7.1 Brazilian splitting test

The Brazilian splitting test of Fig. 7.1.a, with 26 mm of radius and 1 mm of thickness, was modelled as a plane stress state problem with $E_0 = 31500$ N/mm^2, $\nu = 0.25$, $G_c = 0.1$ N/mm and $l_0 = 1$ mm, as suggested by Zhou et al. (2018). At the top and bottom

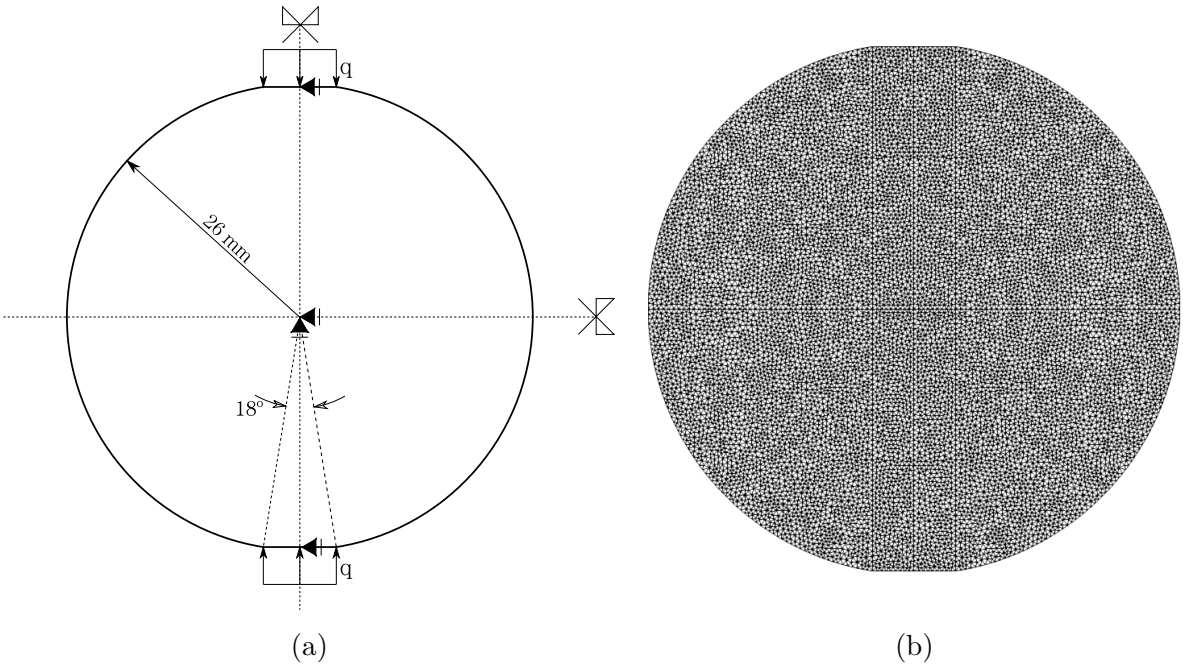

Figure 7.1: Diametrical compression setting. (a) Full setting (Zhou et al., 2018), (b) Triangular (T3) mesh with mean nodal distance of 0.5 mm across the domain.

of the cylinder is applied a symmetric line load ($q = 1$ N/mm, the reference value) in a short strip[1] of 18°.

Initially, to better demonstrate the phase-field evolution, the entire cylinder with no initial crack and the triangular mesh depicted in Fig. 7.1.b was considered. The nonlinear analysis was driven by controlling the horizontal displacement of the first node to the right of the center with increments of 1×10^{-5} mm. The convergence was verified in residual force with global and local tolerance of 1×10^{-3} and 1×10^{-4}, respectively. The evolution of the phase-field profile is illustrated in Fig. 7.2.

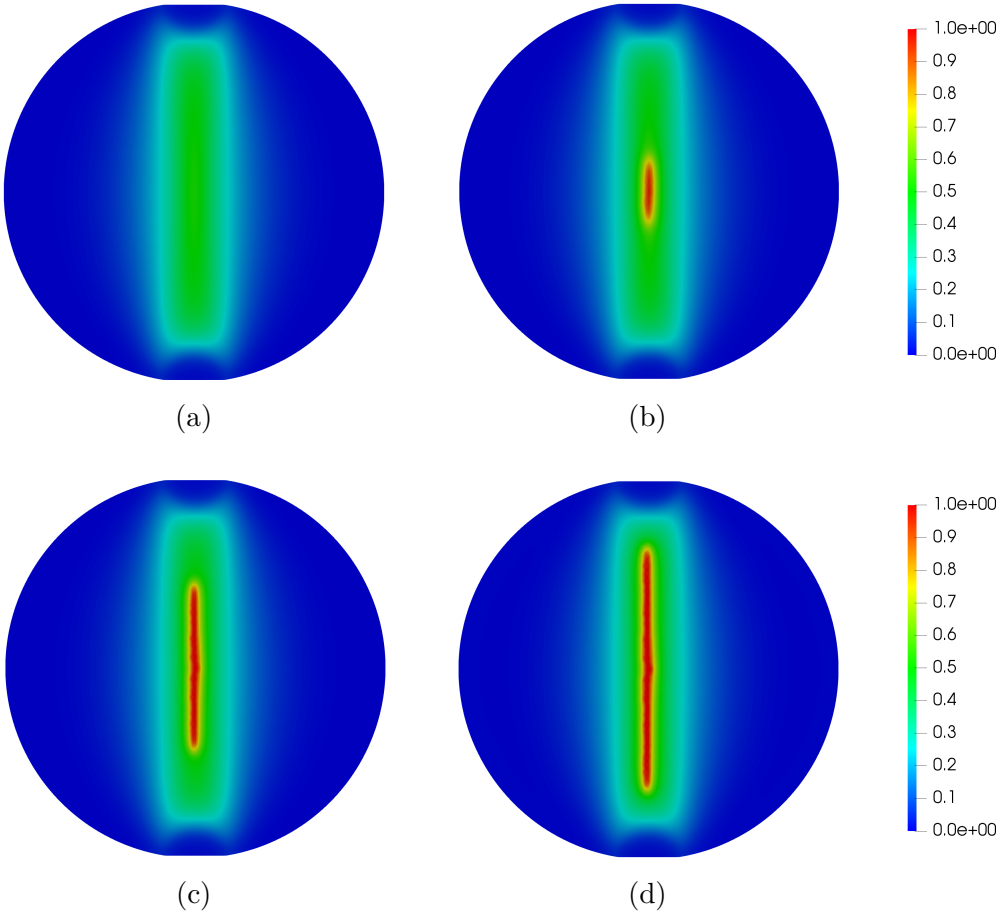

Figure 7.2: Phase-field profile for various analysis step. (a) Step 100, (b) Step 400, (c) Step 700, (d) Step 1000.

Now, in order to investigate just the size effect, taking advantage of the problem symmetry, just a quarter of the cylinder was modelled as depicted in Fig. 7.3. The controlled node and the parameters of the nonlinear analysis were the same for the complete cylinder. The load factor-displacement curves of the rightmost node, obtained for various initial crack size (c) are presented in Fig. 7.4.

The nominal resistance of the cylinder (σ_r) in the Brazilian test can be calculated by

[1]The dimension of the load strip has large influence in the crack evolution, as pointed out by Bahaaddini et al. (2019).

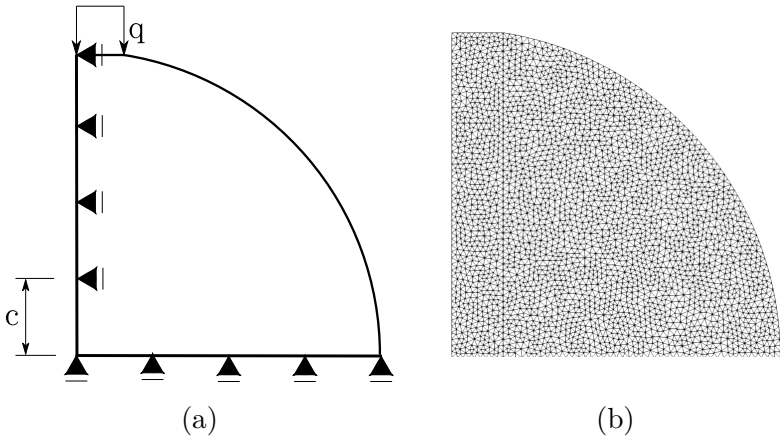

Figure 7.3: Diametrical compression setting, taking advantage of symmetry. (a) Problem setting. Parameter c is the initial crack size, (b) T3 mesh ($h = 0.5$ mm).

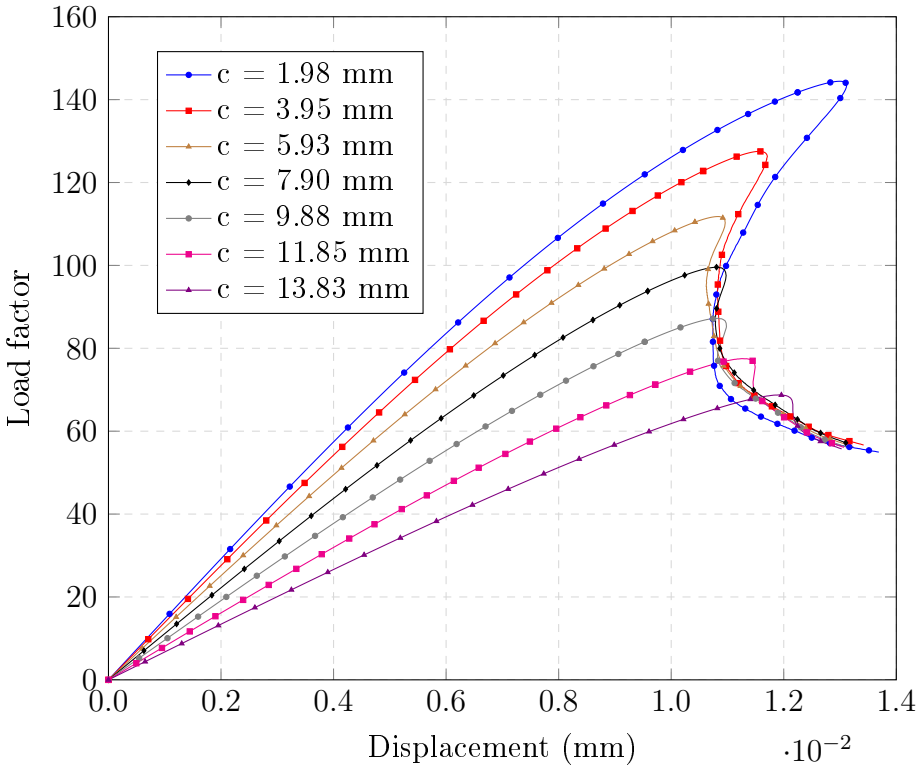

Figure 7.4: Load factor-displacement curve of the rightmost node, for various initial crack size.

the formula (Planas et al., 1999):

$$\sigma_r = \frac{2P_{max}}{\pi D_{ef} L} \tag{7.1}$$

where P_{max} is the maximum load, D_{ef} if the effective diameter and L is the length of the cylinder. From Eq. (7.1), Fig. 7.5 was plotted to relate the nominal resistance with the effective diameter, and as it can been seen, the nominal strength decreases with increasing effective diameter at first, and then that behaviour is reversed, a qualitative behaviour that has been observed in experimental tests (Bazant et al., 1991, Hasegawa and Okada,

1985).

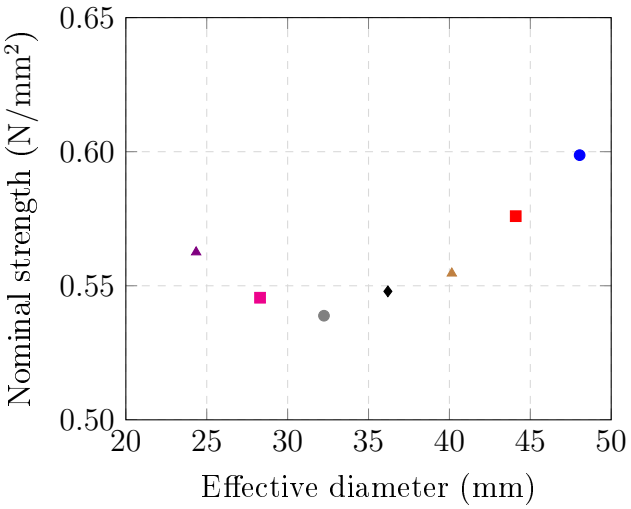

Figure 7.5: Relation between the nominal resistance with the effective diameter in diametrical compression.

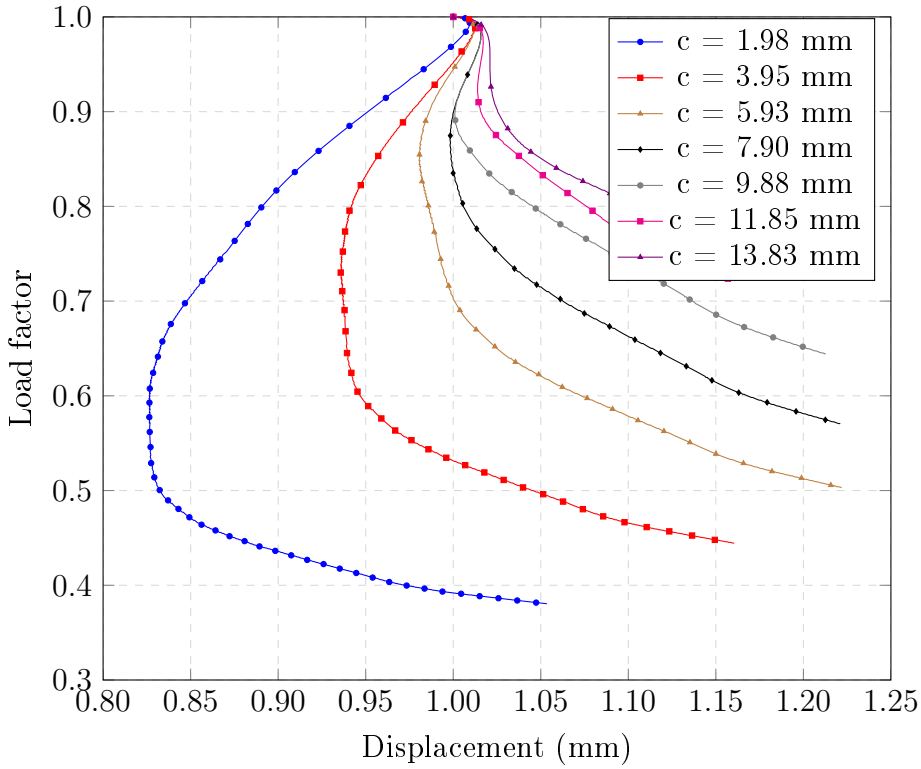

Figure 7.6: Descending branches of the normalized load factor-displacement curve of the rightmost node, for various initial crack sizes.

In order to discuss the size effect on the brittleness of the cylinder, the same aforementioned normalized curves have been used. Fig. 7.6 shows the curves concerning the descending branches only, and as it can be seen the brittleness increases with increasing effective diameter, a qualitative behaviour that has been observed in experimental tests

(Santos, 2015).

7.2 Bending Test

To verify the size effect on failure load and brittleness of a beam under bending, the setting of Fig. 7.7 is considered, where c is the initial crack length. The beam has thickness of

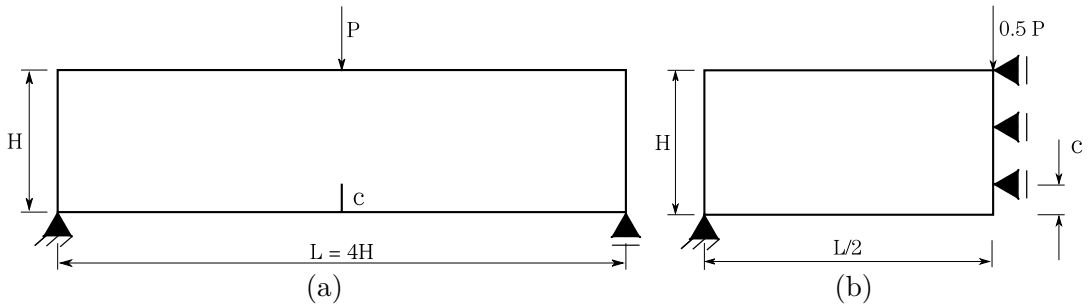

Figure 7.7: Size effect in 3-point bending. $P = 1$ N, the reference value. (a) Problem setting (Penna, 2011), (b) Modelling, taking advantage of symmetry.

36 mm and it was modelled as a plane stress state problem. Due to the symmetry, just half of the beam was modelled for different values of H (360, 480, 600, 720 and 840 mm) and $c = 60$ mm, taken constant.

The meshes were composed by quadrilateral elements (Q4) with size of 20×20 mm and the following material parameters: $E_0 = 44000$ N/mm^2, $\nu = 0.25$, $G_c = 0.164$ N/mm, $l_0 = 50$ mm. In order to prevent crack propagation near the left support, a G_c value ten times larger was adopted in the element with restraints.

The nonlinear analysis was driven by controlling the horizontal displacement of the node on the left side of the crack mouth, with increments of 1×10^{-3} mm. The convergence was verified in relative displacements with global and local tolerance of 1×10^{-3} and 1×10^{-4}, respectively.

The obtained load-displacement curves for the vertical displacement of the point where the load is applied are depicted in Fig. 7.8 and, as it can been seen, the bigger beam has a higher maximum load value and presents a less brittle behaviour.

To better verify the size on structural strength, a nominal value (σ_r) can be calculated by (Planas et al., 1999):

$$\sigma_r = \frac{3P_{max}L}{2th_{ef}^2} \tag{7.2}$$

where P_{max} is the maximum load, L is the beam length, t is the thickness and h_{ef} is the effective height. From Eq. (7.2), Fig. 7.9 was plotted to relate the nominal strength with the effective height, and it was verified that the increasing of the effective height decreases the beam strength, a qualitative behaviour that has been observed in experimental studies Bazant and Pfeiffer (1987), Perdikaris and Romeo (1995).

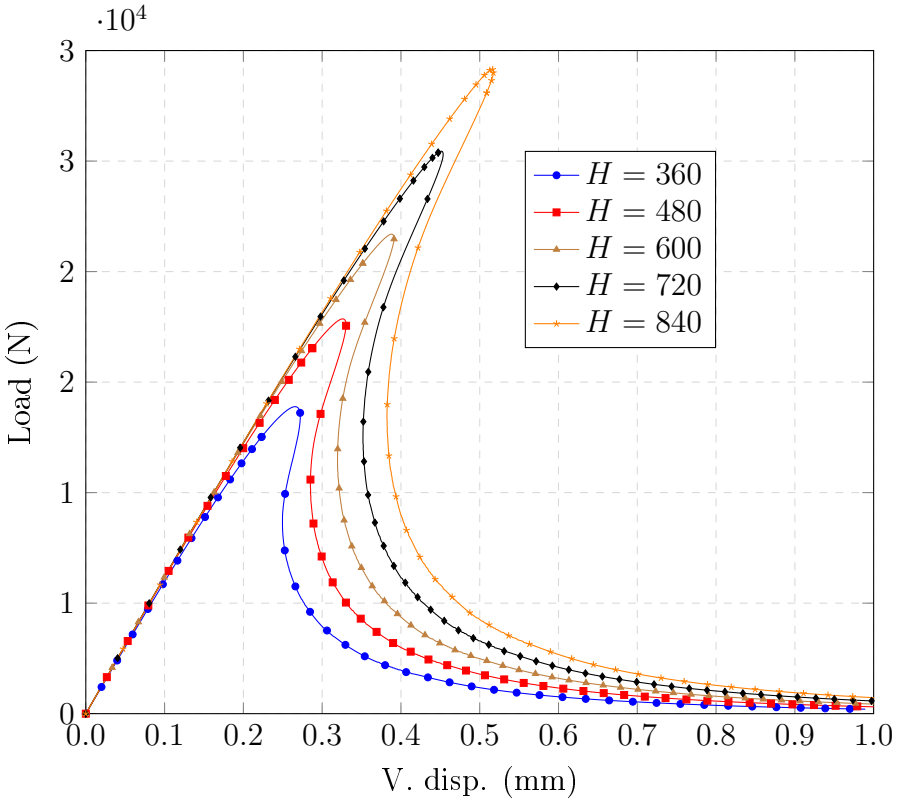

Figure 7.8: Load-displacement curves for the loading application node.

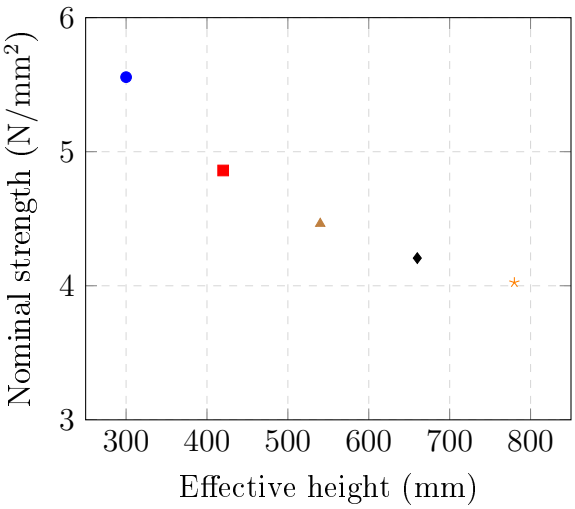

Figure 7.9: Relation between the nominal resistance with the effective height in 3 point bending test.

In order to discuss the size effect on the brittleness of the beam, normalized curves has been used. Fig. 7.10 shows the curves concerning the descending branches only, and as it can be seen the brittleness increases with increasing effective height, a qualitative behaviour that has been observed in experimental tests (Gettu et al., 1990, Santos, 2015).

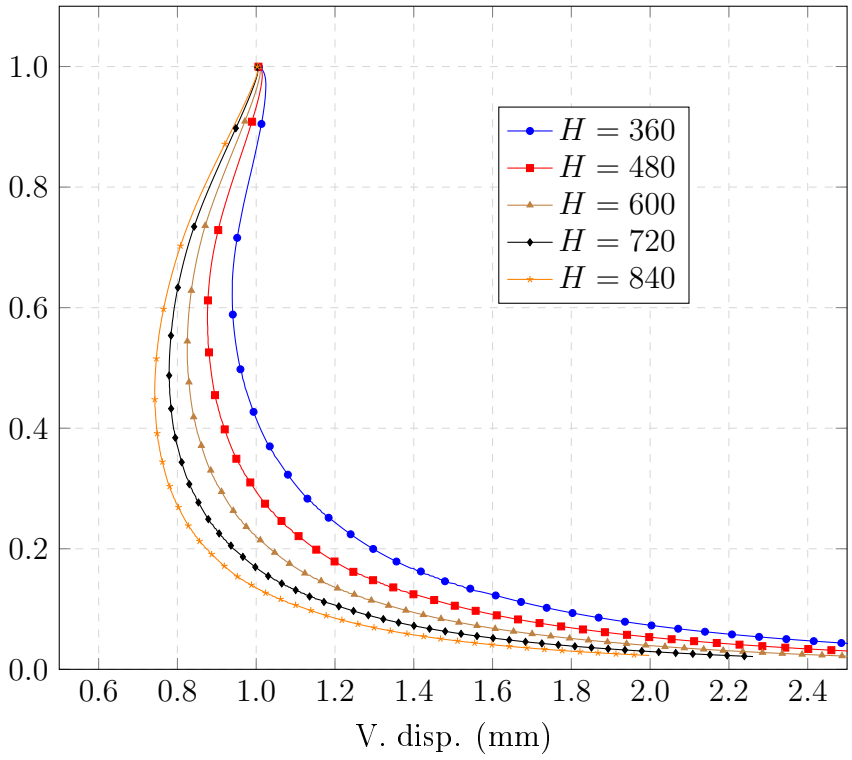

Figure 7.10: Descending branches of the normalized load-displacement curves for the vertical displacement where the load is applied.

Chapter 8

Ability to detect crack nucleation

This chapter presents some examples that verify the ability of the phase-field modelling to detect crack nucleation. Even though the problem is symmetric, it was decided to model it completely to better visualize the evolution of the phase-field. The mesh size was also considered constant in all domain. It was used $\alpha(\phi) = \phi^2$, $g(\phi) = (1-\phi)^2$ and Miehe et al. (2010b) constitutive model.

8.1 3 point bending

In this example it was used the setting, mesh and material defined in Section 7.2 for the beam with size $1440 \times 360 \times 36\text{mm}^3$ without the initial crack.

In the analysis it was controlled the horizontal displacement of the bottom edge right node with increments of 0.001 mm. It was considered convergence in displacements with tolerance of 1×10^{-3}.

The phase-field evolution is presented in Fig. 8.1.

8.2 4 point bending test

This example consists in a beam with size of $600 \times 150 \times 120\text{mm}^3$ (Fig. 8.2). In the analysis it is considered a plane stress state, $P = 1$ N, $E_0 = 31400$ N/mm^2, $\nu = 0.20$, $G_c = 0.275$ N/mm and $l_0 = 47.5$ mm. The mesh is composed by triangular elements with size of 3 mm. It was controlled the vertical displacement of the top edge central node with increments of 0.001 mm. The convergence was verified in displacements with tolerance of 1×10^{-3}.

The phase-field evolution is depicted in Fig. 8.3.

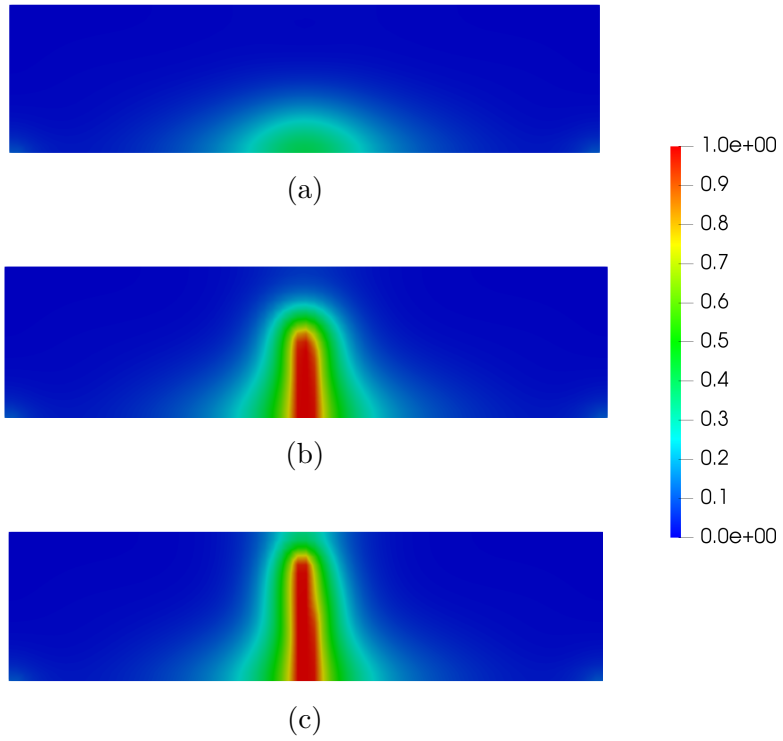

Figure 8.1: Phase-field evolution for 3 point bending test without initial crack. (a) $\Delta = 0.20$ mm, (b) $\Delta = 0.25$ mm, (c)$\Delta = 0.50$ mm.

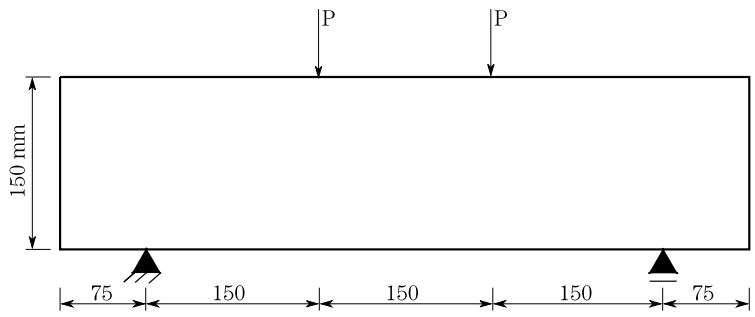

Figure 8.2: Four point bending without initial crack. Thickness of 120 mm.

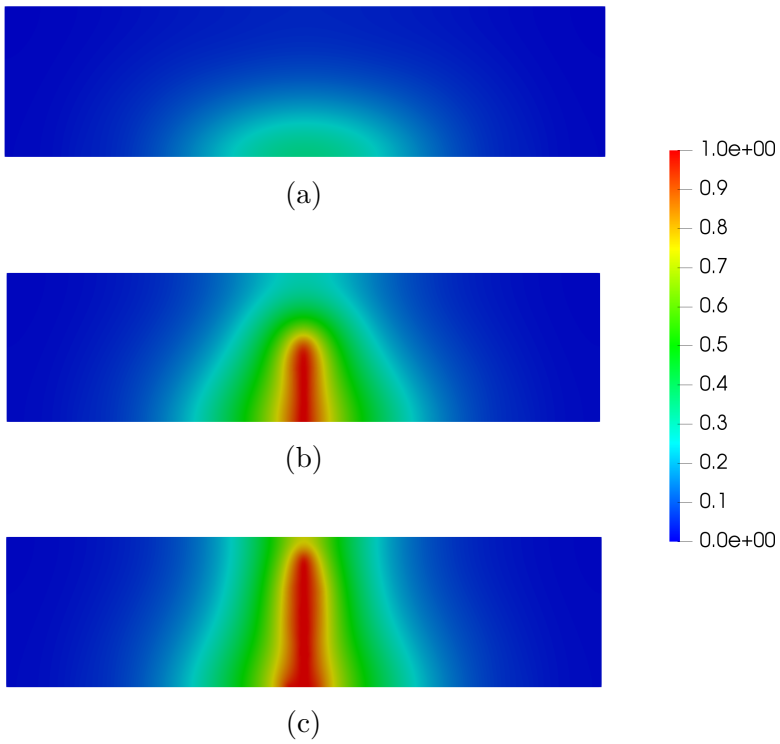

(a)

(b)

(c)

Figure 8.3: Phase-field evolution for 4 point bending test without initial crack. (a) $\Delta = 0.15$ mm, (b) $\Delta = 0.20$ mm, (c)$\Delta = 0.50$ mm.

8.3 Two failure modes of a beam

In the problem depicted in Fig. 8.4, adapted from Simão (2003), two different tests were considered. For each of them the value of x and the material parameters are related in Table 8.1. The structure was subjected to a plane stress state and it was discretized in

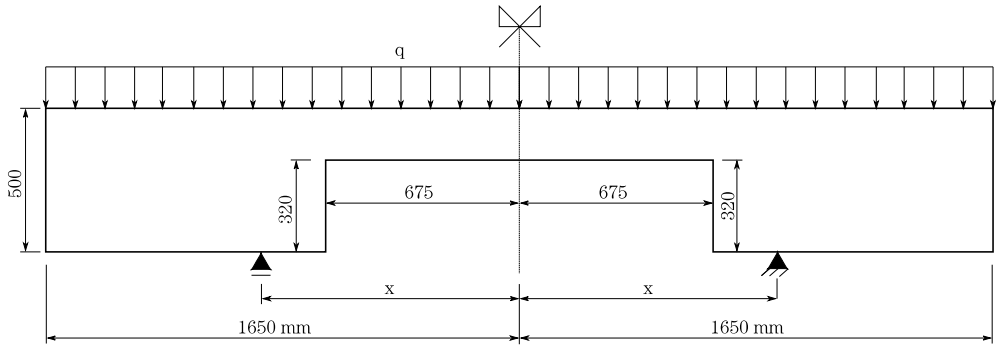

Figure 8.4: Two failure modes of a beam without initial crack. Thickness of 120 mm.

triangular (T3) elements with mean nodal distance of 15 mm across the domain. The reference load was defined as $q = 1$ kN/m.

In the Test 1 the problem was driven by controlling the vertical displacement of the bottom edge central node with increments of 0.005 mm and, in the Test 2, the vertical displacement of the rightmost bottom node was controlled with increments of 0.001 mm. The convergence was verified in relative displacements with global and local tolerance of 1×10^{-3}.

Table 8.1: Considered values for each test.

	E_0(kN/mm^2)	G_c(kN/mm)	l_0(mm)	x (mm)
Test 1	25	35×10^{-6}	67.6	928.60
Test 2	18	41×10^{-6}	67.6	859.50

Figs. 8.5 and 8.6 presents the phase-field evolution. The difference in the failure mode observed in both cases is because the changing of the support position also changes the location where the highest tensile stress, responsible for crack growing, occurs. It also important to emphasize that in Test 2 the solution had localized and the crack just grows in the right side, but that could occur in the left side, or both, depending on the mesh.

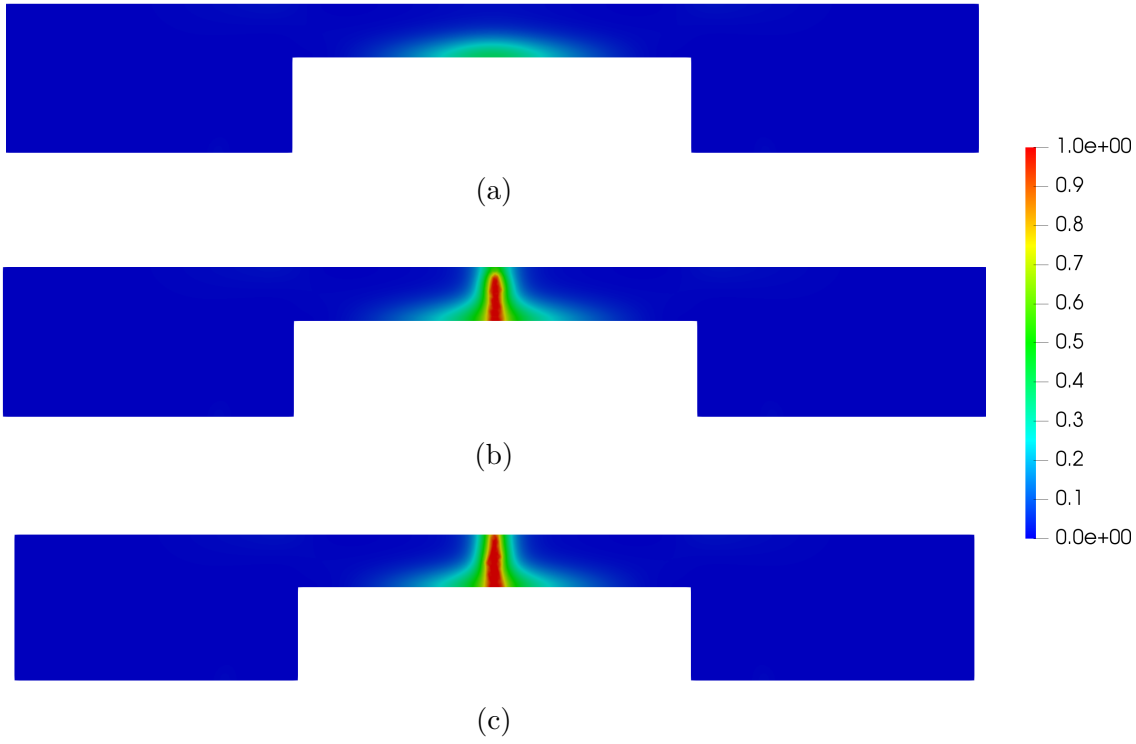

Figure 8.5: Phase-field evolution for Test 1. (a) $\Delta = 0.50$ mm, (b) $\Delta = 0.75$ mm, (c)$\Delta = 1.50$ mm.

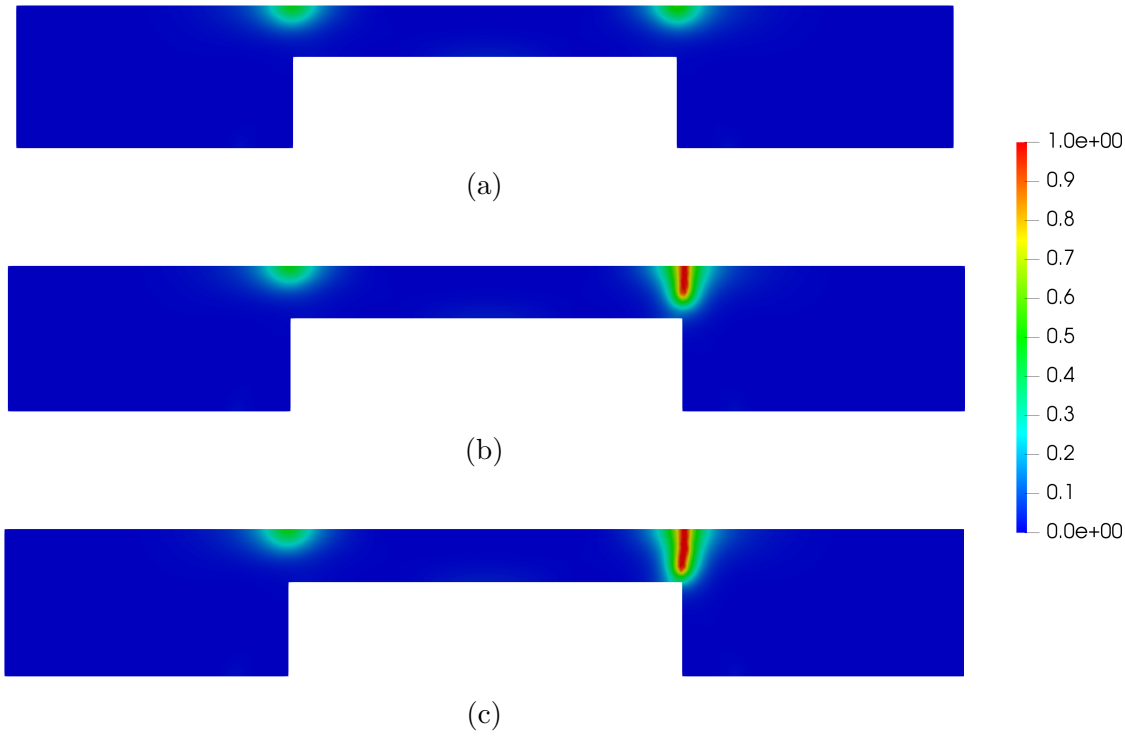

Figure 8.6: Phase-field evolution for Test 2. (a) $\Delta = 0.50$ mm, (b) $\Delta = 0.60$ mm, (c)$\Delta = 1.0$ mm.

Chapter 9

Miscellaneous examples

During the present study, it was noticed that, even with a different load-displacement curve, the model of Miehe et al. (2010b) was able to correctly describe the crack path. Therefore, the purpose of this chapter is to perform some examples already existent in literature by the Miehe et al. (2010b) constitutive model to obtain the load-displacement curves for that model. $\alpha(\phi) = \phi^2$ and $g(\phi) = (1-\phi)^2$ was considered.

9.1 Three point bending

The 3-point beam test according to RILEM[1] predictions for experimental measurement of fracture energy, as presented in Khalilpour et al. (2019), (Fig. 9.1) was performed using the phase-field constitutive model with $E_0 = 25850$ N/mm^2, $\nu = 0.18$, $G_c = 0.089$ N/mm and $l_0 = 33.28$ mm.

The mesh is composed by triangular elements (T3) with mean nodal distance of 1 mm in the refined region and 10 mm elsewhere. The horizontal displacement of the right mouth crack node was controlled with increments of 0.001 mm and the convergence was verified in displacements with global and local tolerance of 1×10^{-3}. The obtained load-displacement curves and the phase-field profile are in Figs. 9.2 and 9.3.

According to Khalilpour et al. (2019) the fracture energy (G_c) can be obtained from load-vertical displacement curve (Fig. 9.2) by

$$G_c = \frac{\text{Area above the curve}}{b(d-a)} \tag{9.1}$$

where b is the beam thickness, d is its height and a the initial crack size. Integrating Fig. 9.2.b by the trapezoid rule, and applying that equation it obtains $G_c = 0.106$ N/mm.

[1]RILEM (Réunion Internationale des Laboratoires et Experts des Matériaux, systémes de construction et ouvrages) is an association created to promote scientific cooperation in the area of construction materials and structures. In RILEM (1985), it has proposed dimensions and relation to determine the fracture energy in a bending test.

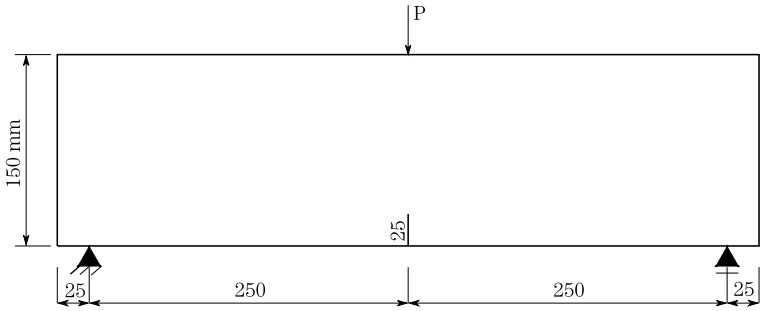

(a)

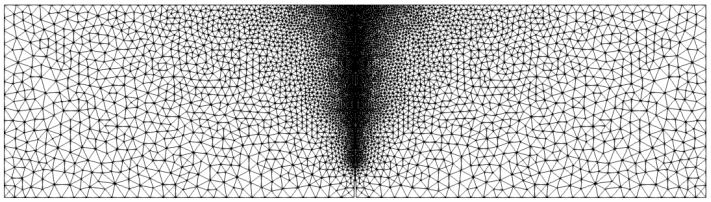

(b)

Figure 9.1: Three point bending test. Thickness of 150 mm. (a) Problem setting (Khalilpour et al., 2019), (b) T3 mesh.

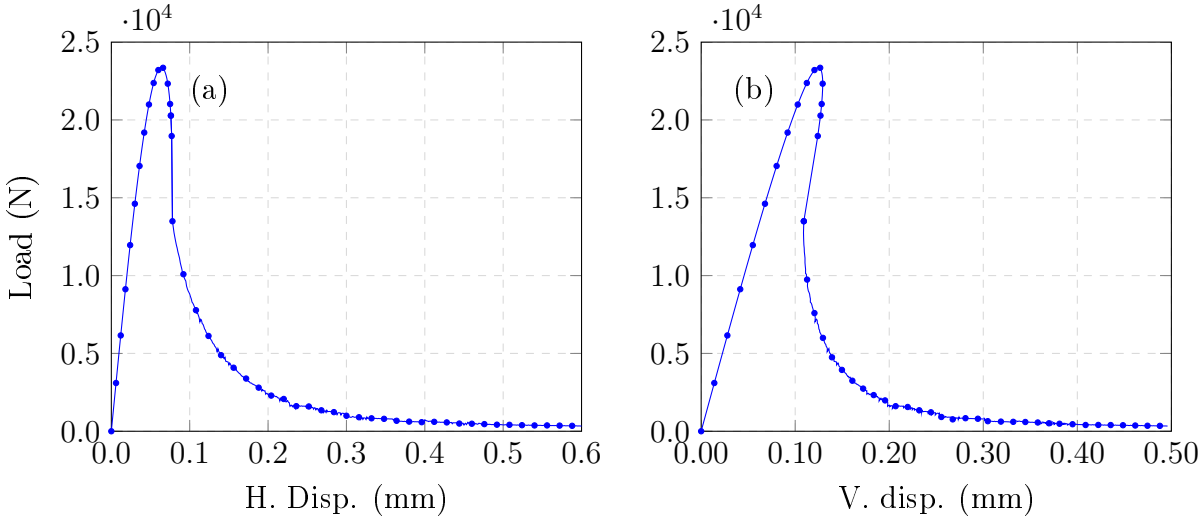

Figure 9.2: Load-displacement curve for three point bending test. (a) Horizontal displacement of the controlled node; (b) Vertical displacement of the load application point.

Observe that the output value is much less than the input one. This difference may have been caused by the functions $\alpha(\phi)$ and $g(\phi)$ which may not correctly represent the behaviour for this material. This issue can be highlighted by the snap-back behaviour observed in Fig. 9.2.b, that characterizes a very brittle material. As for the phase-field profile, it is observed that the result obtained is similar when pre-existing crack is not considered (See Section 8.1).

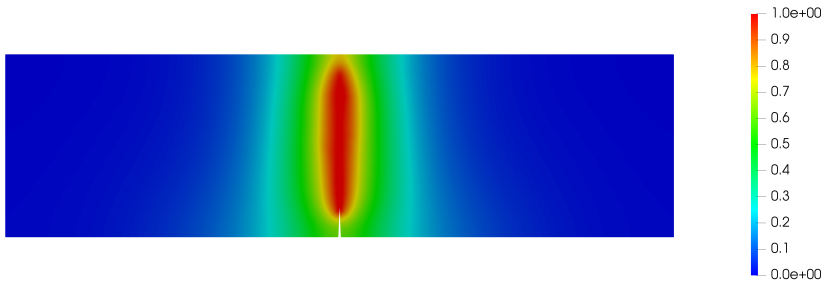

Figure 9.3: Phase-field profile for three point bending test.

9.2 Four point bending

In the four point bending test proposed by Khalilpour et al. (2019), a beam with 600 × 150 × 120 mm^3, with an initial crack of 45 mm, subject to a plane stress state was considered. The mesh is composed by triangular elements (T3) with size of 2 mm in the region of crack propagation and 20 mm faraway. The problem setting and the mesh are depicted in Fig. 9.4.

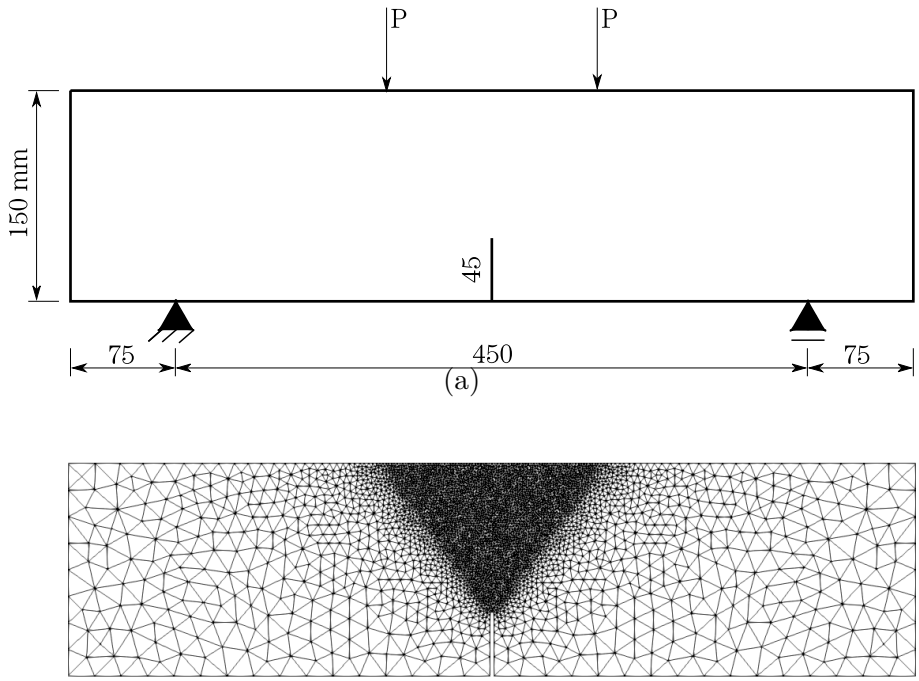

Figure 9.4: Four point bending test. Thickness of 120 mm. (a) Problem setting (Khalilpour et al., 2019), (b) T3 mesh.

The following material parameters were considered: $E_0 = 31400$ N/mm^2, $\nu = 0.2$, $G_c = 0.275$ N/mm and $l_0 = 47.5$ mm. The analysis has controlled the horizontal displacement of the right crack mouth node with increments of 1×10^{-3} mm and the convergence

was verified in displacement with global and local tolerance of 1×10^{-3}. The obtained load-displacement curves and the phase-field profile are presented in Figs. 9.5 and 9.6, respectively.

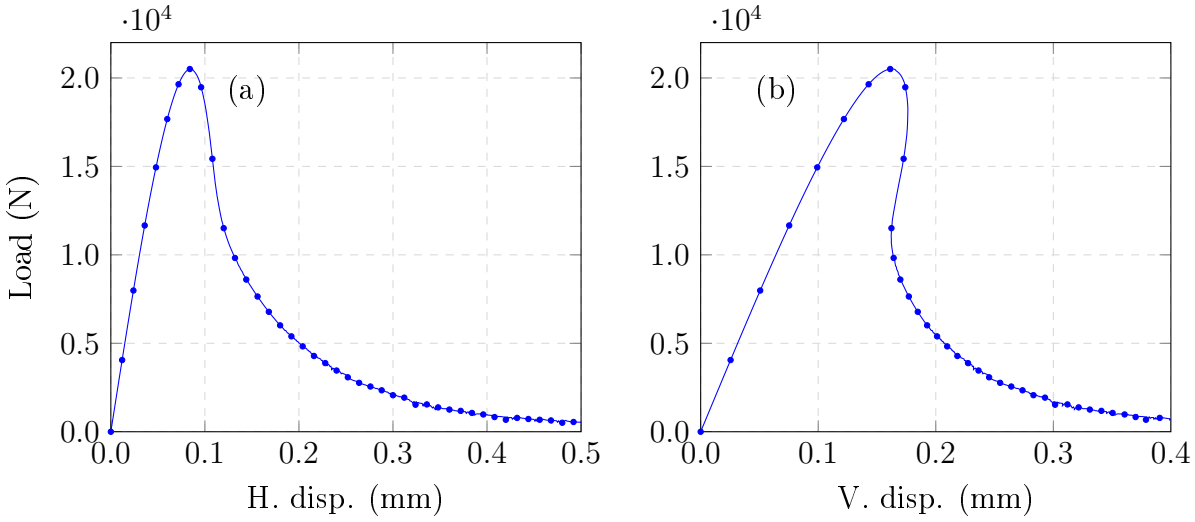

Figure 9.5: Load-displacement curve for four point bending test. (a) Horizontal displacement of the controlled node; (b) Vertical displacement of the load application load.

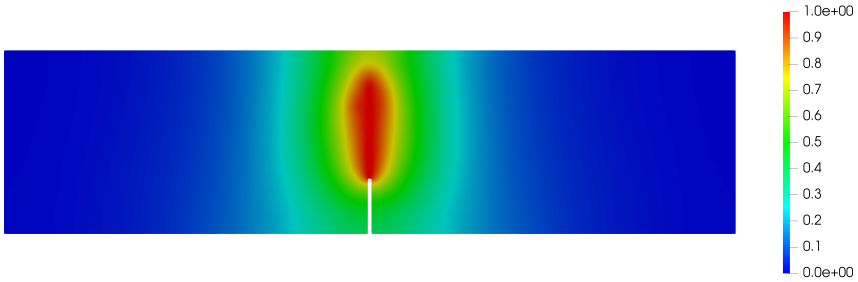

Figure 9.6: Phase-field profile for four point bending test.

Due to the snap back observed in Fig. 9.5.b, the fragile behaviour presented by the model used is also verified in the four point bending test and the obtained phase-field is similar to that observed when the initial crack is not considered (See Section 8.2).

9.3 Antisymmetric sample with two holes

In the antisymmetric sample adapted from Egger et al. (2019) a state of plane strain was considered. The bottom edge of specimen is fixed and the top edge is fixed in horizontal direction and subjected to a vertical displacement with increments of 1×10^{-4} mm (See Fig. 9.7).

The analysis was performed with $E_0 = 210000$ N/mm^2, $\nu = 0.3$, $G_c = 1$ N/mm, $l_0 = 2.0$ mm and considering the sample with, and without, a protected damage region

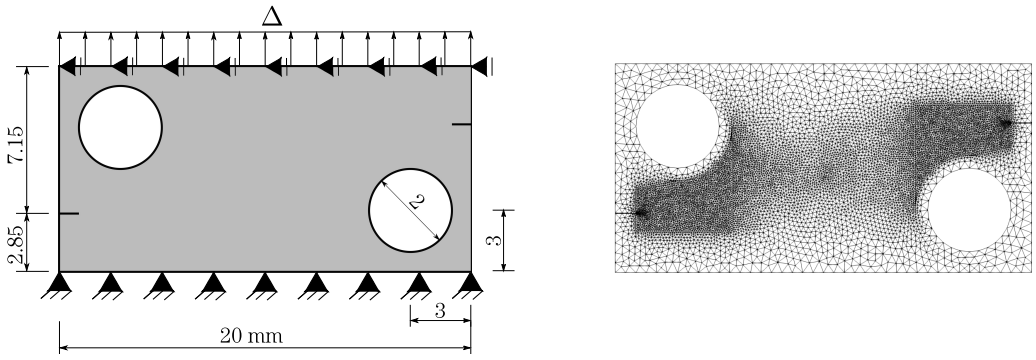

(a) (b)

Figure 9.7: Antisymmetric sample with two holes. (a) Problem setting (Egger et al., 2019), (b) T3 mesh. $h = 0.1$ mm in the refined region and $h = 0.5$ mm in the unrefined.

around the hole with dimension of 0.6 mm. The load-displacement curves and the phase-field profiles are presented in Figs. 9.8 and 9.9, respectively.

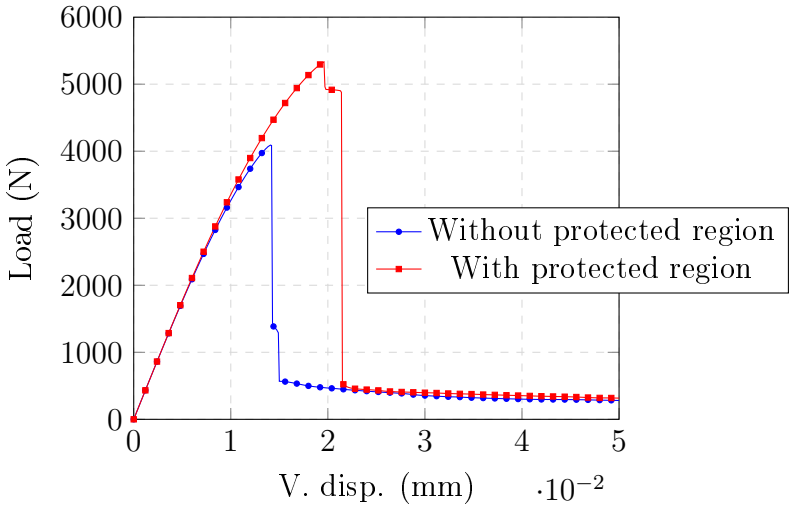

Figure 9.8: Load-displacement curve of top edge for antisymmetric sample with two holes.

The phase-field profile presented by the sample Fig. 9.9 is similar to that described by Egger et al. (2019) and Wu et al. (2020). When the damage around the hole is prevented by imposing a very high G_c value in the surrounding region, the initial crack propagates in the direction of the hole and later diverts its trajectory. Already when there is no protection around the hole the existing cracks don't propagate and new cracks are initiated at the hole perimeters and grow from there. The load-displacement curves show that the load drops down immediately when the crack starts to propagate.

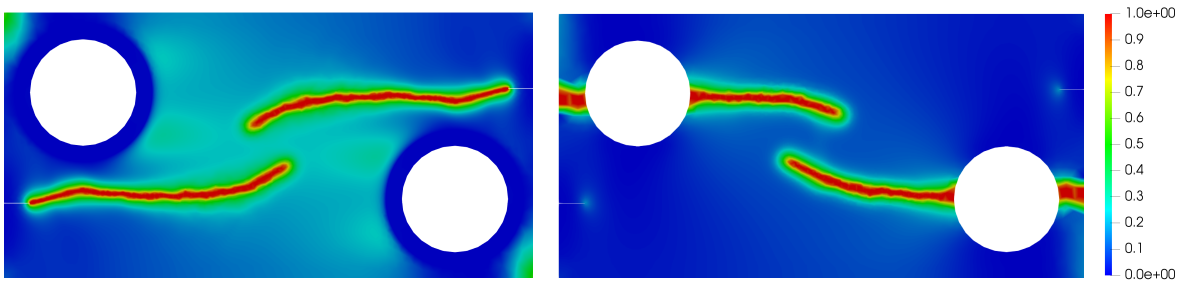

(a) (b)

Figure 9.9: Phase-field profile for $\Delta = 0.022$ mm. (a) With protection around the hole, (b) Without protection around the hole.

9.4 Asymmetrically notched beam

The asymmetrically notched beam of Miehe et al. (2010b) with $20 \times 8 \times 0.5$ mm^3 of size, under three point bending, plane stress state and an initial crack of 1 mm was considered in this test. The material parameters are: $E_0 = 20.8$ kN/mm^2, $\nu = 0.3$,

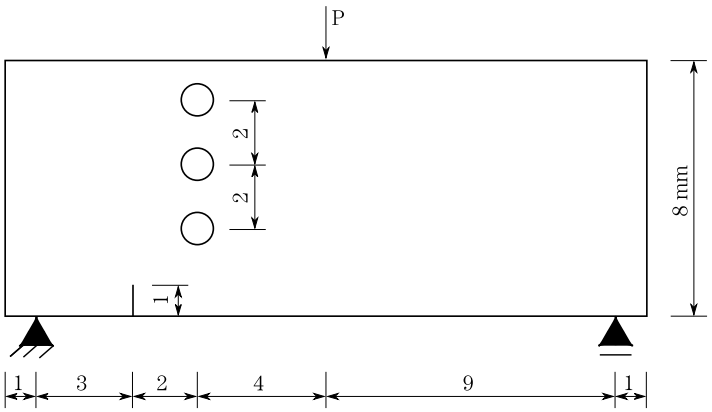

(a)

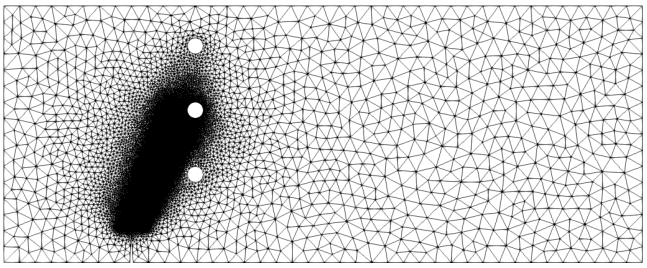

(b)

Figure 9.10: Asymmetric notched beam. The hole has 1 mm of radius and the beam has 0.5 mm of thickness. (a) Problem setting (Miehe et al., 2010b), (b) T3 mesh.

$G_c = 1.0 \times 10^{-3}$ kN/mm and $l_0 = 0.05$ mm.

The mesh is composed by triangular (T3) elements with mean nodal distance of

0.025 mm in the refined region, 0.5 mm around the top and bottom holes and 2 mm elsewhere. The problem setting and mesh are depicted in Fig. 9.10.

It was controlled the crack opening by incrementing the horizontal displacement of the right crack mouth node with 0.001 mm. The convergence was verified in displacements with global and local tolerance of 1×10^{-3}. The obtained results are depicted in Figs. 9.11 and 9.12.

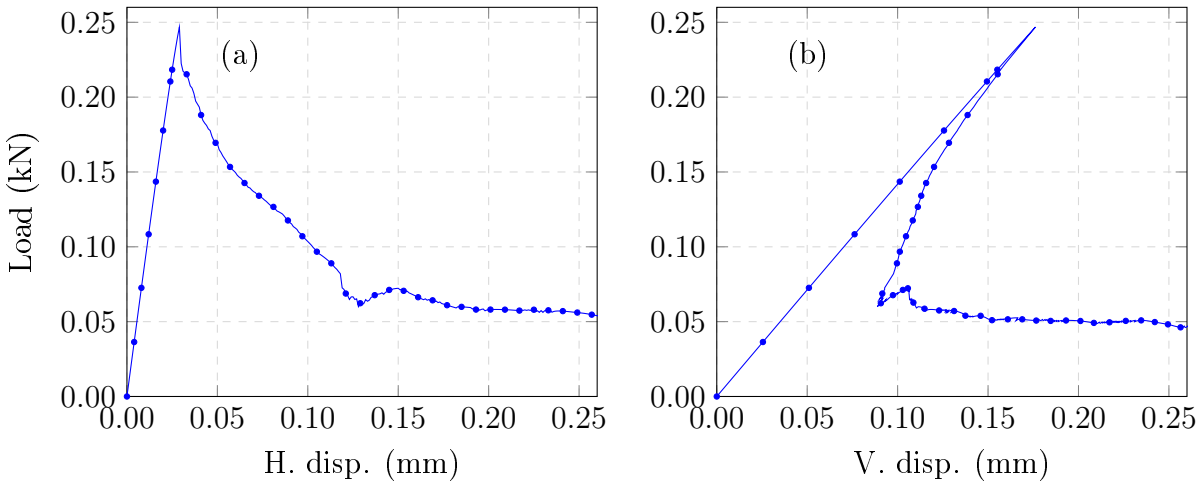

Figure 9.11: Load-displacement curve for the asymmetrically notched beam. (a) Horizontal displacement of the controlled node; (b) Vertical displacement of the load application node.

Figure 9.12: Phase-field profile for asymmetrically notched beam in 120th step.

The load-displacement curve shows that a very sharp snap back is observed and the crack grows in direction to the middle hole as already observed by Miehe et al. (2010b).

9.5 Mixed model failure test

The mixed model failure test, adapted from Wu et al. (2020), considers a beam with $675 \times 150 \times 50$ mm^3, subjected to a plane stress was considered. The tests were performed with, and without, the presence of the red support (See Fig. 9.13.a). The mesh has size of 1.25 mm in the refined region and 10 mm elsewhere (Fig. 9.13.b and 9.13.c). The material parameters are: $E_0 = 38000$ N/mm^2, $\nu = 0.2$, $G_c = 0.069$ N/mm and $l_0 = 2.5$ mm.

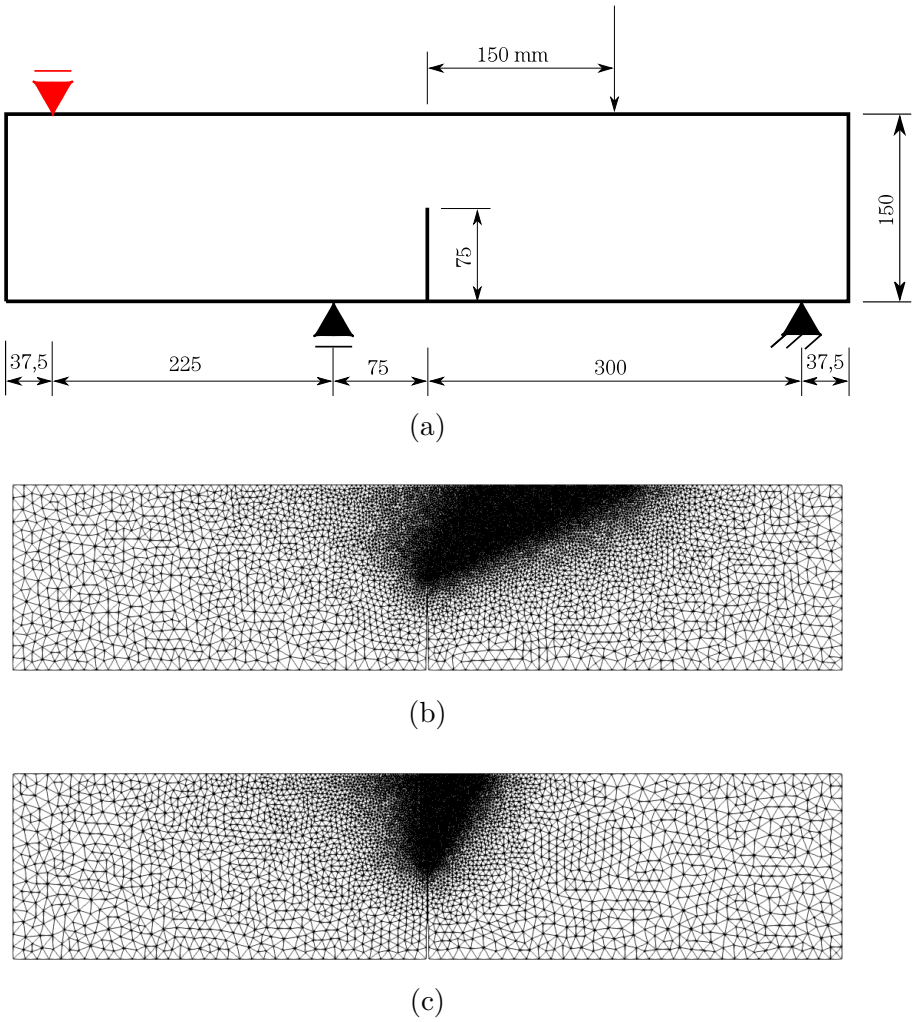

Figure 9.13: Mixed model failure test. Thickness of 50 mm. (a) Problem setting (Wu et al., 2020), (b) T3 mesh with the red support, (c) T3 mesh without the red support.

In the case of the test without the red support, an incremental horizontal displacement of 0.001 mm was imposed in the node to the left of the crack mouth towards opening the crack and, in the test with the red support, the vertical downward displacement of the node to the right of the crack mouth was controlled with same increments value. In both cases, the convergence was verified in displacements with 1×10^{-3} of global and local tolerance. Figs. 9.14 and 9.15 present the load-displacement curves and the phase-field profile.

The load-displacement curve shows that a more brittle behaviour is observed with the presence of the red support, and, as already shown by Wu et al. (2020), the additional support makes the crack propagate more inclined towards the load direction.

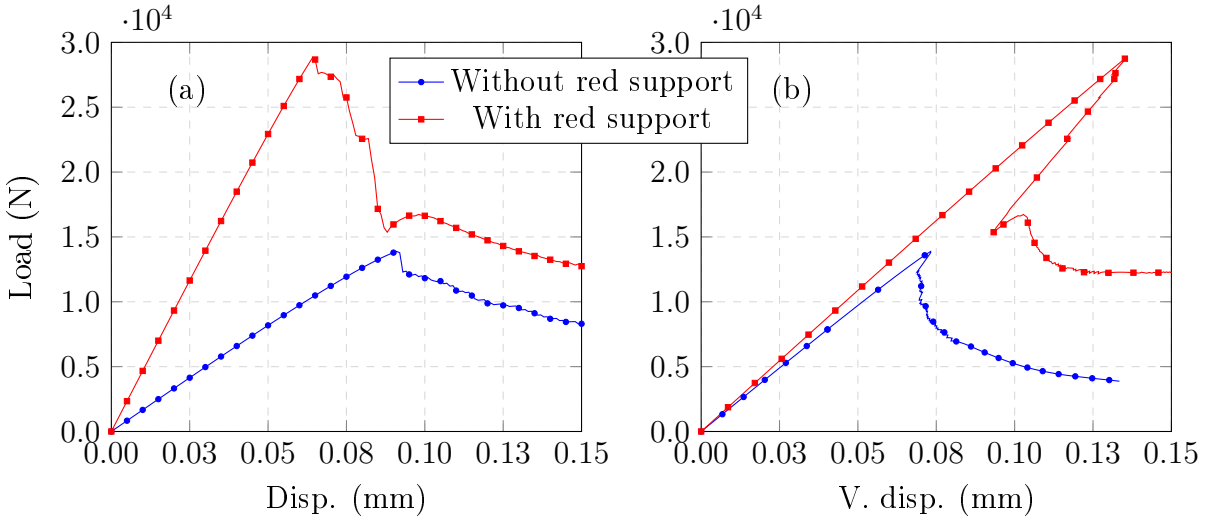

Figure 9.14: Load-displacement curve for mixed model failure test. (a) Displacement of the controlled degree of freedom; (b) Vertical displacement of the load application point.

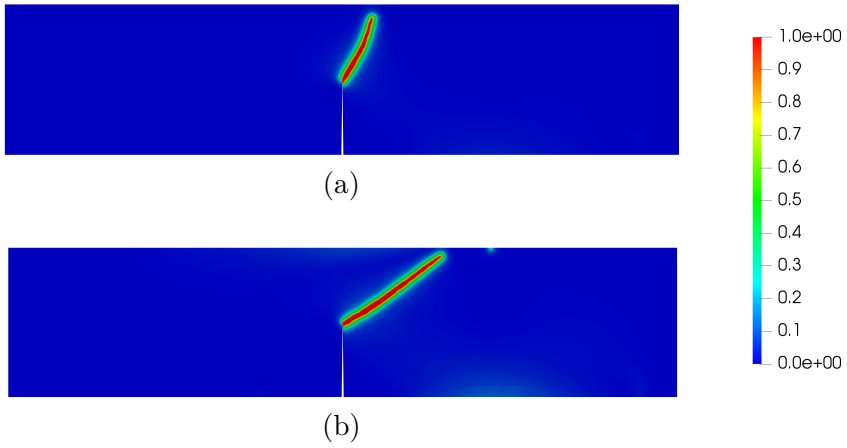

Figure 9.15: Phase-field profile for mixed model failure test. (a) Without red support (400th step), (b) With red support(250th step).

9.6 Semi circular bending test

The semicircle from Aliha et al. (2017) with 75 mm of radius, 32 mm of thickness and a initial crack of 20 mm was considered in this test. The sample was subjected to a plane stress state with the following materials parameters: $E_0 = 31400$ N/mm^2, $\nu = 0.2$, $G_c = 0.275$ N/mm and $l_0 = 2.0$ mm.

The failure modes I and II were tested by varying the position of the right support and initial crack, as depicted in problem setting (Fig. 9.16.a and 9.16.b). The meshes were composed by triangular (T3) elements with size of 0.5 mm in the refined region and 10 mm elsewhere (Fig. 9.16.c and 9.16.d).

In case of failure mode I (Fig. 9.16.a), the analysis has controlled the horizontal displacement of the node to the right of the crack mouth with increments of 1.5×10^{-3} mm

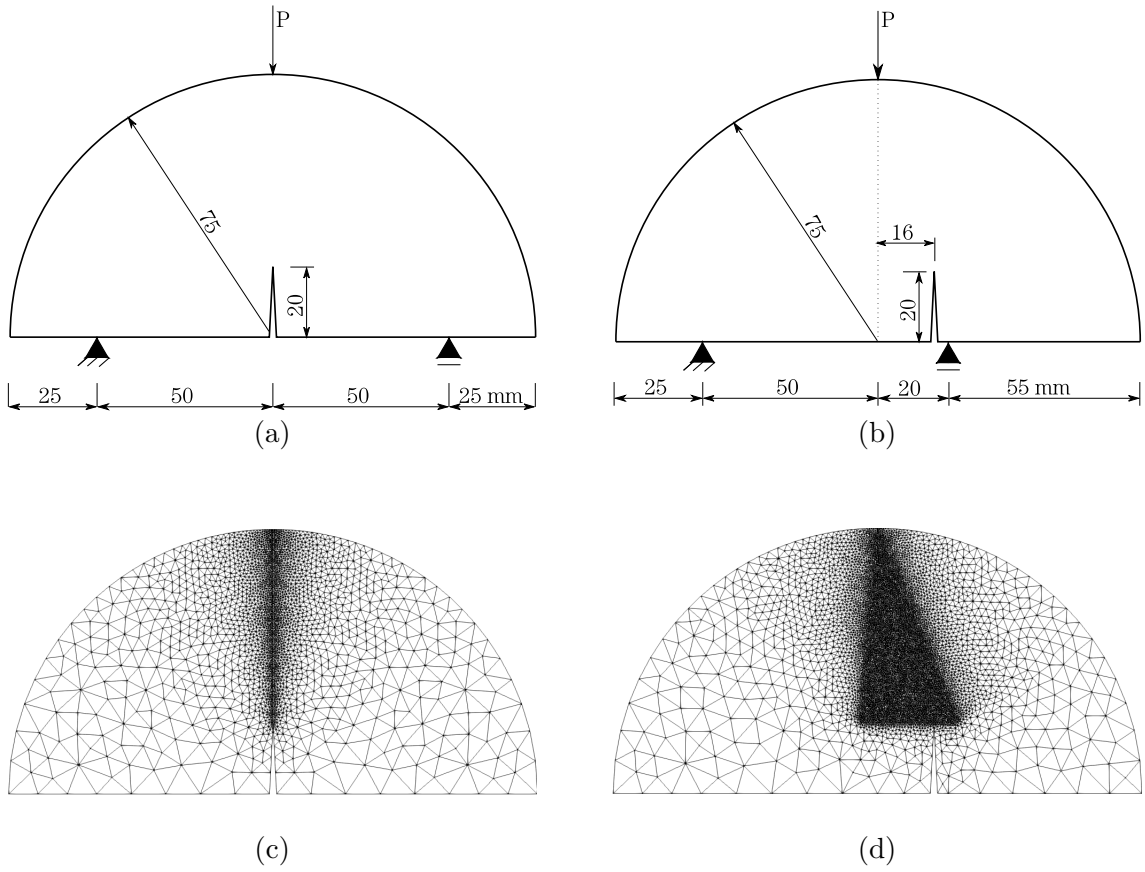

Figure 9.16: Semi circular bending test. The mesh has size of 0.5 mm in the refined region and 10 mm elsewhere. (a) Problem setting for mode I of failure (Aliha et al., 2017), (b) Problem setting for mode II of failure (Aliha et al., 2017), (c) T3 mesh for mode I of failure, (d) T3 mesh for mode II of failure.

and in case of failure mode II (Fig. 9.16.b) the vertical downward displacement of the node to the left of the crack mouth was controlled with increments of 1×10^{-3} mm. In both analyses the convergence was verified in displacements with local and global tolerance of 1×10^{-3}. The load-displacement plots and the obtained phase-field profile are in Figs. 9.17 and 9.18, respectively.

As experimentally shown by Aliha et al. (2017), in both cases the crack propagates towards the load direction and observing the load-displacements curves it is evident that the failure mode II happens in a more brittle way then the failure mode I.

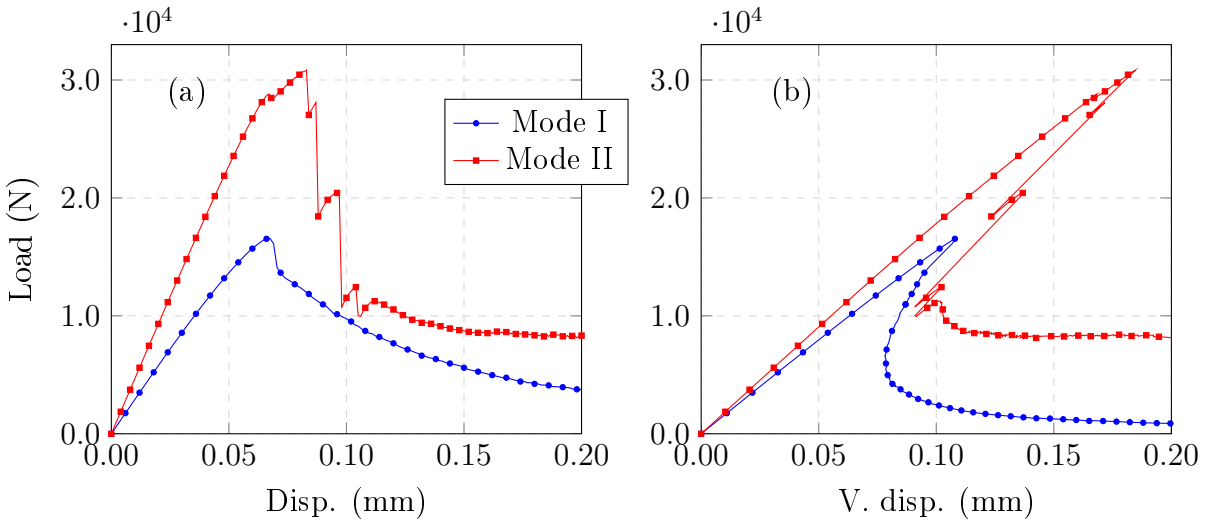

Figure 9.17: Load-displacement curve for the semi circular bending test. (a) Displacement of the controlled degree of freedom; (b) Vertical displacement of the load application point.

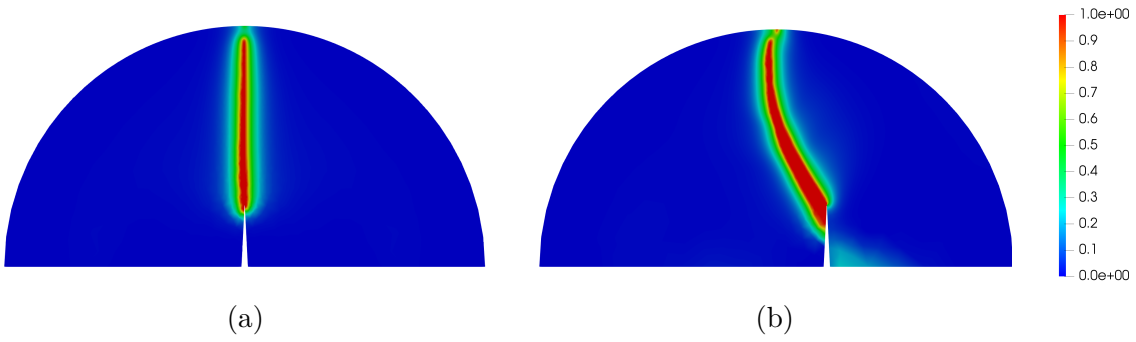

Figure 9.18: Phase-field profile for semi circular bending test in 400th step. (a) Mode I of failure, (b) Mode II of failure.

Chapter 10

Conclusions and future research topics

The main aim of this work was to study phase-field models of fracture, relying on the legacy of the research group regarding cracking modelling. Such a starting study aimed to understand the main characteristics, advantages and drawbacks of these models.

The theoretical background of the phase-field approach, based on variational formulation of Griffth's criterion, was studied producing an exhaustive demonstration of all equations and an increase on the research group expertness on this specific field. The task was accomplished through the implementation of four models based on the Finite Element Method: the isotropic constitutive model, which does not distinguish between compressed and stretched regions of the body, and the anisotropic models proposed by Lancioni and Royer-Carfagni (2009), Amor et al. (2009), Miehe et al. (2010b) that split the strain energy in an attempt to avoid cracks in compressed regions, making the models physically more realistic.

In order to solve the resultant nonlinear equations, a monolithic solver was initially used; however, it presented convergence issues, stopping the incremental-iterative process when the external loads starts to decrease. Aiming to overcome some of the issues of the monolithic solver, a staggered solver was implemented. This kind of solver uncouples the model and solves the displacement and the phase-field one at a time, resulting in a more robust process.

Regarding the computational implementation, it was very clear that *INSANE* is a very robust software with a great potential to include all kinds of models, due to its Object-Oriented Programming design. Also, the legacy of the *INSANE* source code was crucial to make easy all the implementation tasks required by this work, mainly the existent resources for constitutive modelling and for solution of the nonlinear equations.

The comparative study of the constitutive models implemented showed that the model proposed by Lancioni and Royer-Carfagni (2009) is very unstable and dependent on the mesh, presenting, among the tests illustrated in this manuscript, good results only for

the Panthéon fracture test. The study also showed that, although the model proposed by Amor et al. (2009) showed a great advance when compared to that proposed by Lancioni and Royer-Carfagni (2009), it was the model proposed by Miehe et al. (2010b) that exhibited the best results, in terms of stability and mesh dependency. So, this model was used in the remaining simulations.

The study on the behaviour of the phase-field strategy at the material and structural levels showed that, for a given energetic degradation function ($g(\phi) = (1-\phi)^2$) and geometric crack function ($\alpha(\phi) = \phi^2$), the material stress-strain curve is the same if the parameter $g_c = G_c/(2l_0)$ doesn't vary. Taking that into account, a stress-strain curve based on Carreira and Chu (1985, 1986) proposal, was adjusted in order to find a material with similar behaviour. Then, three phase-field models and one elastic degrading model, all of them presenting the same stress-strain curve were used in order to compare the structural behaviour. In all performed tests, the result was different even for materials whose stress-strain curve was the same, presenting a maximum load that varied according to the fracture parameter G_c. This controversial result seems to be due to the absence of any strength limit in the formulation of the used phase-field model. So, it seems to be mandatory the use of phase-field models that take into account some material strength limits, like the model proposed by Wu (2017). The use of such models, however, demands for appropriate solvers, like the bounded constrained solver (Farrell and Maurini, 2017, Benson and Munson, 2006, Heister et al., 2015).

The size effect on strength and brittleness for the Brazilian splitting test and for a tree point bending test was also evaluated. The results showed that the nominal strength decreases with increasing effective structural size and the structural brittleness increases with increasing effective size, a qualitative behaviour that has been observed in experimental tests (Bazant et al., 1991, Hasegawa and Okada, 1985, Santos, 2015, Bazant and Pfeiffer, 1987, Perdikaris and Romeo, 1995, Gettu et al., 1990). These good qualitative results seem to be due to the fact that the size effect phenomenon is mainly due to the ratio between the size of the region where the phase-field is active (the damaged zone) and the structure size.

The ability of phase-field to detect crack nucleation was also tested. In the four tests performed, the analysis was able to start the crack and continue its path, without any previous indication where the nucleation should have taken place.

The aforementioned statements point out the main characteristics, advantages and drawbacks of the phase-field modelling of fracture, as planned for this master's thesis. This first study of the research group in this field of investigation will give support for future research trends that could expand the achievements of this work. Some possible future research topics are exposed in the following:

- Implementation of other energetic degradation and geometric crack functions;
- Implementation of a bound-constrained solver, capable to deal with different ener-

getic degradation and geometric crack functions;

- Comparative study on structural behaviour using phase-field and equivalent elastic degrading models;
- Systematic study on phase-field models mesh dependence;
- Use of other numerical methods instead FEM, like Generalized Finite Element Method, Boundary Element Method and Meshfree Methods;
- Adoption of adaptive refinement in order to change the mesh and to add the phase-field degrees of freedoms only in the regions where phase-field has been activated;
- Implement the phase-field modelling for the 3D case.

Bibliography

Alessi, R., Marigo, J.-J. and Vidoli, S. (2015), 'Gradient damage models coupled with plasticity: Variational formulation and main properties', *Mechanics of Materials* vol. 80, 351 – 367.

Aliha, M., Razmi, A. and Mansourian, A. (2017), 'The influence of natural and synthetic fibers on low temperature mixed mode i+ii fracture behavior of warm mix asphalt (wma) materials', *Engineering Fracture Mechanics* vol. 182, 322 – 336.
URL: *http://www.sciencedirect.com/science/article/pii/S0013794417303843*

Amor, H., Marigo, J.-J. and Maurini, C. (2009), 'Regularized formulation of the variational brittle fracture with unilateral contact: Numerical experiments', *Journal of the Mechanics and Physics of Solids* vol. 57(8), 1209–1229.

Bahaaddini, M., Serati, M., Masoumi, H. and Rahimi, E. (2019), 'Numerical assessment of rupture mechanisms in brazilian test of brittle materials', *International Journal of Solids and Structures* vol. 180-181, 1 – 12.
URL: *http://www.sciencedirect.com/science/article/pii/S0020768319303154*

Bazant, Z. P., Kazemi, M. T., Hasegawa, T. and Mazars, J. (1991), 'Size effects in brazilian split-cylinder tests: measurements and fracture analysis', *Journal ACI Mater* vol. 88, 325–332.

Bazant, Z. and Pfeiffer, P. (1987), 'Determination of fracture energy from size effect and brittleness number', *ACI Materials Journal* vol. 84, 463–480.

Benson, S. J. and Munson, T. S. (2006), 'Flexible complementarity solvers for large-scale applications', *Optimization Methods and Software* vol. 21(1), 155–168.

Borst, de, R., Sluys, L., Mühlhaus, H.-B. and Pamin, J. (1993), 'Fundamental issues in finite element analyses of localization of deformation', *Engineering Computations* vol. 10(2), 99–121.

Borst, R. and Gutiérrez, M. A. (1999), 'A unified framework for concrete damage and fracture models including size effects', *International Journal of Fracture* vol. 95, 261–277.

Bourdin, B., Francfort, G. and Marigo, J. J. (2000), 'Numerical experiments in revisited brittle fracture', *Journal of the Mechanics and Physics of Solids* vol. 48, 797–826.

Bourdin, B., Francfort, G. and Marigo, J.-J. (2008), 'The variational approach to fracture', *Reprinted from J. Elasticity* vol. 91, 5–148.

Broek, D. (1984), *Elementary Engineering Fracture Mechanics*, Martinus Nijhoff Publishers, P.O. Box 566, 2501 CN The Hague, The Netherlands.

Campos, B. C., Barros, F. B. and Penna, S. S. (2020), 'On the numerical integration in generalized/extended finite element method analysis for crack propagation problems', *Engineering Computations* vol. 38(1), 180–220.

Carreira, D. J. and Chu, K.-H. (1985), 'Stress-strain relationship for plain concrete in compression', *American Concrete Institute Journal* vol. 82 (6), 797–804.

Carreira, D. J. and Chu, K.-H. (1986), 'Stress-strain relationship for plain concrete in tension', *American Concrete Institute Journal* vol. 83 (1), 21–28.

da Silva, L. L., Pitangueira, R. L., Penna, S. S. and Barros, F. B. (2017), Um modelo numérico para simulação do processo de fissuração em meios parcialmente frágeis.

de Borst, R. (2002), 'Fracture in quasi-brittle materials: a review of continuum damage-based approaches', *Engineering Fracture Mechanics* vol. 69(2), 95–112.
URL: *https://www.sciencedirect.com/science/article/pii/S0013794401000820*

Egger, A., Pillai, U., Agathos, K., Kakouris, E., Chatzi, E., Ashcroft, I. and Triantafyllou, S. (2019), 'Discrete and phase field methods for linear elastic fracture mechanics: A comparative study and state-of-the-art review', *Applied Sciences* vol. 9, 2436.

Farrell, P. and Maurini, C. (2017), 'Linear and nonlinear solvers for variational phase-field models of brittle fracture', *International Journal for Numerical Methods in Engineering* vol. 109(5), 648–667.
URL: *https://onlinelibrary.wiley.com/doi/abs/10.1002/nme.5300*

Fonseca, G. M., Barros, F. B., de Oliveira, T. S., Monteiro, H. A., Novelli, L. and Pitangueira, R. L. (2020), '2-d crack propagation analysis using stable generalized finite element method with global-local enrichments', *Engineering Analysis with Boundary Elements* vol. 118, 70–83.

Fuina, J. S. (2009), Formulações de Modelos Constitutivos de Microplanos para Contínuos Generalizados, Phd thesis, Universidade Federal de Minas Gerais (UFMG). (in portuguese).

Gettu, R. Z., Bazant, Z. P. and Karr, M. E. (1990), 'Fracture properties and brittleness of high-strength concrete', *ACI Materials Journal* vol. 87, 608–618.

Gori, L. (2018), Failure analysis of quasi-brittle media using the micropolar continuum theory, elastic-degrading constitutive models, and smoothed point interpolation methods, Phd thesis, Universidade Federal de Minas Gerais (UFMG).

Gori, L., Penna, S. S. and da Silva Pitangueira, R. L. (2017), 'An enhanced tensorial formulation for elastic degradation in micropolar continua', *Applied Mathematical Modelling* vol. 41, 299–315.

Gori, L., Silva Penna, S. and da Silva Pitangueira, R. L. (2019*a*), 'G-space theory and weakened-weak form for micropolar media: Application to smoothed point interpolation methods', *Engineering Analysis with Boundary Elements* vol. 101, 318–329.
URL: *https://www.sciencedirect.com/science/article/pii/S0955799718305794*

Gori, L., Silva Penna, S. and da Silva Pitangueira, R. L. (2019*b*), 'Smoothed point interpolation methods for the regularization of material instabilities in scalar damage models', *International Journal for Numerical Methods in Engineering* vol. 117(7), 729–755.
URL: *https://onlinelibrary.wiley.com/doi/abs/10.1002/nme.5974*

Hasegawa, T. and Okada, T. (1985), 'Size effect on splitting tensile strength of concrete', *Institute 7th Conference* pp. 309–312.

Heister, T., Wheeler, M. F. and Wick, T. (2015), 'A primal-dual active set method and predictor-corrector mesh adaptivity for computing fracture propagation using a phase-field approach', *Computer Methods in Applied Mechanics and Engineering* vol. 290, 466–495.

Karma, A., Kessler, D. A. and Levine, H. (2001), 'Numerical experiments in revisited brittle fracture', *Physics Review Letter* vol. 87:045501.

Khalilpour, S., BaniAsad, E. and Dehestani, M. (2019), 'A review on concrete fracture energy and effective parameters', *Cement and Concrete Research* vol. 120, 294 – 321.
URL: *http://www.sciencedirect.com/science/article/pii/S0008884618310688*

Kuhn, C., Schuter, A. and Müller, R. (2015), 'On degradation functions in phase field fracture models', *Computational Materials Science* vol. 108, 374–384.

Lancioni, G. and Royer-Carfagni, G. (2009), 'The variational approach to fracture mechanics', *Journal of Elasticity* vol. 95, 1–30.

Lemaitre, J. and Chaboche, J. L. (1990), *Mechanic of Solid Materials*, Cambridge University Press, Cambridge.

Malekan, M., Silva, L. L., Barros, F. B., Pitangueira, R. L. and Penna, S. S. (2018), 'Two-dimensional fracture modeling with the generalized/extended finite element method: An object-oriented programming approach', *Advances in Engineering Software* vol. 115, 168–193.

Mazars, J. (1984), Application de la m´ecanique de l'endommagement au comportement non lineaire et 'a la rupture du b´eton de structure., Phd thesis, Université Paris, Paris. (in portuguese).

Mendonça, T. S., Peixoto, R. G. and Ribeiro, G. O. (2020), 'A new class of cells with embedded discontinuity for fracture analysis by the boundary element method', *International Journal for Numerical Methods in Engineering* vol. 121(17), 3869–3892.
URL: *https://onlinelibrary.wiley.com/doi/abs/10.1002/nme.6387*

Miehe, C., Hofacker, M. and Welschinger, F. (2010b), 'A phase field model for rate-independent crack propagation: Robust algorithmic implementation based on operator splits', *Computer Methods in Applied Mechanics and Engineering* vol. 199, 2765–2778.

Miehe, C., Welschinger, F. and Hofacker, M. (2010a), 'Thermodynamically consistent phase-field models of fracture: Variational principles and multi-field FE implementations', *International Journal for Numerical Methods in Engineering* vol. 83, 1273–1311.

Monteiro, A. B. (2013), Ambiente Teórico-Computacional Unificado para Modelos Constitutivos: Inclusão de Modelo Elastoplástico com Dano, Master dissetation, Universidade Federal de Minas Gerais (UFMG). (in portuguese).

Monteiro, H. A. d. S. (2021), Uma Nova Abordagem para Análise Estática em Duas Escalas: MEF Generalizados/Estendidos, Estratégia Global-Local e Modelos de Degradação Elástica no Estudo de Meios Não Lineares, Parcialmente Frágeis e Heterogêneos, Phd thesis, Universidade Federal de Minas Gerais (UFMG). (in portuguese).

Monteiro, H., Novelli, L., Fonseca, G., Pitangueira, R. and Barros, F. (2020), 'A new approach for physically nonlinear analysis of continuum damage mechanics problems using the generalized/extended finite element method with global-local enrichment', *Engineering Analysis with Boundary Elements* vol. 113, 277–295.
URL: *https://www.sciencedirect.com/science/article/pii/S0955799719306769*

Nogueira, P. D. (2021), Damage Models for Micromorphic Continuum, Master dissetation, Universidade Federal de Minas Gerais (UFMG).

Novelli, L., de Oliveira, T. S., da Silveira Monteiro, H. A., Fonseca, G. M., da Silva Pitangueira, R. L. and Barros, F. B. (2020), 'Stable generalized/extended finite element

method with global–local enrichment for material nonlinear analysis', *Computer Methods in Applied Mechanics and Engineering* vol. 372, 113429.
URL: *https://www.sciencedirect.com/science/article/pii/S0045782520306149*

Oliveira, D. B., Penna, S. S. and Pitangueira, R. L. S. (2020), 'Elastoplastic constitutive modeling for concrete: a theoretical and computational approach', *Revista IBRACON de Estruturas e Materiais* vol. 13, 171 – 182.

Peerlings, R., de Borst, R., Brekelmans, W. and Geers, M. (2002), 'Localisation issues in local and nonlocal continuum approaches to fracture', *European Journal of Mechanics - A/Solids* vol. 21(2), 175–189.

Peixoto, R., Penna, S., Pitangueira, R. and Ribeiro, G. (2019), 'A non-local damage approach for the boundary element method', *Applied Mathematical Modelling* vol. 69, 63–76.
URL: *https://www.sciencedirect.com/science/article/pii/S0307904X18305973*

Peixoto, R., Ribeiro, G. and Pitangueira, R. (2018), 'A boundary element method formulation for quasi-brittle material fracture analysis using the continuum strong discontinuity approach', *Engineering Fracture Mechanics* vol. 202, 47–74.
URL: *https://www.sciencedirect.com/science/article/pii/S0013794418304521*

Penna, S. S. (2011), Formulação multipotencial para modelos de degradação elástica: unificação teórica, proposta de novo modelo, implementação computacional e modelagem de estruturas de concreto, Phd thesis, Universidade Federal de Minas Gerais (UFMG). (in portuguese).

Perdikaris, P. and Romeo, A. (1995), 'Size effect on fracture energy of concrete and stability issues in three-point bending fracture toughness testing', *ACI Materials Journal* vol. 92, 483–496.

Pham, K., Amor, H., Marigo, J.-J. and Maurini, C. (2011), 'Gradient damage models and their use to approximate brittle fracture', *International Journal of Damage Mechanics* vol. 20, 618–652.

Planas, J., Guinea, G. and Elices, M. (1999), 'Size effect and inverse analysis in concrete fracture', *International Journal of Fracture* vol. 95, 367–378.

RILEM (1985), 'Determination of the fracture energy of mortar and concrete by means of three-point bend tests on notched beams', *Materials and Structures* vol. 18, 287–290.

Saliba, S. S., Gori, L. and da Silva Pitangueira, R. L. (2021), 'A coupled finite element-meshfree smoothed point interpolation method for nonlinear analysis', *Engineering*

Analysis with Boundary Elements vol. 128, 1–18.
URL: *https://www.sciencedirect.com/science/article/pii/S0955799721000667*

Santos, A. H. d. A. e. (2015), Estudo experimental do efeito de escala em estruturas de concreto utilizando correlação de imagem digital, Phd thesis, Universidade Federal de Minas Gerais (UFMG). (in portuguese).

Silva, L. L. d. (2019), Estratégia Multiescala para descrição Micromórfica do Contínuo a partir do Contínuo Clássico., Phd thesis, Universidade Federal de Minas Gerais (UFMG). (in portuguese).

Simão, W. I. d. S. (2003), Modelos de armadura e aderência para análise não-linear de estruturas de concreto armado, Master dissetation, Universidade Federal de Minas Gerais (UFMG). (in portuguese).

Simo, J. and Ju, J. (1987), 'Strain- and stress-based continuum damage models—i. formulation', *International Journal of Solids and Structures* vol. 23(7), 821–840.

Winkler, B., Hofstetter, G. and Lehar, H. (2004), 'Application of a constitutive model for concrete to the analysis of a precast segmental tunnel lining', *International Journal for Numerical and Analytical Methods in Geomechanics* vol. 28, 797 – 819.

Wolenski, A. R. V., Monteiro, A. B., Penna, S. S., Pitangueira, R. L. d. S. and Barros, F. B. (2020), 'Damage propagation using novel g/xfem strategies: computational aspects and numerical investigations', *Journal of the Brazilian Society of Mechanical Sciences and Engineering* vol. 42.
URL: *https://www.insane.dees.ufmg.br/wp-content/uploads/2020/12/8230-Larissa.pdf*

Wolff, K. P., Pitangueira, R. L. and Peixoto, R. G. (2020), 'A displacement-based and explicit non-planar 3d crack propagation model in the generalized/extended finite element method', *Theoretical and Applied Fracture Mechanics* vol. 108, 102647.

Wu, J.-Y. (2017), 'A unified phase-field theory for the mechanics of damage and quasi-brittle failure', *Journal of the Mechanics and Physics of Solids* vol. 103, 72–99.

Wu, J.-Y., Nguyen, V. P., Thanh Nguyen, C., Sutula, D., Bordas, S. and Sinaie, S. (2020), 'Chapter One - Phase-field modeling of fracture', *Advances in Applied Mechanics* vol. 53, 1–183.
URL: *https://www.sciencedirect.com/science/article/pii/S0065215619300134*

Zang, P., Hu, X., Wang, X. and Yao, W. (2018), 'An iteration scheme for phase field model for cohesive fracture and its implementation in abaqus', *Engineering Fracture Mechanics* vol. 204, 2668–287.

Zhou, S., Zhuang, X., Zhu, H. and Rabczuk, T. (2018), 'Phase field modelling of crack propagation, branching and coalescence in rocks', *Theoretical and Applied Fracture Mechanics* vol. 96, 174 – 192.
URL: *http://www.sciencedirect.com/science/article/pii/S016784421830123X*

Appendices

Appendix A

Demonstration of theoretical foundation equations

Equations used in theoretical foundation of phase-field will be demonstrated in this chapter using index notation, for facility.

A.1 Eq. (2.6)

The energy functional that gives the energy balance is given by:

$$E_t = \int_\Omega \psi_0(\varepsilon_{ij}) \, \mathrm{d}\mathcal{V} - \int_\Omega b_i u_i \, \mathrm{d}\mathcal{V} - \int_{\partial\Omega_t} t_i u_i \, \mathrm{d}\mathcal{A} \tag{A.1}$$

Deriving in relation to time it gets:

$$\dot{E}_t = \int_\Omega \frac{\partial \psi_0}{\partial \varepsilon_{ij}} \dot{\varepsilon_{ij}} \, \mathrm{d}\mathcal{V} - \int_\Omega (\dot{b}_i u_i + b_i \dot{u}_i) \, \mathrm{d}\mathcal{V} - \int_{\partial\Omega_t} (\dot{t}_i u_i + t_i \dot{u}_i) \, \mathrm{d}\mathcal{A} \tag{A.2}$$

The first integral in Eq. (A.2) can be rewritten as:

$$\int_\Omega \frac{\partial \psi_0}{\partial \varepsilon_{ij}} \dot{\varepsilon_{ij}} \, \mathrm{d}\mathcal{V} = \int_\Omega \sigma_{ij} \dot{\varepsilon_{ij}} \, \mathrm{d}\mathcal{V} = \int_\Omega \sigma_{ij} \left(\frac{\dot{u}_{i,j} + \dot{u}_{j,i}}{2} \right) \, \mathrm{d}\mathcal{V}$$

$$\int_\Omega \sigma_{ij} \dot{\varepsilon_{ij}} \, \mathrm{d}\mathcal{V} = \frac{1}{2} \int_\Omega \sigma_{ij} \dot{u}_{i,j} \, \mathrm{d}\mathcal{V} + \frac{1}{2} \int_\Omega \sigma_{ij} \dot{u}_{j,i} \, \mathrm{d}\mathcal{V} \tag{A.3}$$

Interchanging the dummy index on the last term of Eq. (A.3), it gets:

$$\int_\Omega \sigma_{ij} \dot{\varepsilon_{ij}} \, \mathrm{d}\mathcal{V} = \frac{1}{2} \int_\Omega \sigma_{ij} \dot{u}_{i,j} dV + \frac{1}{2} \int_\Omega \sigma_{ji} \dot{u}_{i,j} dV$$

But σ_{ij} is symmetric, so $\sigma_{ij} = \sigma_{ji}$, and the equation becomes:

$$\int_\Omega \sigma_{ij} \dot{\varepsilon_{ij}} \, \mathrm{d}\mathcal{V} = \int_\Omega \sigma_{ij} \dot{u}_{i,j} dV \tag{A.4}$$

For applying the divergence theorem to simplify Eq. (A.4), consider:

$$\left(\sigma_{ij}\dot{u}_i\right)_{,j} = \sigma_{ij,j}\dot{u}_i + \sigma_{ij}\dot{u}_{i,j}$$

$$\sigma_{ij}\dot{u}_{i,j} = \left(\sigma_{ij}\dot{u}_i\right)_{,j} - \sigma_{ij,j}\dot{u}_i \tag{A.5}$$

Substituting Eq. (A.5) in Eq. (A.4), and applying the divergence theorem it gets:

$$\int_\Omega \sigma_{ij}\dot{\varepsilon_{ij}}\ \mathrm{d}\mathcal{V} = \int_{\partial\Omega} \sigma_{ij}\dot{u}_i n_j\ \mathrm{d}\mathcal{A} - \int_\Omega \sigma_{ij,j}\dot{u}_i\ \mathrm{d}\mathcal{V} \tag{A.6}$$

Now, substituting Eq. (A.6) in Eq. (A.2), after some algebraic manipulations, it obtains:

$$\dot{E}_t = \int_{\partial\Omega_t} (\sigma_{ij}n_j - t_i)\dot{u}_i\ \mathrm{d}\mathcal{A} + \int_{\partial\Omega_u} \sigma_{ij}n_j\dot{u}_i\ \mathrm{d}\mathcal{A} - \int_\Omega (\sigma_{ij,j} + b_i)\dot{u}_i\ \mathrm{d}\mathcal{V} - \int_\Omega \dot{b}_i u_i\ \mathrm{d}\mathcal{V} - \int_{\partial\Omega_t} \dot{t}_i u_i\ \mathrm{d}\mathcal{A} \tag{A.7}$$

But $\sigma_{ij}n_j - t_i = 0$ and $\sigma_{ij,j} + b_i = 0$, so the Eq. (A.7) becomes:

$$\dot{E}_t = \int_{\partial\Omega_u} \sigma_{ij}n_j\dot{u}_i\ \mathrm{d}\mathcal{A} - \int_\Omega \dot{b}_i u_i\ \mathrm{d}\mathcal{V} - \int_{\partial\Omega_t} \dot{t}_i u_i\ \mathrm{d}\mathcal{A} \tag{A.8}$$

In a symbolic form:

$$\dot{E}_t = \int_{\partial\Omega_u} (\underline{\sigma}\cdot\bar{n})\cdot\dot{\bar{u}}\ \mathrm{d}\mathcal{A} - \int_\Omega \dot{\bar{b}}\cdot\bar{u}\ \mathrm{d}\mathcal{V} - \int_{\partial\Omega_t} \dot{\bar{t}}\cdot\bar{u}\ \mathrm{d}\mathcal{A} \tag{A.9}$$

A.2 Eq. (2.7)

The first variation of energy functional E_t, given by Eq. (2.7) can be written as:

$$\delta E_t = \delta\Psi_s + \delta\Psi_c - \delta P_{ext} \tag{A.10}$$

By unilateral stationary condition, it can say that Eq. (A.10) is bigger than zero. In this time, it's going to be demonstrated each part of this equation.

Before perturbation, the strain energy can be expressed as follows:

$$\Psi_{s\epsilon} = \int_{\Omega\setminus\Gamma} \psi(\varepsilon_{ij}(u_{\epsilon_{ij}}), \Gamma_\epsilon)\ \mathrm{d}\mathcal{V} \tag{A.11}$$

In this way, it gets:

$$\delta\Psi_s = \left.\frac{\partial\Psi_{s\epsilon}}{\partial\epsilon}\right|_{\epsilon=0} = \int_{\Omega\setminus\Gamma} \left.\left(\frac{\partial\psi}{\partial\underline{\varepsilon}_\epsilon}\frac{\partial\underline{\varepsilon}_\epsilon}{\partial\epsilon}\right)\right|_{\epsilon=0} dV + \left.\left(\frac{\partial\Psi_{s\epsilon}}{\partial\Gamma_\epsilon}\frac{\partial\Gamma_\epsilon}{\partial\epsilon}\right)\right|_{\epsilon=0}$$

$$\delta\Psi_s = \int_{\Omega\setminus\Gamma} \sigma_{ij}\delta\varepsilon_{ij}\ \mathrm{d}\mathcal{V} + \frac{\partial\Psi_s}{\partial\Gamma}\delta\Gamma \tag{A.12}$$

Using the divergence theorem, in analogy to what was done in Appendix A.1, Eq. (A.12) can be written as:

$$\delta\Psi_s = \int_{\partial\Omega_t} (\sigma_{ij} n_j)\delta u_i \ \mathrm{d}\mathcal{A} + \int_{\Gamma} (\sigma_{ij} n_j)\delta u_i \ \mathrm{d}\mathcal{A} - \int_{\Omega\setminus\Gamma} (\sigma_{ij,j} u_i \ \mathrm{d}\mathcal{V} + \frac{\partial \Psi_s}{\partial \Gamma}\delta\Gamma \tag{A.13}$$

The surface energy, used in crack growth, is expressed:

$$\delta\Psi_c = \left.\frac{\partial \Psi_{c\epsilon}}{\partial \epsilon}\right|_{\epsilon=0} = \frac{\partial}{\partial \epsilon}\left(\int_{\Gamma} G_c d\Gamma + \epsilon G_c \delta\Gamma\right)$$

$$\delta\Psi_c = \left.\frac{\partial \Psi_{c\epsilon}}{\partial \epsilon}\right|_{\epsilon=0} = \frac{\partial}{\partial \epsilon}\left(\int_{\Gamma} G_c d\Gamma + \epsilon G_c \delta\Gamma\right)$$

$$\delta\Psi_c = G_c \delta\Gamma \tag{A.14}$$

For work of the external loads, it's already know, by FEM:

$$\delta P_{ext} = \int_{\Omega\setminus\Gamma} b_i \delta u_i \ \mathrm{d}\mathcal{V} + \int_{\partial\Omega_t} t_i \delta u_i \ \mathrm{d}\mathcal{A} \tag{A.15}$$

Substituting Eq. (A.13), Eq. (A.14) and Eq. (A.15) in Eq. (A.10), it arrives at Eq. (A.16), as it wanted to demonstrated.

$$\delta E_t = \int_{\Gamma} \sigma_{ij} n_j \delta u_i \ \mathrm{d}\mathcal{A} + \int_{\partial\Omega_t} (\sigma_{ij} n_j - t_i)\delta u_i \ \mathrm{d}\mathcal{A} - \int_{\Omega\setminus\Gamma} (\sigma_{ij,j} + b_i)\delta u_i \ \mathrm{d}\mathcal{V} + \left(\frac{\partial \Psi_s}{\partial \Gamma} + G_c\right)\delta\Gamma \tag{A.16}$$

In symbolic form:

$$\delta E_t = \int_{\Gamma} (\underline{\sigma}\cdot\bar{n})\delta\underline{u} \ \mathrm{d}\mathcal{A} + \int_{\partial\Omega_t} (\underline{\sigma}\cdot\bar{n} - \bar{t})\cdot\delta\bar{u} \ \mathrm{d}\mathcal{A} - \int_{\Omega\setminus\Gamma} (\nabla\underline{\sigma} + \underline{b})\cdot\delta\underline{u} \ \mathrm{d}\mathcal{V} + \left(\frac{\partial \Psi_s}{\partial \Gamma} + G_c\right)\delta\Gamma \tag{A.17}$$

A.3 Eq. (2.11)

The derivative of Eq. (2.1) with respect to time is:

$$\dot{E}_t = \dot{\Psi}_s + \dot{\Psi}_c - \dot{P}_{ext} \tag{A.18}$$

Each part of Eq. (A.18) will be calculated separately.

The derivative of Ψ_s becomes:

$$\dot{\Psi}_s = \frac{\partial}{\partial t}\int_{\Omega\setminus\Gamma} \psi(\varepsilon_{ij}(u_i), \Gamma) \ \mathrm{d}\mathcal{V}$$

$$\dot{\Psi}_s = \int_{\Omega\setminus\Gamma} \frac{\partial \psi}{\partial \varepsilon_{ij}}\dot{\varepsilon_{ij}} \ \mathrm{d}\mathcal{V} + \frac{\partial \psi_s}{\partial \Gamma}\dot{\Gamma}$$

But $\dfrac{\partial \psi}{\partial \varepsilon_{ij}} = \sigma_{ij}$, so it gets:

$$\dot{\Psi}_s = \int_{\Omega\setminus\Gamma} \sigma_{ij}\dot{\varepsilon_{ij}}\ \mathrm{d}\mathcal{V} + \frac{\partial \psi_s}{\partial \Gamma}\dot{\Gamma} \tag{A.19}$$

Before a few algebraic manipulations and, applying the divergence theorem like it was done on Appendix A.1, it gets from Eq. (A.19):

$$\dot{\Psi}_s = \int_{\Omega\setminus\Gamma} b_i\dot{u_i}\ \mathrm{d}\mathcal{V} + \int_{\partial\Omega_t} t_i\dot{u_i}\ \mathrm{d}\mathcal{A} + \int_{\partial\Omega_u} \sigma_{ij}n_j\dot{u_i}\ \mathrm{d}\mathcal{A} + \frac{\partial \Psi_s}{\partial \Gamma}\dot{\Gamma} \tag{A.20}$$

Deriving Ψ_c, it gets:

$$\dot{\Psi}_c = \frac{\partial}{\partial t}\int_{\Gamma} G_c\ d\Gamma = G_c\dot{\Gamma} \tag{A.21}$$

The derivative of the potential energy of external forces P_{ext} becomes:

$$\dot{P}_{ext} = \int_{\Omega\setminus\Gamma} (\dot{b_i}u_i + b_i\dot{u_i})\ \mathrm{d}\mathcal{V} + \int_{\partial\Omega_t} (\dot{t_i}u_i + t_i\dot{u_i})\ \mathrm{d}\mathcal{A} \tag{A.22}$$

Substituting Eq. (A.20), Eq. (A.21) and Eq. (A.22) in Eq. (A.18) it obtains:

$$\dot{E}_t = \int_{\partial\Omega_u} \sigma_{ij}n_j\dot{u_j}\ \mathrm{d}\mathcal{A} - \int_{\Omega\setminus\Gamma} \dot{b_i}u_i\ \mathrm{d}\mathcal{V} - \int_{\Omega_t} \dot{t_i}u_i\ \mathrm{d}\mathcal{A} + \left(\frac{\partial \Psi_s}{\partial \Gamma} + G_c\right)\dot{\Gamma} \tag{A.23}$$

In symbolic form:

$$\dot{E}_t = \int_{\partial\Omega_u} (\underline{\sigma}\cdot\bar{n})\cdot\dot{\bar{u}}\ \mathrm{d}\mathcal{A} - \int_{\Omega\setminus\Gamma} \dot{\bar{b}}\cdot\bar{u}\ \mathrm{d}\mathcal{V} - \int_{\Omega_t} \dot{\bar{t}}\cdot\bar{u}\ \mathrm{d}\mathcal{A} + \left(\frac{\partial \Psi_s}{\partial \Gamma} + G_c\right)\dot{\Gamma} \tag{A.24}$$

Comparing Eq. (A.24) with Eq. (2.6), it concluded as it wanted to be demonstrated:

$$\left(\frac{\partial \Psi_s}{\partial \Gamma} + G_c\right)\dot{\Gamma} = 0 \Rightarrow (\mathcal{G} - G_c)\dot{\Gamma} = 0 \tag{A.25}$$

A.4 Eq. (2.14)

The demonstration of Miehe et al. (2010a) phase-field model equations will begun from Eq. (2.13b). From that, it is defined the functional F:

$$F = \frac{1}{2}(\phi^2 + l_0^2(\phi')^2) \tag{A.26}$$

For minimize the functional given by Eq. (A.26), it will be used the following Euler's Rule:

$$\frac{\partial F}{\partial \phi} - \left(\frac{\partial F}{\partial \phi'}\right)' = 0 \tag{A.27}$$

In this way, it has:

$$\frac{\partial F}{\partial \phi} = \phi \tag{A.28a}$$

$$\frac{\partial F}{\partial \phi'} = l_0^2 \phi' \tag{A.28b}$$

Substituting Eq. (A.28) in Eq. (A.27), it gets in the Eq. (A.29):

$$\phi - l_0^2 \phi'' = 0 \tag{A.29}$$

It can be proved that Eq. (2.13a) is the solution of Eq. (A.29). It's easy to demonstrate that. Just replace Eq. (A.30) in Eq. (A.29).

$$\phi = e^{-|x|/l_0} \tag{A.30a}$$

$$\phi'' = \frac{1}{l_0^2} e^{-|x|/l_0} \tag{A.30b}$$

Now, it's going to be solved the Eq. (2.13b) for Eq. (2.13a):

$$I = \frac{1}{2}\int_0^L 2e^{-2x/l_0}\Gamma dx + \frac{1}{2}\int_{-L}^0 2e^{2x/l_0}\Gamma dx$$

$$I = \Gamma\left[-\frac{l_0}{2}e^{-2x/l_0}\Big|_0^L + \frac{l_0}{2}e^{2x/l_0}\Big|_{-L}^0\right] = \Gamma l_0 \tag{A.31}$$

As it can be seen, the Eq. (A.31) give the sharp crack surface multiplied by the length parameter l_0. To get a function that obtains the own crack sharp surface it is defined the functional:

$$\Gamma_l = \frac{1}{l_0} I(\phi, \phi') \tag{A.32}$$

A.5 Eq. (2.21)

In order to demonstrate the final equation of total energy function, it was calculated the first variation of Eq. (2.20). From that, it haves:

$$\begin{aligned}\delta E_t = \int_\Omega \sigma_{ij}\delta\varepsilon_{ij}\ \mathrm{d}\mathcal{V} + \int_\mathcal{B} \frac{\partial \psi}{\partial \phi}\delta\phi\ \mathrm{d}\mathcal{V} - \int_\Omega b_i \delta u_i\ \mathrm{d}\mathcal{V} - \int_{\partial\Omega_t} t_i \delta u_i\ \mathrm{d}\mathcal{A} + \\ + \int_\mathcal{B} G_c\left(\frac{\partial \gamma}{\partial \phi}\delta\phi + \frac{\partial \gamma}{\partial \phi_{,i}}\delta\phi_{,i}\right)\ \mathrm{d}\mathcal{V}\end{aligned} \tag{A.33}$$

In analogy in witch was demonstrated on Appendix A.1:

$$\int_\Omega \sigma_{ij}\delta\varepsilon_{ij}\ \mathrm{d}\mathcal{V} = \int_{\partial\Omega}(\sigma_{ij}n_j)\delta u_i\ \mathrm{d}\mathcal{A} - \int_\Omega \sigma_{ij,j}\delta u_i\ \mathrm{d}\mathcal{V} \tag{A.34}$$

Substituting Eq. (A.34) in Eq. (A.33) it gets:

$$\begin{aligned}\delta E_t = &- \int_\Omega (\sigma_{ij,j} + b_i) u_i \ \mathrm{d}\mathcal{V} + \int_{\Omega_t} (\sigma_{ij} n_j - t_i) \delta u_i \ \mathrm{d}\mathcal{A} + \\ &+ \int_\mathcal{B} \left[G_c \left(\frac{\partial \gamma}{\partial \phi} \delta\phi + \frac{\partial \gamma}{\partial \phi_{,i}} \cdot \delta\phi_{,i} \right) + \frac{\partial \psi}{\partial \phi} \delta\phi \right] \ \mathrm{d}\mathcal{V}\end{aligned} \tag{A.35}$$

The last integrate in domain $\mathcal{B}$ of Eq. (A.35), defined here as A, can be re-written as:

$$A = \int_\mathcal{B} \frac{\partial \psi}{\partial \phi} \delta\phi \ \mathrm{d}\mathcal{V} + \int_\mathcal{B} G_c \frac{\partial \gamma}{\partial \phi} \delta\phi \ \mathrm{d}\mathcal{V} + \int_\mathcal{B} G_c \frac{\partial \gamma}{\partial \phi_{,i}} \phi_{,i} \ \mathrm{d}\mathcal{V} \tag{A.36}$$

Consider what follows:

$$\begin{aligned}\left(\frac{\partial \gamma}{\partial \phi_{,i}} \delta\phi \right)_{,i} &= \left(\frac{\partial \gamma}{\partial \phi_{,i}} \right)_{,i} \delta\phi + \frac{\partial \gamma}{\partial \phi_{,i}} \delta\phi_{,i} \\ \frac{\partial \gamma}{\partial \phi_{,i}} \delta\phi_{,i} &= \left(\frac{\partial \gamma}{\partial \phi_{,i}} \delta\phi \right)_{,i} - \left(\frac{\partial \gamma}{\partial \phi_{,i}} \right)_{,i} \delta\phi\end{aligned} \tag{A.37}$$

Substituting Eq. (A.37) in Eq. (A.36), before applying the Divergence Theorem comes:

$$A = \int_\mathcal{B} \left[\frac{\partial \psi}{\partial \phi} + G_c \delta_\phi \gamma \right] \delta\phi \ \mathrm{d}\mathcal{V} + \int_{\partial\mathcal{B}} G_c \frac{\partial \gamma}{\partial \phi_i} n_i \delta\phi \ \mathrm{d}\mathcal{A} \tag{A.38}$$

Where:

$$\delta_\phi \gamma = \frac{\partial \gamma}{\partial \phi} - \left(\frac{\partial \gamma}{\partial \phi_{,i}} \right)_{,i} \tag{A.39}$$

Substituting Eq. (A.38) in A.35 we arrives in Eq. (2.21) as it would want to demonstrated:

$$\begin{aligned}\delta E_t = &- \int_\Omega (\sigma_{ij,j} + b_i) \delta u_i \ \mathrm{d}\mathcal{V} + \int_{\partial\Omega_t} (\sigma_{ij} n_j - t_i) \delta u_i \ \mathrm{d}\mathcal{A} + \int_\mathcal{B} \left[\frac{\partial \psi}{\partial \phi} + G_c \delta_\phi \gamma \right] \delta\phi \ \mathrm{d}\mathcal{V} + \\ &+ \int_{\nabla\mathcal{B}} G_c \left(\frac{\partial \gamma}{\partial \phi_{,i}} n_i \right) \delta\phi \ \mathrm{d}\mathcal{A}\end{aligned} \tag{A.40}$$

In symbolic notation:

$$\begin{aligned}\delta E_t = &- \int_\Omega (\nabla \underline{\sigma} + \bar{b}) \cdot \delta\bar{u} \ \mathrm{d}\mathcal{V} + \int_{\partial\Omega_t} (\underline{\sigma} \cdot \bar{n} - \bar{t}) \cdot \delta\bar{u} \ \mathrm{d}\mathcal{A} + \int_\mathcal{B} \left[\frac{\partial \psi}{\partial \phi} + G_c \delta_\phi \gamma \right] \delta\phi \ \mathrm{d}\mathcal{V} + \\ &+ \int_{\nabla\mathcal{B}} G_c \left(\frac{\partial \gamma}{\partial \nabla\phi} \cdot \bar{n} \right) \delta\phi \ \mathrm{d}\mathcal{A}\end{aligned} \tag{A.41}$$

A.6 Eq. (2.24)

To demonstrate Equations 2.24, the energy functional (Eq. (2.1)) will be derived with respect to time:

$$\dot{E}_t = \dot{\Psi}_s + \dot{\Psi}_c - \dot{P}_{ext} \tag{A.42}$$

In that way, each part of Eq. (A.42) have to be calculated. For Ψ_s it gets:

$$\dot{\Psi}_s = \frac{\partial}{\partial t}\left[\int_\Omega \psi(\underline{\varepsilon}(\bar{u}), \phi)\ \mathrm{d}\mathcal{V}\right] = \int_\Omega \sigma_{ij}\varepsilon_{ij}\ \mathrm{d}\mathcal{V} + \int_\mathcal{B} \frac{\partial \psi}{\partial \phi}\dot{\phi}\ \mathrm{d}\mathcal{V} \tag{A.43}$$

Making the same that was done on Appendix A.1, Eq. (A.43) becomes:

$$\dot{\Psi}_s = \int_{\partial\Omega} \sigma_{ij} n_j \dot{u}_i\ \mathrm{d}\mathcal{A} - \int_\Omega \sigma_{ij,j}\dot{u}_i\ \mathrm{d}\mathcal{V} + \int_\mathcal{B} \frac{\partial \psi}{\partial \phi}\dot{\phi}\ \mathrm{d}\mathcal{V} \tag{A.44}$$

For surface energy, comes:

$$\dot{\Psi}_c = \int_\mathcal{B} G_c \gamma(\phi, \phi_{,i})\ \mathrm{d}\mathcal{V} = \int_\mathcal{B} G_c \left[\frac{\partial \gamma}{\partial \phi}\dot{\phi} + \frac{\partial \gamma}{\partial \phi_{,i}}\dot{\phi}_{,i}\right]\ \mathrm{d}\mathcal{V} \tag{A.45}$$

Applying the divergence theorem, before some mathematical manipulations it arrives at:

$$\dot{\Psi}_c = \int_\mathcal{B} G_c \left[\frac{\partial \gamma}{\partial \phi} - \left(\frac{\partial \gamma}{\partial \phi_{,i}}\right)_{,i}\right]\dot{\phi}\ \mathrm{d}\mathcal{V} + \int_{\partial\mathcal{B}} G_c \frac{\partial \gamma}{\partial \phi_{,i}} n_i \dot{\phi}\ \mathrm{d}\mathcal{A} \tag{A.46}$$

But the second instalment of Eq. (A.46) is zero by boundary conditions. In that way:

$$\dot{\Psi}_c = \int_\mathcal{B} G_c \delta_\phi \gamma \dot{\phi}\ \mathrm{d}\mathcal{V} \tag{A.47}$$

where:

$$\delta_\phi \gamma = \frac{\partial \gamma}{\partial \phi} - \left(\frac{\partial \gamma}{\partial \phi_{,i}}\right)_{,i} \tag{A.48}$$

In symbolic notation, Eq. (A.48) is written as:

$$\delta_\phi \gamma = \frac{\partial \gamma}{\partial \phi} - \nabla \cdot \frac{\partial \gamma}{\partial \nabla \phi} \tag{A.49}$$

The derivative of external forces potential can be easy verified that:

$$\dot{P}_{ext} = \int_\Omega (\dot{b}_i u_i + b_i \dot{u}_i)\ \mathrm{d}\mathcal{V} + \int_{\partial\Omega_t} (\dot{t}_i u_i + t_i \dot{u}_i)\ \mathrm{d}\mathcal{A} \tag{A.50}$$

Substituting Eq. (A.46), Eq. (A.47) and Eq. (A.50) in Eq. (A.42) gets:

$$\dot{E}_t = \int_{\partial\Omega_u} \sigma_{ij} n_j \dot{u}_i \, \mathrm{d}\mathcal{A} + \int_{\partial\Omega_t} (\sigma_{ij} n_j - t_i)\dot{u}_i \, \mathrm{d}\mathcal{A} - \int_{\partial\Omega_t} \dot{t}_i u_i \, \mathrm{d}\mathcal{A} - \int_{\Omega} (\sigma_{ij,j} + b_i)\dot{u}_i \, \mathrm{d}\mathcal{V} + \\ - \int_{\Omega} \dot{b}_i u_i \, \mathrm{d}\mathcal{V} + \int_{\mathcal{B}} \frac{\partial \psi}{\partial \phi}\dot{\phi} \, \mathrm{d}\mathcal{V} + \int_{\mathcal{B}} G_c \delta_\phi \gamma \dot{\phi} \, \mathrm{d}\mathcal{V} \tag{A.51}$$

It's known that $\sigma_{ij} n_j - t_i = 0$ and $\sigma_{ij,j} + b_i = 0$, and comparing Eq. (A.51) with Eq. (2.6), it noted that the three first therms of A.51 are equal to $\dot{E}_t$. From this, considering $Y = \dfrac{\partial \psi}{\partial \phi}$, it arrives at the following:

$$\int_{\mathcal{B}} \left[Y - G_c \delta_\phi \gamma \right] \dot{\phi} \, \mathrm{d}\mathcal{V} = 0 \tag{A.52}$$

Observe that the therm in bracket of Eq. (A.52) is similar to Eq. (2.11). With that in mind, from Eq. (A.52) comes:

- For $\dot{\phi} > 0$ (it can't be smaller than zero by irreversibility condition):

$$Y - G_c \delta_\phi \gamma = 0 \tag{A.53}$$

- For $\dot{\phi} = 0$, to obey Eq. (2.11):

$$Y - G_c \delta_\phi \gamma < 0 \tag{A.54}$$

A.7 Eq. (2.38)

From Eq. (2.21), applying the conditions obtained on Eq. (2.23) and Eq. (2.25), and considering the Unilateral Stationary Condition, it gets:

$$\delta E_t = \int_{\mathcal{B}} \left[-Y + G_c \delta_\phi \gamma \right] \delta\phi \, \mathrm{d}\mathcal{V} \geq 0 \tag{A.55}$$

Substituting Eq. (2.26d) and Eq. (2.32b) in Eq. (A.55):

$$\delta E_t = \int_{\mathcal{B}} g'(\phi) \bar{Y} \delta\phi \, \mathrm{d}\mathcal{V} + \int_{\mathcal{B}} \frac{G_c}{C_0} \frac{1}{l_0} \alpha'(\phi) \delta\phi \, \mathrm{d}\mathcal{V} - \int_{\mathcal{B}} \frac{2G_c}{C_0} l_0 \phi_{,ii} \delta\phi \, \mathrm{d}\mathcal{V} \geq 0 \tag{A.56}$$

Considering $(\phi_{,i}\delta\phi)_{,i} = \phi_{,ii}\delta\phi + \phi_{,i}\delta\phi_{,i}$ it can be said that:

$$\phi_{,ii}\delta\phi = (\phi_{,i}\delta\phi)_{,i} - \phi_{,i}\delta\phi_{,i} \tag{A.57}$$

Substituting what was obtained in Eq. (A.57) in the last integral of Eq. (A.56), and

applying the divergence theorem, it comes to:

$$\int_{\mathcal{B}} \frac{2G_c}{C_0} l_0 \phi_{,ii} \delta\phi \ \mathrm{d}\mathcal{V} = \frac{2G_c l_0}{C_0} \left[\int_{\partial\mathcal{B}} \phi_{,i} \delta\phi n_i dA - \int_{\mathcal{B}} \phi_{,i} \delta\phi_{,i} \ \mathrm{d}\mathcal{V} \right] \tag{A.58}$$

But, the first integral on brackets of Eq. (A.58) is zero because the variable ϕ don't varies on boundary $\partial\mathcal{B}$, that is, $\delta\phi = 0$. With this consideration, substituting Eq. (A.58) in Eq. (A.56) it obtains:

$$\delta E_t = \int_{\mathcal{B}} \left[g'(\phi) \bar{Y} \delta\phi + \frac{G_c}{C_0} \left(\frac{1}{l_0} \alpha'(\phi) \delta\phi + 2 l_0 \phi_{,ii} \delta\phi \right) \right] \ \mathrm{d}\mathcal{V} \geq 0 \tag{A.59}$$

Calling $\delta\gamma = \dfrac{1}{C_0} \left[\dfrac{1}{l_0} \alpha'(\phi) \delta\phi + 2 l_0 \phi_{,ii} \delta\phi \right]$ it arrives on Eq. (A.60) as it would wanted to be demonstrated:

$$\int_{\mathcal{B}} \left[g'(\phi) \bar{Y} \delta\phi + G_c \delta\gamma \right] \ \mathrm{d}\mathcal{V} \geq 0 \tag{A.60}$$

In symbolic form, $\delta\gamma$ can be written as:

$$\delta\gamma = \frac{1}{C_0} \left[\frac{1}{l_0} \alpha'(\phi) \delta\phi + 2 l_0 \nabla\phi \cdot \nabla\delta\phi \right] \tag{A.61}$$

Appendix B

Numerical solution

In this chapter it will be demonstrated the analytical solution for a bar subject to a tension test. The demonstrations shown here can also be found in Wu et al. (2020) but the author of this manuscript wanted to put here too in order to facilitate future researches of phase-field modelling in Structures Department of UFMG.

To start the demonstrations, imagine a bar $x \in [-L, L]$, centred in the origin, loaded in both extremities in such way that the boundary conditions will not affect the phase-field evolution. When phase-field values becomes bigger, as it is demonstrated in Section 2.2.2, Eq. (B.1) is satisfied:

$$Y - G_c \delta_\phi \gamma = 0 \tag{B.1}$$

It also have the following definitions in phase-field theory:

$$Y = -g'(\phi)\bar{Y} \tag{B.2a}$$

$$\bar{Y} = \frac{1}{2}\sigma\varepsilon \tag{B.2b}$$

$$\sigma = g(\phi)E_0\varepsilon \tag{B.2c}$$

$$\delta_\phi \gamma = \frac{1}{C_0}\left[\frac{1}{l_0}\alpha'(\phi) - 2l_0\Delta\phi\right] \tag{B.2d}$$

Substituting Eq. (B.2) in Eq. (B.1), it arrives to:

$$\frac{1}{2}g'(\phi)g(\phi)E_0\varepsilon^2 + \frac{G_c}{C_0}\left[\frac{1}{l_0}\alpha'(\phi) - 2l_0\phi_{,xx}\right] = 0 \tag{B.3}$$

Now, let be introduced a monotonically increase function $\omega(\phi)$ defined as:

$$\omega(\phi) = \frac{1}{g(\phi)} - 1 \Longrightarrow g(\phi) = \frac{1}{1+\omega(\phi)} \tag{B.4}$$

The derivative of $g(\phi)$ becomes:

$$g'(\phi) = -g^2(\phi)\omega'(\phi) < 0 \tag{B.5}$$

Substituting Eq. (B.5) in Eq. (B.3) it gets:

$$\frac{1}{2}\left[-g^2(\phi)\omega'(\phi)\right]g(\phi)\mathbb{E}_0\varepsilon^2+\frac{G_c}{C_0}\left[\frac{1}{l_0}\alpha'(\phi)-2l_0\phi_{,xx}\right]=0 \tag{B.6}$$

Re-writing:

$$-\frac{1}{2}\frac{g(\phi)E_0\varepsilon}{E_0}\omega'(\phi)g(\phi)E_0\varepsilon+\frac{G_c}{C_0}\left[\frac{1}{l_0}\alpha'(\phi)-2l_0\phi_{,xx}\right]=0 \tag{B.7}$$

Substituting B.2c in B.7:

$$\sigma^2\omega'(\phi)-A_0\left[\alpha'(\phi)-2l_0^2\phi_{,xx}\right]=0,\quad A_0=\frac{2G_cE_0}{C_0l_0} \tag{B.8}$$

The displacement (u) in the end of the bar can be calculated by the elasticity formula:

$$u=\int_0^L\varepsilon dx,\quad \text{with } \varepsilon=\frac{\sigma}{E_0}[1+\omega(\phi)] \tag{B.9}$$

where the definition of ε was obtained from equations Eq. (B.2c) and Eq. (B.4).

B.1 Homogeneous solution

In this section the homogeneous solution will be considered, that is, the stress, strains and phase-field values are homogeneous along the bar domain. In this way $\phi_{,xx}=0$ and Eq. (B.8) becomes:

$$\sigma^2\omega'(\phi)-A_0\alpha'(\phi)=0 \tag{B.10}$$

Organizing Eq. (B.10) and using Eq. (B.9), the following can be written:

$$\sigma=\sqrt{A_0\frac{\alpha'(\phi)}{\omega'(\phi)}},\quad \varepsilon=\frac{1}{E_0}\sqrt{-A_0\frac{\alpha'(\phi)}{g'(\phi)}},\quad u=\varepsilon L=\frac{L}{E_0}\sqrt{-A_0\frac{\alpha'(\phi)}{g'(\phi)}} \tag{B.11}$$

To obtain the maximum value of traction that the material supports, the analysis will be based in the generic geometric crack function proposed by Wu (2017):

$$\alpha(\phi)=\xi\phi+(1-\xi)\phi^2,\quad \xi\in[0;2] \tag{B.12}$$

- When it is adopted $\xi=0$ it arrives in $\alpha(\phi)=\phi^2$, and according to Wu et al. (2020) the failure criterion is activated since the loading is applied. Deriving σ with relation to ϕ the critical point is obtained:

$$\frac{\partial\sigma}{\partial\phi}=0\Longrightarrow\frac{\partial\sigma}{\partial\phi}=\frac{1}{2}*\frac{A_0\dfrac{\alpha''(\phi)\omega'(\phi)-\alpha'(\phi)\omega''(\phi)}{(\omega'(\phi))^2}}{\sqrt{A_0\dfrac{\alpha'(\phi)}{\omega'(\phi)}}}=0 \tag{B.13}$$

Considering what was described in B.14 and with a few algebraic manipulations B.13 arrives to B.15:

$$\alpha'(\phi) = 2\phi \tag{B.14a}$$

$$\alpha''(\phi) = 2 \tag{B.14b}$$

$$\omega'(\phi) = -\frac{g'(\phi)}{g^2(\phi)} \tag{B.14c}$$

$$\omega''(\phi) = -\frac{g''(\phi)g(\phi) - 2(g'(\phi))^2}{g^3(\phi)} \tag{B.14d}$$

$$\left[g(\phi_c)g''(\phi_c) - 2(g'(\phi_c))^2\right]\phi_c = g'(\phi_c)g(\phi_c) \tag{B.15}$$

And the maximum value of traction is obtained by putting the value of critical point (ϕ_c) in Eq. (B.11).

In this work, in all examples analysed, it was used $g(\phi) = (1-\phi)^2$. With that, substituting in equation Eq. (B.15) it arrives to:

$$\phi_c = \frac{1}{4}, \qquad \sigma_c = \frac{3}{16}\sqrt{\frac{3E_0G_c}{l_0}}, \qquad \varepsilon_c = \sqrt{\frac{G_c}{3E_0l_0}} \tag{B.16}$$

- When it is adopted $\xi > 0$ the derivative of the geometric crack function in zero becomes $\alpha'(\phi) = \xi$. In this case, according to Wu et al. (2020) there is a initial state in which the material remains with $\phi = 0$. In this case, the peak stress occurs in the instant of damage initiation and for $\omega(0) > 0$ it can be written:

$$\sigma_c = \lim_{\phi\to 0}\sqrt{A_0\frac{\alpha'(\phi)}{\omega'(\phi)}}, \qquad \varepsilon_c = \lim_{\phi\to 0}\frac{1}{E_0}\sqrt{-A_0\frac{\alpha'(\phi)}{g'(\phi)}} \tag{B.17}$$

For $\omega'(0) = 0$, Wu et al. (2020) defines:

$$\sigma_c = \lim_{\phi\to 0}\sqrt{A_0\frac{\alpha''(\phi)}{\omega''(\phi)}}, \qquad \varepsilon_c = \lim_{\phi\to 0}\frac{1}{E_0}\sqrt{A_0\frac{\alpha''(\phi)}{\omega''(\phi)}} \tag{B.18}$$

B.2 Localised solution

The localised solution assumes that phase-field evolution will start in a certain point, and it will grow. In this demonstration, assume that the localized band is centred in $x = 0$ and extends for the domain $[-D, D]$ where D is a half bandwidth, not necessarily constant, in such way that $D \ll L$. Multiplying Eq. (B.8) by $\phi_{,x}$ and integrating with respect to x

goes to:

$$\sigma^2\omega(\phi) - A_0\left[\alpha(\phi) - (l_0\phi_{,x})^2\right] = 0 \tag{B.19}$$

In boundary condition of the localization band, it is considered that

$$\phi(x = \pm D) = 0, \quad \phi_{,x}(x = \pm D) = 0, \quad \omega(\phi(x = \pm D)) = 0. \tag{B.20}$$

For a given displacement u^*, because of symmetry, the maximum value of phase-field (ϕ^*) will occurs in $x = 0$ where $\phi_{,x} = 0$. In this case, Eq. (B.19) becomes:

$$\sigma^2\omega(\phi^*) - A_0\alpha(\phi^*) = 0 \Longrightarrow \sigma = \sqrt{A_0\frac{\alpha(\phi^*)}{\omega(\phi^*)}} \tag{B.21}$$

The failure strength is determined upon the instant of damage initiation, so applying L'Hôpital to calculate the indeterminate limit, it gets:

$$f_t = \lim_{\phi* \to 0}\sigma = \sqrt{A_0\frac{\alpha'(0)}{\omega'(0)}} = \sqrt{\frac{2G_c\mathbb{E}_0}{C_0 l_0}\frac{\alpha'(0)}{\omega'(0)}}, \quad A_0 = f_t^2\frac{\omega'(0)}{\alpha'(0)} = \frac{2G_c\mathbb{E}_0}{C_0 l_0} \tag{B.22}$$

Considering that, Eq. (B.21) can be re-written as:

$$\sigma = f_t\sqrt{\frac{\omega'(0)}{\alpha'(0)}\frac{\alpha(\phi^*)}{\omega(\phi^*)}} \tag{B.23}$$

From Eq. (B.19), $\phi_{,x}$ is:

$$\phi_{,x} = \frac{1}{l_0}\sqrt{\alpha(\phi) - \frac{\sigma^2}{A_0}\omega(\phi)} \tag{B.24}$$

Substituting Eq. (B.21) in Eq. (B.24), becomes:

$$\phi_{,x} = \frac{d\phi}{dx} = -\frac{1}{l_0}\mathcal{F}, \quad \mathcal{F} = \sqrt{\alpha(\phi) - \frac{\alpha(\phi^*)}{\omega(\phi^*)}\omega(\phi)} \tag{B.25}$$

The negative signal is explained due the fact that ϕ is monotonically decreasing in the interval $x \in [0; L]$.

With this is mind, to calculate the position of a given phase-field it can be done:

$$x(\phi, \phi^*) = l_0\int_{\phi}^{\phi^*}\mathcal{F}^{-1}(\bar{\phi}, \phi^*)d\bar{\phi} \tag{B.26}$$

And the size of half damaged part of the bar:

$$D(\phi^*) = l_0\int_{0}^{\phi^*}\mathcal{F}^{-1}(\bar{\phi}, \phi^*)d\bar{\phi} \tag{B.27}$$

And the displacement imposed at the free end of the bar ($x = L$):

$$u(\phi^*) = \frac{\sigma}{\mathbb{E}_0} L + \frac{1}{2} w(\phi^*) dx \tag{B.28}$$

where $w(\phi^*)$ is defined:

$$w(\phi^*) = \frac{2\sigma}{\mathbb{E}_0} \int_0^D \omega(\phi) dx \tag{B.29}$$

Using Eq. (B.22), Eq. (B.23) and Eq. (B.24), it gets to:

$$w(\phi^*) = \frac{4G_f}{C_0 f_t} \sqrt{\frac{\alpha'(0)}{\omega'(0)}} \int_0^{\phi^*} \sqrt{\frac{\alpha(\phi^*)}{\alpha(\bar{\phi})\omega(\phi^*) - \alpha(\phi^*)\omega(\bar{\phi})}} \omega(\bar{\phi}) d\bar{\phi} \tag{B.30}$$

Appendix C

Demonstration of FEM equations

The demonstration of FEM discretization will strat from Eq. (2.38a), that in Voight's notation can be written as:

$$\int_{\Omega} \delta\bar{\varepsilon}^T \bar{\sigma} \, \mathrm{d}\mathcal{V} = \delta\bar{d}^T \bar{f}_I$$

Substituting $\delta\bar{\varepsilon} = [\mathbf{B}]_I^u \, \delta\bar{d}$, it arrives to:

$$\delta\bar{d}^T \int_{\Omega} [\mathbf{B}]_I^{u,T} \, \bar{\sigma} \, \mathrm{d}\mathcal{V} = \delta\bar{d}^T \bar{f}_I \tag{C.1}$$

As $\delta\bar{d}$ is arbitrary, Eq. (C.1) comes to the already known Eq. (C.2):

$$\int_{\Omega} [\mathbf{B}]_I^{u,T} \, \bar{\sigma} \, \mathrm{d}\mathcal{V} = \bar{f}_I \tag{C.2}$$

Substituting the the definitions of Eq. (2.42) in Eq. (2.38b):

$$\int_{\mathcal{B}} g'\bar{Y}\delta\bar{a}^T \, [\mathbf{N}]_I^{\phi,T} + \frac{1}{C_0}\left(\frac{1}{l_0}\alpha'\delta\bar{a}^T \, [\mathbf{N}]_I^{\phi,T} + 2l_0\delta\bar{a}^T \, [\mathbf{B}]_I^{\phi,T} \, \nabla\phi\right) \, \mathrm{d}\mathcal{V} \geq \bar{0}_I \tag{C.3}$$

But $\delta\bar{a}$ is arbitrary, so Eq. (C.3) can be re-written as:

$$\int_{\mathcal{B}} g'\bar{Y} \, [\mathbf{N}]_I^{\phi,T} + \frac{1}{C_0}\left(\frac{1}{l_0}\alpha' \, [\mathbf{N}]_I^{\phi,T} + 2l_0 \, [\mathbf{B}]_I^{\phi,T} \, \nabla\phi\right) \, \mathrm{d}\mathcal{V} \geq \bar{0}_I \tag{C.4}$$

As it would wanted to be demonstrated Eq. (C.2) and Eq. (C.4) are the discrete form of the phase-field governing equations and the residual form of then can be written as:

$$\bar{r}_I^u = \int_{\Omega} [\mathbf{B}]_I^{u,T} \, \bar{\sigma} \, \mathrm{d}\mathcal{V} - \bar{f}_{ext} = \bar{0}_I \tag{C.5a}$$

$$\bar{r}_I^{\phi} = -\int_{\mathcal{B}} [\mathbf{N}]_I^{\phi,T} \left(g'\bar{Y} + \frac{1}{C_0 l_0}\alpha' G_c\right) \, \mathrm{d}\mathcal{V} - \int_{\mathcal{B}} \frac{2l_0}{C_0} G_c \, [\mathbf{B}]_I^{\phi,T} \, \nabla\phi \, \mathrm{d}\mathcal{V} \leq \bar{0}_I \tag{C.5b}$$

To obtain the tangent stiffness matrix it is necessary to derive the left part of Eq. (C.2) and Eq. (C.4) with respect to the nodal displacements vector ($\bar{d}$) and the nodal phase-field

vector ($\bar{a}$). In this way, starting from Eq. (C.2) and applying the chain rule, it gets:

$$[\mathbf{K^{uu}}]_{IJ} = \int_{\Omega} [\mathbf{B}]_I^{u,T} \frac{\partial \bar{\sigma}}{\partial \bar{\varepsilon}} \frac{\partial \bar{\varepsilon}}{\partial \bar{d}_J} \, \mathrm{d}\mathcal{V} \tag{C.6}$$

But, from Eq. (2.40b):

$$[\mathbf{K^{uu}}]_{IJ} = \int_{\Omega} [\mathbf{B}]_I^{u,T} \frac{\partial \bar{\sigma}}{\partial \bar{\varepsilon}} [\mathbf{B}]_J^{u} \, \mathrm{d}\mathcal{V} \tag{C.7}$$

Now, deriving Eq. (C.2) with respect to nodal phase-field $\bar{a}$ it arrives to:

$$\left[\mathbf{K^{u\phi}}\right]_{IJ} = \int_{\Omega} [\mathbf{B}]_I^{u,T} \frac{\partial \bar{\sigma}}{\partial \phi} \frac{\partial \phi}{\partial \bar{a}_J} \, \mathrm{d}\mathcal{V} \tag{C.8}$$

Using the definition 2.42a, Eq. (C.8) can be rewritten as:

$$\left[\mathbf{K^{u\phi}}\right]_{IJ} = \int_{\Omega} [\mathbf{B}]_I^{u,T} \frac{\partial \bar{\sigma}}{\partial \phi} [\mathbf{N}]_J^{\phi} \, \mathrm{d}\mathcal{V} \tag{C.9}$$

In analogy in what was done above, deriving the left part of Eq. (C.4) with respect to displacements (d) gets:

$$\left[\mathbf{K^{\phi u}}\right]_{IJ} = \int_{\mathcal{B}} [\mathbf{N}]_I^{\phi,T} g' \frac{\partial \bar{Y}}{\partial \bar{\varepsilon}} [\mathbf{B}]_J^{u} \, \mathrm{d}\mathcal{V} \tag{C.10}$$

Now, with respect to phase-field vector ($\bar{a}$), obtains:

$$\left[\mathbf{K^{\phi\phi}}\right]_{IJ} = \int_{\mathcal{B}} [\mathbf{N}]_I^{\phi,T} \left(g'' \bar{Y} + \frac{1}{C_0 l_0} \alpha'' G_c \right) [\mathbf{N}]_J^{\phi} \, \mathrm{d}\mathcal{V} + \int_{\mathcal{B}} \frac{2 l_0}{C_0} G_c \, [\mathbf{B}]_I^{\phi,T} [\mathbf{B}]_J^{\phi} \, \mathrm{d}\mathcal{V} \tag{C.11}$$

So, the tangent stiffness matrix becomes:

$$[\mathbf{K}] = \begin{bmatrix} [\mathbf{K^{uu}}] & \left[\mathbf{K^{u\phi}}\right] \\ \left[\mathbf{K^{\phi u}}\right] & \left[\mathbf{K^{\phi\phi}}\right] \end{bmatrix} \tag{C.12}$$

with its therms defined on Eq. (C.7), Eq. (C.9), Eq. (C.10) and Eq. (C.11).

Appendix D

Constitutive and stress tensors

It is already known that the strain tensor and the tangent constitutive tensor is obtained, respectively, by deriving once and twice the strain energy density with respect to the strain tensor. So, from Eq. (2.36):

$$\sigma_{ij} = \frac{\partial \psi}{\partial \varepsilon_{ij}} = g(\phi)\frac{\partial \psi_0^+}{\partial \varepsilon_{ij}} + \frac{\partial \psi_0^-}{\partial \varepsilon_{ij}} \tag{D.1a}$$

$$C_{ijkl} = \frac{\partial^2 \psi}{\partial \varepsilon_{ij}\partial \varepsilon_{kl}} = g(\phi)\frac{\partial \psi_0^+}{\partial \varepsilon_{ij}\partial \varepsilon_{kl}} + \frac{\partial \psi_0^-}{\partial \varepsilon_{ij}\partial \varepsilon_{kl}} \tag{D.1b}$$

From Eq. (D.1), it is demonstrated in this appendix stress and the constitutive tensor for the constitutive models presented in this work.

D.1 Eq. (2.57): Lancioni and Royer-Carfagni (2009)

Rewriting strain energy density proposed by Lancioni and Royer-Carfagni (2009) in index notation it gets:

$$\psi_0^+ = \mu_0 \left(\varepsilon_{ij}\varepsilon_{ij} - \frac{1}{3}(\varepsilon_{ij}\delta_{ij})^2 \right) \tag{D.2a}$$

$$\psi_0^- = \frac{1}{2} K_0 (\varepsilon_{ij}\delta_{ij})^2 \tag{D.2b}$$

Deriving Eq. (D.2) with respect to strain tensor once and twice it obtains:

$$\frac{\partial \psi_0^+}{\partial \varepsilon_{kl}} = 2\mu_0 \left(\varepsilon_{kl} - \frac{1}{3}\varepsilon_{ij}\delta_{ij}\delta_{kl} \right) \tag{D.3a}$$

$$\frac{\partial \psi_0^-}{\partial \varepsilon_{kl}} = K_0 \varepsilon_{ij}\delta_{ij}\delta_{kl} \tag{D.3b}$$

$$\frac{\partial \psi_0^+}{\partial \varepsilon_{kl}\partial \varepsilon_{mn}} = 2\mu_0 \left(\delta_{mnkl} - \frac{1}{3}\delta_{mn}\delta_{kl} \right) \tag{D.3c}$$

$$\frac{\partial \psi_0^-}{\partial \varepsilon_{kl}\partial \varepsilon_{mn}} = K_0 \delta_{ij}\delta_{mn} \tag{D.3d}$$

Substituting Eq. (D.3) in Eq. (D.1) it gets, in symbolic form:

$$\sigma = g(\phi)\ 2\mu_0 \left(\underline{\varepsilon} - \frac{1}{3}\mathrm{tr}(\underline{\varepsilon})\underline{I} \right) + K_0 \mathrm{tr}(\underline{\varepsilon})\underline{I} \tag{D.4a}$$

$$\hat{\mathbf{C}} = 2g(\phi)\mu_0 \left(\frac{1}{3}\mathrm{tr}(\underline{\varepsilon})\underline{I} \right) + K_0 \underline{I} \otimes \underline{I} \tag{D.4b}$$

D.2 Eq. (2.58c) and Eq. (2.58d): Amor et al. (2009)

Writing Eq. (2.58a) and Eq. (2.58b) in index notation:

$$\psi_0^+ = \frac{1}{2}K_0 R_n^+ (\varepsilon_{ij}\delta_{ij})^2 + \mu_0 \left[\varepsilon_{ij}\varepsilon_{ij} - \frac{1}{3}(\varepsilon_{ij}\delta_{ij})^2 \right] \tag{D.5a}$$

$$\psi_0^- = \frac{1}{2}K_0 R_n^- (\varepsilon_{ij}\delta_{ij})^2 \tag{D.5b}$$

Derivating Eq. (D.5) with respect to the strain tensor, it gets:

$$\frac{\partial \psi_0^+}{\partial \varepsilon_{kl}} = K_0 R_n^+ \varepsilon_{ij}\delta_{ij}\delta_{kl} + 2\mu_0 \left(\varepsilon_{kl} - \frac{1}{3}\varepsilon_{ij}\delta_{ij}\delta_{kl} \right) \tag{D.6a}$$

$$\frac{\partial \psi_0^-}{\partial \varepsilon_{kl}} = K_0 R_n^- \varepsilon_{ij}\delta_{ij}\delta_{kl} \tag{D.6b}$$

$$\frac{\partial \psi_0^+}{\partial \varepsilon_{kl}\partial \varepsilon_{mn}} = K_0 R_n^+ \delta_{mn}\delta_{kl} + 2\mu_0 \left(\delta_{mnkl} - \frac{1}{3}\delta_{mn}\delta_{kl} \right) \tag{D.6c}$$

$$\frac{\partial \psi_0^-}{\partial \varepsilon_{kl}\partial \varepsilon_{mn}} = K_0 R_n^- \delta_{mn}\delta_{kl} \tag{D.6d}$$

From Eq. (D.6), the stress and the constitutive tensor can be written, in symbolic form, as:

$$\underline{\sigma} = g(\phi) \left[K_0 R_n^+ \underline{\varepsilon} : \underline{I} \otimes \underline{I} + 2\mu_0 \left(\underline{\varepsilon} - \frac{1}{3}\underline{\varepsilon} : \underline{I} \otimes \underline{I} \right) \right] + K_0 R_n^- \underline{\varepsilon} : \underline{I} \otimes \underline{I} \tag{D.7a}$$

$$\hat{\mathbf{C}} = g(\phi) \left[K_0 R_n^+ \underline{I} \otimes \underline{I} + 2\mu_0 \left(\hat{\mathbf{I}} - \frac{1}{3}\underline{I} \otimes \underline{I} \right) \right] + K_0 R_n^- \underline{I} \otimes \underline{I} \tag{D.7b}$$

D.3 Eq. (2.63): Miehe et al. (2010b)

In this section will be demonstrated the form of constitutive and stress tensor proposed by Miehe et al. (2010b). For that, it is firstly necessary to demonstrate the construction of the fourth order tensor $\hat{\mathbf{P}}^{\pm}$. Due that, this section is splitted in two subsections: the first, in which in demonstrated the $\hat{\mathbf{P}}^{\pm}$ tensor, and the second, with the demonstrations of constitutive and stress tensor itself.

D.3.1 The fourth order $\hat{\mathbf{P}}^{\pm}$ tensor

The value of $\langle \varepsilon_n \rangle_+$ defined in Eq. (2.60), using the definitions given in Eq. (2.49), can be rewritten as:

$$\langle \varepsilon_n \rangle_+ = \varepsilon_n \frac{1 + \mathrm{sgn}(\varepsilon_n)}{2} = \varepsilon_n \mathrm{H}(\varepsilon_n) \tag{D.8}$$

Rewriting Eq. (2.60a):

$$\varepsilon_{ij}^{+} = \sum_{n=1}^{3} \varepsilon_n \mathrm{H}(\varepsilon_n) p_{n_i} p_{n_j} \tag{D.9}$$

It is wanted a fourth order tensor P_{ijkl}^{+} in such way that:

$$\varepsilon_{ij}^{+} = P_{ijkl}^{+} \varepsilon_{kl} = P_{ijkl}^{+} \sum_{n=1}^{3} \varepsilon_n p_{n_k} p_{n_l} \tag{D.10}$$

Matching Eq. (D.9) and Eq. (D.10), it gets to:

$$P_{ijkl}^{+} \sum_{n=1}^{3} p_{n_k} p_{n_l} = \sum_{n=1}^{3} \mathrm{H}(\varepsilon_n) p_{n_i} p_{n_j} \tag{D.11}$$

If P_{ijkl}^{+} is a fourth order tensor, it can be defined by:

$$P_{ijkl}^{+} = \alpha a_i b_j c_k d_l \tag{D.12}$$

where α is a constant value.

Substituting Eq. (D.12) in Eq. (D.11):

$$\alpha a_i b_j c_k d_l \sum_{n=1}^{3} p_{n_k} p_{n_l} = \sum_{n=1}^{3} \mathrm{H}(\varepsilon_n) p_{n_i} p_{n_j} \tag{D.13}$$

Both sides of equations needs to be equal. For that is is necessary:

$$\alpha = \mathrm{H}(\varepsilon_n) \tag{D.14a}$$
$$a_i = p_{n_i} \tag{D.14b}$$
$$b_j = p_{n_j} \tag{D.14c}$$
$$c_k p_{n_k} = 1 \tag{D.14d}$$
$$d_l p_{n_l} = 1 \tag{D.14e}$$

To satisfy Eq. (D.14d) and Eq. (D.14e), it needs that:

$$c_k \equiv p_{n_k},\ \|c_k\| = \|p_{n_k}\| = 1 \tag{D.15a}$$
$$d_l \equiv p_{n_l},\ \|d_l\| = \|p_{n_l}\| = 1 \tag{D.15b}$$

So:

$$P^+_{ijkl} = \sum_{n=1}^{3} \mathrm{H}(\varepsilon_n) p_{n_i} p_{n_j} p_{n_k} p_{n_l} \tag{D.16}$$

In symbolic notation:

$$\hat{\mathbf{P}}^+ = \sum_{n=1}^{3} \mathrm{H}(\varepsilon_n) \bar{p}_n \otimes \bar{p}_n \otimes \bar{p}_n \otimes \bar{p}_n \tag{D.17}$$

D.3.2 The constitutive and stress tensor

The strain energy density, in index notation becomes:

$$\psi_0^+ = \frac{1}{2}\lambda_0 R_n^+ (\delta_{ij}\varepsilon_{ij})^2 + \mu_0 \varepsilon_{ij}^+ \varepsilon_{ij}^+ \tag{D.18a}$$
$$\psi_0^- = \frac{1}{2}\lambda_0 R_n^- (\delta_{ij}\varepsilon_{ij})^2 + \mu_0 \varepsilon_{ij}^- \varepsilon_{ij}^- \tag{D.18b}$$

The stress tensor is calculated, in this case, by:

$$\sigma_{ij} = g(\phi)\frac{\partial \psi_0^+}{\partial \varepsilon_{ij}} + \frac{\partial \psi_0^-}{\partial \varepsilon_{ij}} = g(\phi)\frac{\partial \psi_0^+}{\partial \varepsilon_{ij}^+}\frac{\partial \varepsilon_{ij}^+}{\partial \varepsilon_{ij}} + \frac{\partial \psi_0^-}{\partial \varepsilon_{ij}^-}\frac{\partial \varepsilon_{ij}^-}{\partial \varepsilon_{ij}} \tag{D.19}$$

From Eq. (2.59):

$$\frac{\partial \varepsilon_{ij}^-}{\partial \varepsilon_{ij}} = \frac{\partial \varepsilon_{ij}^+}{\partial \varepsilon_{ij}} = 1 \tag{D.20}$$

So, with definitions of Eq. (D.19) and Eq. (D.20), the derivatives of Eq. (D.18a)

becomes:

$$\frac{\partial \psi_0^+}{\partial \varepsilon_{kl}} = \lambda_0 R_n^+ \delta_{ij} \varepsilon_{ij} \delta_{kl} + 2\mu_0 P_{klmn}^+ \varepsilon_{mn} \tag{D.21a}$$

$$\frac{\partial \psi_0^-}{\partial \varepsilon_{kl}} = \lambda_0 R_n^- \delta_{ij} \varepsilon_{ij} \delta_{kl} + 2\mu_0 P_{klmn}^- \varepsilon_{mn} \tag{D.21b}$$

$$\frac{\partial \psi_0^+}{\partial \varepsilon_{kl} \partial \varepsilon_{mn}} = \lambda_0 R_n^+ \delta_{mn} \delta_{op} + 2\mu_0 P_{opmn}^+ \tag{D.21c}$$

$$\frac{\partial \psi_0^-}{\partial \varepsilon_{kl} \partial \varepsilon_{mn}} = \lambda_0 R_n^- \delta_{mn} \delta_{op} + 2\mu_0 P_{opmn}^- \tag{D.21d}$$

Now, in symbolic form, the constitutive and stress tensor can be written:

$$\underline{\sigma} = g(\phi) \left(\lambda_0 R_n^+ \mathrm{tr}(\underline{\varepsilon}) \underline{I} + 2\mu_0 \hat{\mathbf{P}}^+ : \underline{\varepsilon} \right) + \lambda_0 R_n^- \mathrm{tr}(\underline{\varepsilon}) \underline{I} + 2\mu_0 \hat{\mathbf{P}}^- : \underline{\varepsilon} \tag{D.22a}$$

$$\hat{\mathbf{C}} = g(\phi) \left(\lambda_0 R_n^+ \underline{I} \otimes \underline{I} + 2\mu_0 \hat{\mathbf{P}}^+ \right) + \lambda_0 R_n^- \underline{I} \otimes \underline{I} + 2\mu_0 \hat{\mathbf{P}}^- \tag{D.22b}$$

Appendix E

Strain energy density particularized for 2-D case

In this appendix is demonstrated the form of the strain energy density, particularized for a 2-D case, for the energy phase-field models presented in this work.

E.1 Eq. (2.64): Isotropic model

Is is already known that the strain energy density for a 2-D case, and the general stress tensor can be calculated by:

$$\psi_0 = \frac{1}{2}\sigma_{ij}\varepsilon_{ij} = \frac{1}{2}(\sigma_{11}\varepsilon_{11} + 2\sigma_{12}\varepsilon_{12} + \sigma_{22}\varepsilon_{22}) \tag{E.1a}$$

$$\sigma_{ij} = \lambda_0\delta_{ij}\mathrm{tr}(\varepsilon_{ij}) + 2\mu_0\varepsilon_{ij} \tag{E.1b}$$

Substituting Eq. (E.1b) in Eq. (E.1a) it gets:

$$\psi_0 = \frac{1}{2}\left[(\lambda_0\mathrm{tr}(\varepsilon_{ij}) + 2\mu_0\varepsilon_{11})\varepsilon_{11} + 2(2\mu_0\varepsilon_{12})\varepsilon_{12} + (\lambda_0\mathrm{tr}(\varepsilon_{ij}) + 2\mu_0\varepsilon_{22})\varepsilon_{22}\right] \tag{E.2}$$

Before some algebraic manipulations Eq. (E.2) becomes to Eq. (E.3), as it would wanted to be demonstrated:

$$\psi_0 = \frac{1}{2}\lambda_0\mathrm{tr}(\varepsilon_{ij})(\varepsilon_{11} + \varepsilon_{22}) + \mu(\varepsilon_{11}^2 + \varepsilon_{22}^2 + 2\varepsilon_{12}^2) \tag{E.3}$$

E.2 Eq. (2.65): Lancioni and Royer-Carfagni (2009)

To obtain the energy split made by Lancioni, for a 2-D case, this demonstration will start from Eq. (E.3) writing its second part in therms of volumetric and deviatoric tensor:

$$\psi_0 = \frac{1}{2}\lambda_0\mathrm{tr}(\varepsilon_{ij})(\varepsilon_{11} + \varepsilon_{22}) + \mu_0\left[(\varepsilon_{11}^D + \varepsilon_{11}^V)^2 + (\varepsilon_{22}^D + \varepsilon_{22}^V)^2 + 2(\varepsilon_{12}^D + \varepsilon_{12}^V)^2\right] \tag{E.4}$$

The therm in square brackets, before developed becomes:

$$[\cdots] = (\varepsilon_{11}^D)^2 + (\varepsilon_{22}^D)^2 + 2(\varepsilon_{12}^D)^2 + (\varepsilon_{11}^V)^2 + (\varepsilon_{22}^V)^2 + 2(\varepsilon_{12}^V)^2 + 2\varepsilon_{11}^D\varepsilon_{22}^V + 2\varepsilon_{22}^D\varepsilon_{22}^V + 4\varepsilon_{12}^D\varepsilon_{12}^V \quad \text{(E.5)}$$

Observe that, the first three therms of Eq. (E.5) correspond to the internal product of the active deviatoric strain tensor. In this way:

$$[\cdots] = \varepsilon_{ac_{ij}}^D\varepsilon_{ac_{ij}}^D + \frac{1}{9}(\mathrm{tr}(\varepsilon_{ij}))^2 + \frac{1}{9}(\mathrm{tr}(\varepsilon_{ij}))^2 + \frac{2}{3}\mathrm{tr}(\varepsilon_{ij})\varepsilon_{11}^D + \frac{2}{3}\mathrm{tr}(\varepsilon_{ij})\varepsilon_{22}^D \quad \text{(E.6)}$$

$$[\cdots] = \varepsilon_{ac_{ij}}^D\varepsilon_{ac_{ij}}^D + \frac{2}{9}(\mathrm{tr}(\varepsilon_{ij}))^2 + \frac{2}{3}\mathrm{tr}(\varepsilon_{ij})(\varepsilon_{11}^D + \varepsilon_{22}^D) \quad \text{(E.7)}$$

Rewriting the terms in parentheses in function of volumetric and total strains, becomes:

$$[\cdots] = \varepsilon_{ac_{ij}}^D\varepsilon_{ac_{ij}}^D + \frac{2}{9}(\mathrm{tr}(\varepsilon_{ij}))^2 + \frac{2}{3}\mathrm{tr}(\varepsilon_{ij})\left(\varepsilon_{11} - \frac{1}{3}\mathrm{tr}(\varepsilon_{ij}) + \varepsilon_{22} - \frac{1}{3}\mathrm{tr}(\varepsilon_{ij})\right) \quad \text{(E.8)}$$

$$[\cdots] = \varepsilon_{ac_{ij}}^D\varepsilon_{ac_{ij}}^D + \frac{2}{9}(\mathrm{tr}(\varepsilon_{ij}))^2 + \frac{2}{3}\mathrm{tr}(\varepsilon_{ij})(\varepsilon_{11} + \varepsilon_{22}) - \frac{4}{9}(\mathrm{tr}(\varepsilon_{ij}))^2 \quad \text{(E.9)}$$

$$[\cdots] = \varepsilon_{ac_{ij}}^D\varepsilon_{ac_{ij}}^D - \frac{2}{9}(\mathrm{tr}(\varepsilon_{ij}))^2 + \frac{2}{3}\mathrm{tr}(\varepsilon_{ij})(\varepsilon_{11} + \varepsilon_{22}) \quad \text{(E.10)}$$

Substituting Eq. (E.10) in Eq. (E.4), it arrives in Eq. (E.11):

$$\psi_0 = \left\{\mu_0\varepsilon_{ac_{ij}}^D\varepsilon_{ac_{ij}}^D\right\} + \left\{\frac{1}{2}\lambda_0\mathrm{tr}(\varepsilon_{ij})(\varepsilon_{11} + \varepsilon_{22}) + \mu_0\left(\frac{2}{3}\mathrm{tr}(\varepsilon_{ij})(\varepsilon_{11} + \varepsilon_{22}) - \frac{2}{9}(\mathrm{tr}(\varepsilon_{ij}))^2\right)\right\} \quad \text{(E.11)}$$

In symbolic form, it arrives at Eq. (2.65), as it would wanted to be demonstrated:

$$\psi_0 = \left\{\mu_0\underline{\varepsilon}_{ac}^D : \underline{\varepsilon}_{ac}^D\right\} + \left\{\frac{1}{2}\lambda_0\mathrm{tr}(\underline{\varepsilon})(\varepsilon_{11} + \varepsilon_{22}) + \mu_0\left(\frac{2}{3}\mathrm{tr}(\underline{\varepsilon})(\varepsilon_{11} + \varepsilon_{22}) - \frac{2}{9}(\mathrm{tr}(\underline{\varepsilon}))^2\right)\right\} \quad \text{(E.12)}$$

where the first therm in cases corresponds to ψ_0^+ and the second therm to ψ_0^-.

E.3 Eq. (2.66): Amor et al. (2009)

Observe that, the model proposed by Amor et al. (2009) is very similar to Lancioni and Royer-Carfagni (2009). The difference is that in Amor et al. (2009) the second therm in

cases of Eq. (E.13) is also considered as part as the active strain energy. In this way:

$$\psi_0 = \left\{\mu_0 \underline{\varepsilon}_{ac}^{D} : \underline{\varepsilon}_{ac}^{D} + R_n^{+}\left[\frac{1}{2}\lambda_0 \mathrm{tr}(\underline{\varepsilon})(\varepsilon_{11}+\varepsilon_{22}) + \mu_0\left(\frac{2}{3}\mathrm{tr}(\underline{\varepsilon})(\varepsilon_{11}+\varepsilon_{22}) - \frac{2}{9}(\mathrm{tr}(\underline{\varepsilon}))^2\right)\right]\right\} + \left\{R_n^{-}\left[\frac{1}{2}\lambda_0 \mathrm{tr}(\underline{\varepsilon}) + (\varepsilon_{11}+\varepsilon_{22}) + \mu_0\left(\frac{2}{3}\mathrm{tr}(\underline{\varepsilon})(\varepsilon_{11}+\varepsilon_{22}) - \frac{2}{9}(\mathrm{tr}(\underline{\varepsilon}))^2\right)\right]\right\} \tag{E.13}$$

where the first therm in cases corresponds to ψ_0^{+} and the second therm to ψ_0^{-}.

E.4 Eq. (2.67): Miehe et al. (2010b)

Comparing Eq. (2.54a) to Eq. (2.61a) it can be said that the strain energy density proposed by Miehe et al. (2010b) is very similar to isotropic constitutive model. Due that fact, in analogy to what was done in Appendix E.1 we can particularize Miehe et al. (2010b) strain energy density to 2-D case by:

$$\psi_0 = \left\{\frac{1}{2}\lambda_0 R_n^{+}\mathrm{tr}(\underline{\varepsilon})(\varepsilon_{11}+\varepsilon_{22}) + \mu_0 \underline{\varepsilon}_{ac}^{+} : \underline{\varepsilon}_{ac}^{+}\right\} + \left\{\frac{1}{2}\lambda_0 R_n^{-}\mathrm{tr}(\underline{\varepsilon})(\varepsilon_{11}+\varepsilon_{22}) + \mu_0 \underline{\varepsilon}_{ac}^{-} : \underline{\varepsilon}_{ac}^{-}\right\} \tag{E.14}$$

where the first therm in cases corresponds to ψ_0^{+}, the second therm to ψ_0^{-} and $\underline{\varepsilon}_{ac}^{+}$ and $\underline{\varepsilon}_{ac}^{-}$ corresponds to the active part of $\underline{\varepsilon}^{+}$ and $\underline{\varepsilon}^{-}$.

Appendix F

Demonstration of implementation equations

In this section will be demonstrated the necessary equation for implementation section.

F.1 Eq. (3.3): Dual internal variable operator in monolithic solver

The dual internal variables vector is calculated by deriving the internal energy functional with respect to the internal variables. In this way, for a plane case, the first three therms of this vector is the already known stress vector in Voigth notation.

Defining the internal energy functional by ψ^*, shown in Eq. (F.1a), the remaining therms is obtained by Eq. (F.1b) and Eq. (F.1c):

$$\psi^* = \psi + G_c\gamma \tag{F.1a}$$

$$\frac{\partial\psi^*}{\partial\phi} = \frac{\partial\psi}{\partial\phi} + \frac{\partial}{\partial\phi}\left(G_c\gamma\right) \tag{F.1b}$$

$$\frac{\partial\psi^*}{\partial\phi_{,i}} = \frac{\partial}{\partial\phi_{,i}}\left(G_c\gamma\right) \tag{F.1c}$$

By doing the chain rule in Eq. (F.1b) it becomes:

$$\frac{\partial\psi^*}{\partial\phi} = \frac{\partial\psi}{\partial g}\frac{\partial g}{\partial\phi} + \frac{G_c}{C_0}\frac{\partial}{\partial\phi}\left[\frac{\alpha(\phi)}{l_0} + l_0\phi_{,i}\phi_{,i}\right] = g'(\phi)\bar{Y} + \frac{G_c}{C_0 l_0}\alpha''(\phi) \tag{F.2}$$

And from Eq. (F.1c), it gets:

$$\frac{\partial\psi^*}{\partial\phi_{,i}} = \frac{G_c}{C_0 l_0}\frac{\partial}{\partial\phi_{,i}}\left[\phi_{,i}\phi_{,i}\right] = 2\frac{G_c}{C_0 l_0}\phi_{,i} \tag{F.3}$$

From all that discussed, the dual internal variables vector in given by Eq. (F.4), as it

would wanted to be demonstrated:

$$\bar{\sigma} = \left\{ \sigma_x \quad \sigma_y \quad \tau_{xy} \quad g'\bar{Y} + \frac{G_c}{C_0 l_0}\alpha' \quad 2\frac{G_c l_0}{C_0}\phi_{,x} \quad 2\frac{G_c l_0}{C_0}\phi_{,y} \right\}^T \tag{F.4}$$

F.2 Eq. (3.10): Constitutive tensor for plane stress in Voigt notation

In **plane stress**, $\sigma_{33} = 0$. From Generalized Hooke's law, it gets:

$$\sigma_{ij} = c_{ijkl}\varepsilon_{kl} \tag{F.5a}$$

$$\sigma_{33} = c_{3311}\varepsilon_{11} + c_{3322}\varepsilon_{22} + c_{3333}\varepsilon_{33} = 0 \tag{F.5b}$$

From Eq. (F.5b):

$$\varepsilon_{33} = -\frac{1}{c_{3333}}\left(c_{3311}\varepsilon_{11} + c_{3322}\varepsilon_{22}\right) \tag{F.6}$$

Substituting Eq. (F.6) in Eq. (F.5a) it can be obtained that:

$$\sigma_{11} = \left[c_{1111} - \frac{c_{1133}c_{3311}}{c_{3333}}\right]\varepsilon_{11} + \left[c_{1122} - \frac{c_{1133}c_{3322}}{c_{3333}}\right]\varepsilon_{22} \tag{F.7a}$$

$$\sigma_{22} = \left[c_{2211} - \frac{c_{2233}c_{3311}}{c_{3333}}\right]\varepsilon_{11} + \left[c_{2222} - \frac{c_{2233}c_{3322}}{c_{3333}}\right]\varepsilon_{22} \tag{F.7b}$$

$$\sigma_{12} = \frac{1}{2}(c_{1212} + c_{1221})\gamma_{12} \tag{F.7c}$$

As it would wanted to be demonstrated, using Eq. (F.7) the constitutive matrix can be written as:

$$[\mathbf{C}]^u_{\text{stg}} = \begin{bmatrix} \left(c_{1111} - \frac{c_{1133}c_{3311}}{c_{3333}}\right) & \left(c_{1122} - \frac{c_{1133}c_{3322}}{c_{3333}}\right) & 0 \\ \left(c_{2211} - \frac{c_{2233}c_{3311}}{c_{3333}}\right) & \left(c_{2222} - \frac{c_{2233}c_{3322}}{c_{3333}}\right) & 0 \\ 0 & 0 & \frac{1}{2}(c_{1212} + c_{1221}) \end{bmatrix} \tag{F.8}$$